Defect engineering of UiO-66 metal-organic framework (MOF) for improved hydrogen storage applications

By

MPHO LEDWABA

Submitted in partial fulfilment of the requirements for the degree of

Doctor of Philosophy

in the Department of Chemistry and Polymer Science

FACULTY OF SCIENCE

STELLENBOSCH UNIVERSITY

Supervisor: Prof. Leonard Barbour

Co-Supervisor: Prof. Jianwei Ren

March 2021

DECLARATION BY CANDIDATE

I hereby declare that the work found in this dissertation submitted for a degree at Stellenbosch University is solely my own original work and has not previously been submitted to any other higher education institution. I further confirm that all sources referenced or quoted herein are confirmed and acknowledged by virtue of a list of references.

March 2021

DEDICATION

"The mind of the prudent acquires knowledge"

"The ear of the wise seeks knowledge"

"It is not good for a person to be without knowledge"

"Listen to counsel, receive instruction and accept correction that you may be wise in the time to come."

"Train up a child in the way she should go, teaching her to seek Gods wisdom and will for his abilities and talents."

These are a few of many teachings from the book of Proverbs

I dedicate this research to my mother, **Priscilla Ledwaba** who firmly instilled these teachings in my life, encouraging me to pursue what my heart desires regardless of the circumstances that seemed like a barrier. In her financial struggles, she ensured that I achieved my goals and pushed me forward to where I am today. I write this with tears of joy in my eyes, grateful that you are alive to see the product of your strength.

ACKNOWLEDGEMENTS

I would like to first and foremost give thanks my heavenly Father, the Sovereign Master and Creator of all things. It has not been by power or wisdom but only by Your Spirit and Grace that I arrived at the finish line. You have carried me through the ups and downs (and yes there were plenty of downs) and when I wanted to give up, You lifted me up encouraged me with your unfailing word and gave me new strength.

Your word in Psalms says "weeping may last for a night, but JOY comes in the morning"

Oh LORD my GOD I give Glory to YOU forever!!!

This would not have been possible without the assistance of my supervisors Profs Len Barbour and Jianwei Ren. Thank you for transferring knowledge, for the guidance and for pushing me to achieve my goals. According to the Oxford Dictionary a supervisor is someone who directs and oversees the work of another, and I can say that you have fulfilled that duty exceptionally. The advice you gave me showed that not only were you doing what you had to, but you wanted to better me as a person and a researcher not only for this project but also for the future. I am truly grateful.

I acknowledge the Hydrogen South Africa (HySA) team for being such a great support structure. Thank you for every contribution you have made towards my work. Dr Musyoka, I thank you for all your assistance. You are the backbone of this work. Your endless supply of advice and guidance didn't go unnoticed. Dr H and Dr North, thank you for all the technical work you did backstage. Thank you for the regular check-up; I appreciate each of you.

I thank my husband, Kgositsile Mogaswane, for always being there for me. The late nights at work, listening to my complaints when things were not working in the lab, I would have broken down if you were not by my side. Thank you for being my pillar of strength.

Additionally, I would like to acknowledge CSIR for hosting me and financing my studies under a Doctoral Studentship. Through this studentship, you provided the training and facilities needed for me to realise completion of this research. I would also like to thank Stellenbosch University for all the support especially Dr Marike Du Plessis for all the administrative sopport as well as the National Research Foundation (NRF) for the financial support..

Finally, I would like to extend sincere gratitude to my fellow EC colleagues/friends for their assistance and for creating a friendly research environment.

ABSTRACT

Metal–organic frameworks (MOFs) as a relatively new class of porous crystalline materials have attracted much interest in many applications due to their high porosity, diverse structures, and controllable chemical structures. However, the specific geometrical morphologies, limited functions and unsatisfactory performances of pure MOFs hinder their further applications. Several modifying strategies for engineering MOF crystals have been developed based on their desired features and applications. In nature there are no "ideal crystals" with an infinite periodic repetition or ordering of the same groups of atoms in space. The structure of "real crystals" often deviates from the ideal arrangement and includes a significant density of structural irregularities or deficiencies. Crystal irregularities may arise from compositional inhomogeneities, and this term is often used interchangeably. By using defective technology strategies during their synthesis, crystal imperfections may be introduced into the MOF framework, thereby enhancing their performance in the envisioned applications. Defect engineering is one of the most effective approaches that one can use to change their physical and chemical features such as thermal stability, textural properties, mechanical properties and gas adsorption abilities. In order to achieve the desired changes, it is essential to control the defects, otherwise these defects may have an adverse effect on the MOFs. Therefore, it is vitally important to apply synthetic control over defects; the exact nature and concentration of the defects may be controlled by modifying the synthetic conditions and post-synthetic modifications. Structurally characterising inherent or engineered defects is very challenging and this challenge has not been addressed substantially.

This thesis explores the experimental creation of structural defects via post-synthetic modification, the role of structural defects and their relationship to gas adsorption, with

emphasis on hydrogen adsorption. Through a combination of techniques, including powder X-ray diffraction (PXRD), thermogravimetric analysis (TGA), acid-base titration and Brunauer–Emmett–Teller (BET) surface area and pore size measurements, missing linkers and missing cluster defects have been identified and analysed. In Chapter 4, we seek to understand the relationship between some of the major synthetic parameters and the physicochemical characteristics of UiO-66 (Universitetet i Oslo) MOF and discover a "non-defective" sampling technique for this material. The technique produces non-defective UiO-66 MOFs at a specific temperature (493 K), with the linker ratio being greater than that of the salt previously reported by Shearer et al. As described in Chapter 5, by varying the concentrations of modulator and the linker, we demonstrate that the linker vacancies can be systematically tuned, leading to significantly increased surface areas. The defects are caused by partial terephthalic acid replacement with smaller formate groups from the formic acid modulator. The BET surface areas of the obtained samples range from 1200 to 1600 $m^2.g^{-1}$, and the best sample has a surface area that is about 30% higher than the theoretical value of the surface area of defect-free UiO-66. Additionally, linker vacancies are proven to have profound effects on the gas adsorption behaviour of UiO-66 by improving the hydrogen uptake from 1.51 wt. % to 2.0 wt. % at 77 K and 1 bar. Chapters 5 and 6 include detailed studies of two conventional methods for generating defects (i.e., de novo defect technology and post-synthetic modification (PSM)) discussed in each chapter respectively. Still in chapter 5, experimental investigations are discussed that show the impact of modulator and linker concentration on H_2 adsorption and thermal stability. Chapter 6 provides insight into the impact on thermal stability and adsorption properties brought about by the post-synthetic modification methods. The resultant materials typically have high surface areas, large pore volumes and structures with hierarchical pores, which makes them more practical for hydrogen storage applications.

OPSOMMING

Metaal–organiese raamwerke (MOFs) as ′n relatief nuwe klas van poreuse, kristallyne materiale lok baie belangstelling in vele toepassings as gevolg van hul hoë poreusheid, diverse strukture en beheerbare chemiese strukture. Die spesifieke geometriese morfologie, beperkte funksies en onbevredigende werkverrigting van suiwer MOFs beperk egter hul verdere toepassing. Heelwat modifiseringstrategieë vir die ontwerp van MOF kristalle, gebaseer op hul gewensde eienskappe, is reeds ontwikkel. In die natuur is daar nie "ideale kristalle" met ′n oneindige, periodiese herhaling of gespasieerde orde van dieselfde groepe atome nie. Die struktuur van "regte kristalle" wyk dikwels af van die ideale rangskikking en sluit ′n aansienlike digtheid van strukturele onreëlmatigheid of gebreke in. Kristalonreëlmatighede kan voorkom wanneer die samestelling nie homogeen is nie en hierdie terme word dikwels afwisselend gebruik. Deur gebruik te maak van defek-tegnologie strategieë gedurende sintese, kan kristalonvolmaaktheid in die MOF raamwerk ingebou word en so hul werkverrigting in die beoogde toepassings versterk. Defek-konstruksie is een van die mees effektiewe benaderings wat gebruik kan word om die fisiese en chemiese eienskappe, soos byvoorbeeld termiese stabiliteit, teksturele eienskappe, meganiese eienskappe en gassorpsievermoë, van MOFs te verander. Om die verlangde veranderinge te bereik, is dit noodsaaklik om die defekte te beheer, anders kan die defekte ′n ongunstige effek op die MOF hê. Daarom is dit uiters belangrik om beheer oor defekte tydens sintese toe te pas; die presiese aard en konsentrasie van defekte kan beheer word deur die toestande tydens sintese te wysig, asook deur na-sintetiese modifikasie. Om inherente-, of ingeboude defekte struktureel te karakteriseer, is uitdagend en hierdie uitdaging is nog nie aansienlik aangespreek nie.

Hierdie tesis ondersoek die eksperimentele inbou van strukturele defekte deur middel van de-novo en na-sintetiese modifikasie. Hierin ondersoek ons ook die rol van strukturele defekte en hoe hul verband hou met gasadsorpsie, met ′n klem op waterstof adsorpsie. Deur gebruik te maak van ′n kombinasie van tegnieke, insluitend poeier X-straaldiffraksie (PXRD), termogravimetriese analise (TGA), suur-basis titrasie, Brunauer–Emmett–Teller (BET) oppervlak-area en meting van porie-grootte, kon vermiste skakels en bondeldefekte geïdentifiseer en geanaliseer word. In Hoofstuk 4 poog ons om die verhouding tussen sommige van die hoof sintetiese parameters en die fisikochemiese eienskappe van UiO-66

(Universitetet i Oslo) MOF te verstaan en ontdek ′n "nie-defektiewe" monsternemingstegniek vir hierdie materiaal. Hierdie tegniek produseer nie-defektiewe UiO-66 MOFs by ′n spesifieke temperatuur (493 K), met ‘n skakelverhouding groter as dié van die sout wat voorheen deur Shearer et al. gerapporteer is. Soos beskryf in Hoofstuk 5, deur die konsentrasies van die modulator en die skakel te varieer, demonstreer ons dat die skakelgapings sistematies gestel kan word, wat lei tot ′n merkwaardige toename in oppervlak-areas. Die defekte word veroorsaak deur die gedeeltelike vervanging van tereftaalsuur met kleiner formaatgroepe, afkomstig van die formaatsuur modulator. Die BET oppervlak-areas van die monsters wat verkry is, strek van 1200 to 1600 $m^2.g^{-1}$ en die beste monster het ′n oppervlak-area ongeveer 30% hoër as die teoretiese waarde vir die oppervlak-area van defek-vrye UiO-66. Verder is dit bewys dat skakelgapings groot effekte het op die gasadsorpsie gedrag van UiO-66 deur die waterstofopname van 1.51 wt. % tot 2.0 wt. % by 77 K en 1 bar te verbeter. Hoofstukke 5 en 6 sluit noukeurige studies in van twee konvensionele metodes om defekte te genereer (naamlik de novo defek-tegnologie en na-sintetiese modifikasie (PSM)) soos bespreek in elke hoofstuk afsonderlik. Steeds in Hoofstuk 5, word eksperimentele ondersoeke bespreek, wat die impak van modulator en skakel konsentrasie op H_2-adsorpsie en termiese stabiliteit wys. Hoofstuk 6 verskaf insig ten opsigte van die inwerking op termiese stabiliteit en adsorpsie eienskappe teweeggebring deur die na-sintetiese modifikasie metodes. Die gevolglike materiale het tipies hoë oppervlak-areas, groot porievolumes en strukture met hiërargiese porieë, wat dit meer prakties maak vir waterstof-storingstoepassings.

TABLE OF CONTENTS

LIST OF FIGURES

LIST OF TABLES

ABBREVIATIONS

1/2/3D	One/ two/ three dimensional
AA	Acetic acid
AFM	Atomic force microscopy
ATR	Attenuated total reflection
BDC	Benzene-1,4-dicarboxylic acid (terephthalic acid)
BET	Brunauer-Emmett-Teller
Bp	Boiling point
BTC	Benzenetricarboxylic acid
BTUs	British Thermal Units
CFM	Confocal fluorescence microscopy
$CHCl_3$	Chloroform
CNCs	Coordination network compounds
DFA	Difluoroacetic acid
DMF	N,N'-dimethyl formamide
DOE	Department of Energy
DRIFTS	Diffuse reflectance infrared Fourier transform spectroscopy
DSC	Differential scanning calorimetry
E_a	Activation energy
EDS	Energy-dispersive X-ray spectroscopy
ESI-MS	Electrospray ionisation mass spectrometry
fcc	Face centered cubic
FTS	Form-Tech Scientific
H_2BDC	Terephthalic acid
HCOOH	Formic acid
HD	High definition
H-K	Horvath-Kawazoe
HRNPD	High-resolution neutron powder diffraction
FA	Formic acid
FTIR	Fourier transform Infra-red
HCl	Hydrochloric acid
HKUST	Hong Kong University of Science and Technology
IRMOF	Isoreticular metal-organic framework

LEDs	Light emitting diodes
LNCS	Liquid Nitrogen Cooling System
mCUS	Coordinatively unsaturated metal sites
MIL	Matérial Institut Lavoisier
MM-MOFs	Mixed metal- metal organic frameworks
MOFs	Metal-organic frameworks
NMR	Nuclear magnetic resonance
NTP	Normal temperature and pressure
OH	Hydroxyl
PBU	Paddlewheeled building unit
PCPs	Porous coordination polymers
PSD	Pore size distribution
PSE/M	Post synthetic Exchange/Modification
Psi	Parts per square inch
PXRD	Powder X-ray diffraction
RPM	Rates per minute
SAM	Self-assembled membrane
SEM	**S**canning electron microscope
SBB	Super building block
SBET	Brunauer-Emmett-Teller surface area
SBU	Secondary building unit
SCXRD	Single crystal X-ray diffraction
SSA	Specific surface area
STP	Standard temperature and pressure
SURMOF	**S**urface-anchored metal organic frameworks
TEM	Transmission electron microscopy
TFA	Triflouroacetate
TGA	Thermogravimetric analysis
UHM	University of Hamburg Materials
UiO	Universiteteit i Oslo
UV	Ultra-violet
Vpore	Pore volume
ZIF	Zeolitic imidazolate framework
ZJU	Zhejiang University

PUBLICATIONS

Jianwei Ren., **Mpho Ledwaba**, Nicholas Musyoka, Henrietta Langmi, Mkhulu Mathe, S Liao and W Pang,. Structural defects in metal–organic frameworks (MOFs): Formation, detection and control towards practices of interests. *Coord. Chem. Rev*. **2017**, *349*, pp.169-197. *(Published)*

Mpho Ledwaba, Jianwei Ren, Nicholas M. Musyoka, Mkhulu Mathe. Equilibrium and Kinetics for Hydrogen Adsorption in UiO-66 MOFs. *(In progress)*

SYMPOSIUMS/CONFERENCE PRESENTATIONS

Mpho V. Ledwaba, Jianwei Ren. Generation of defective UiO-66 Metal Organic Frameworks (MOFs) for hydrogen storage, 1st Africa Energy Materials conference, 28 - 31 March 2017, Council for Scientific and Industrial Research, Pretoria, South Africa. *(Oral presentation)*

Mpho V. Ledwaba, Jianwei Ren, Nicholas M. Musyoka, Henrietta W. Langmi, Mkhulu Mathe. Post-synthetic modification in the formation and control of structural defects in UiO-66 metal-organic frameworks, 30th IPHE Steering committee, 04-07 December 2018, University of Pretoria (UP), Pretoria, South Africa. *(Poster presentation)*

Mpho V. Ledwaba, Jianwei Ren, Nicholas Musyoka, Henrietta Langmi. Post-synthetic modification in the formation and control of structural defects in UiO-66 metal-organic frameworks, 43rd National Convention of the South African Chemical Institute, 02- 07 December 2018, Council for Scientific and Industrial Research International Convention Centre, Pretoria, South Africa.

CHAPTER 1: INTRODUCTION

1.1 Background

Energy in the world today is becoming a major concern because a secure and sustainable energy supply is necessary for society to thrive [1]. There is an increasing demand to meet global energy standards, which effectively defines the livelihood of the population. Energy is used to produce the power needed in our homes, factories, schools and enterprises for everyday living and functioning. It energises, just to mention a few, our computers, lamps, fridges, lavators and climatiseurs. In addition, the amount of energy required in the industrial sector continues to grow. This energy is mainly generated by the combustion of fossil fuel stocks and large amounts of contaminating gas (CO_2, NO_X etc.) are discharged into the atmosphere [2, 3]. These gases, particularly CO_2, contribute significantly and adversely to global warming, including an increase in average global temperatures, an increase in sea levels, floods and deforestation. The impact on governments, policymakers and environmentalists of global warming has become a matter of great concern. Of late, numerous studies that have been commissioned have focused on developing environmentally friendly, sustainable and affordable carbon-free energy sources in order to minimise pollutant gas emissions into the atmosphere as a consequence of the high usage of energy globally [4].

There are two categories of energy available in the world today: renewable and non- renewable energy. The former is replenished by natural resources. Non-renewable energy is not replenished or only slowly replenished. The renewable energy structures available vary from solar, wind power systems, geothermal and so forth. Renewable systems offer economic and environmental advantages for various applications in comparison to non-renewable systems. The secondary energy sources, including electricity and hydrogen, can be generated from renewable as well as non-renewable energy. The primary sources of energy currently are non-

renewable, including fossil fuels, that is, oil, coal and gas [3]. The negative environmental impact of fossil fuels is increasing and their cost (electricity) is rising. Renewable energy resources are slowly becoming an important alternative to fossil fuel. The quality, nature modularity, low operating costs, mobility and adaptable nature of renewable energy technologies, make it a viable substitute for fossil fuels. Many consider these sources of energy as directly replacing existing technologies for fossil fuels, which lowers the cost compared to conventional fossil-fuel technologies [1]. This reduces the pressure on national grids and ensures that people in remote areas also have access to energy. Furthermore, it contributes to a reduction in the amount of fossil fuel released to the atmosphere. The global energy consumption forecast is estimated at approximately 700 quadrillion British thermal units (BTUs) by 2030 [5]. That number is twice as much power as the current usage. The predominant energy sources will continue to be fossil fuels, accounting for over 90% of the expected demand growth [5]. The supply and demand challenges are more than threats to global warming, but environmental concerns are growing on a regular basis, such as ozone depletion, contamination, deforestation, and radioactive releases [1]. If the planet is to reach a stable energy future, these environmental issues must be resolved rapidly. The goal today is to pursue sustainability by using energy sources which have little or no adverse environmental impact [6, 7]. Such sources of energy (solar, wind, etc.) are easily replenished once used when contrasted to the limited fossil fuels (oil, coal and natural gas). Hydrogen is typically a safe and sustainable fuel source and a secure source of energy [8, 9]. This type of fuel can be produced from various sources, which include most fossil and renewable fuels (natural gases and carbon gasification). Figure 1.1 shows that hydrogen is produced from diverse resources and emissions are generally limited to heat and water, as compared to gasoline which has carbon emissions.

Hydrogen is thus an essential energy source solution for long-term energy sustainability.

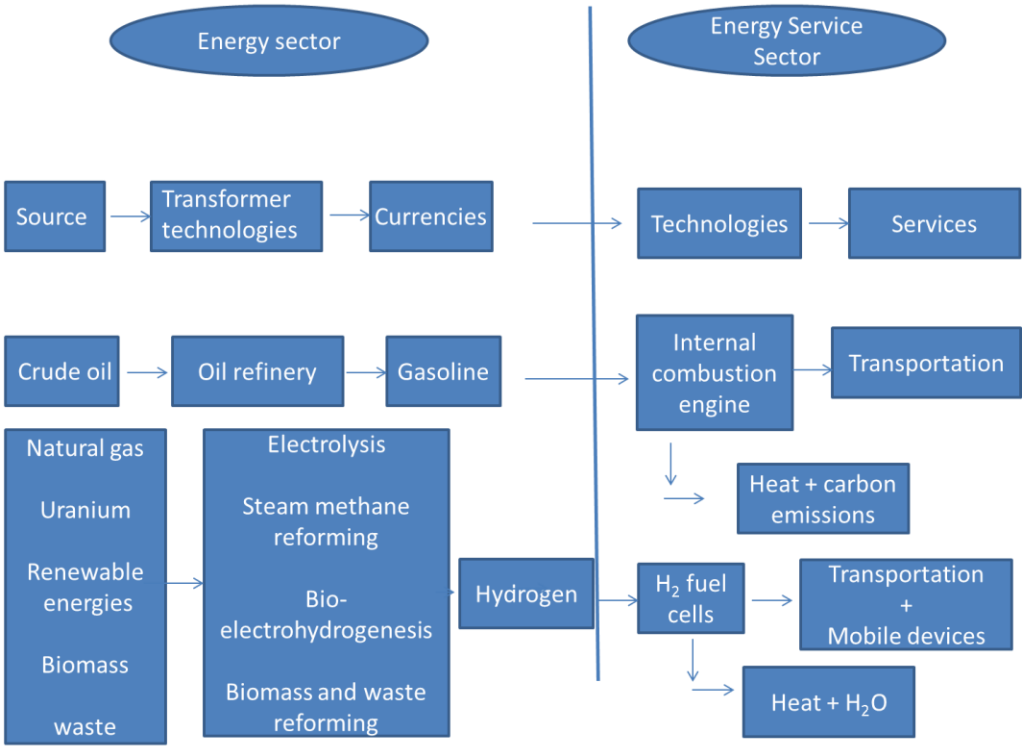

Figure 1.1 An evaluation of hydrogen and petrol in the energy supply chain currency [10]

Due to some unique desirable properties, hydrogen has been regarded as a potential fuel source for a long time in motor applications [11]. These properties include their oxygen combustion, which only generates water as waste, although it can produce certain oxides of nitrogen when combusted in air. A comparison of hydrogen with combustion features of other fuels is presented in Table 1.1, which displays the combustion characteristics of hydrogen, methane and gasoline. The importance for sustainable development and resolution of global environmental problems of hydrogen energy has been shown by recent studies [12-14]. The transition to the hydrogen economy, where hydrogen is the principal power supplier, and electricity is the principal non-chemical form of energy, is progressively increasing and interest has been growing rapidly in this field. However, direct hydrogen to electricity generation requires energy expertise such as fuel cell technologies. The fuel cell is a thermodynamic

system that provides energy through an electrochemical reaction, directly converting the chemical energy into electrical energy [15].

Table 1.1. Combustion characteristics of hydrogen compared to other fuels [4]

Property	**Hydrogen**	**Methane**	**Gasoline**
Flammability limits (% by volume)	4-75	5.3-15.0	1.2-6.0
Minimum ignition energy (mJ)	0.02	0.28	0.25
Laminar flame speed at NTP ($m.s^{-1}$)	1.9	0.38	0.37-0.43
Adiabatic temperature (K)	2318	2190	~2470
Auto-ignition temperature (K)	858	813	~500-750
Quenching gap at NTP (mm)	0.64	2.03	~2.0

The demand for highly efficient power generation devices has driven recent advances in fuel cells. Current investments in fuel cell technologies are primarily directed towards increasing their efficiency and/or utilising hydrogen as an auxiliary fuel by the automotive industry. Applications in energy and electronics industries also offer opportunities. The foremost motive for fuel cells usage in energy production is the necessity to decrease pollution, to increase power supply, to diversify energy supplies and to decrease external reliance on energy. In remote settings such as in satellites, remote weather stations, large forests, agricultural areas, and some military applications, fuel cells are very useful as power sources [16].

1.2 **Problem statement**

Hydrogen can potentially be utilised in various sectors, including industrial processes and transport, as a carbon-free energy carrier. It is currently being implemented in powering a growing fleet based on fuel cell technologies, including trains in Germany buses in South Korea, cars in California and forklifts all over the world. Such vehicles, which use fuel cells are needed to keep the hydrogen economy growing and for evolving various industries.

Hydrogen has a very low volumetric energy density under atmospheric conditions relative to gasoline and other automotive fuels. It must be accommodated in a vehicle either as a super-cooled liquid or as a heavily concentrated gas, both methods requiring additional energy. Compressed hydrogen in hydrogen tanks at 350 bar (5,000 psi) and 700 bar (10,000 psi) is used for hydrogen tank systems in automobiles. Although this technology has made it possible to commercialise hydrogen vehicles, it does not achieve the challenging U.S. DOE density targets. The discovery of hydrogen storage materials capable of meeting all DOE goals is an important stepping-stone towards a sustainable hydrogen economy. Theoretically, porous materials can store more hydrogen than high pressure fuel tanks. But, owing to the weak interaction of hydrogen gas with the pore walls, much of the storage space is unused and remains void. Such materials work best at cryogenic temperatures that are too low for practical use. In order to increase the amount of hydrogen contained in the materials, it is suggested that hydrogen-"grabbing" elements such as boron or nitrogen be added to the carbon connectors that form the pore walls or introducing and controlling defects.

1.3 **Significance**

Metal-based materials such as MOFs have generated much interest as porous gas storage materials for several new applications such as catalysis, thermal energy storage, chemical sensors, pharmaceutical delivery and equipment related to electronics. The characteristics of

MOFs must be strategically adjusted and manipulated to achieve optimised performance for these planned applications. Since the MOF research community first recognised defects in the structures of MOFs, the deliberate inclusion of defects has been proposed to change their properties.

Substantially large pores within a MOF hamper its ability to store hydrogen, since the potential surface of the pores will not attract H_2 molecules that are close to the centres of the pores. These low-density framework solids are usually only able to take up low volumetric H_2. It is widely accepted that a large total of micropore volume consisting of small pores is better suited for effective storage of hydrogen [17]. For this reason, framework interpenetration for tuning of pores and structures has been developed for optimal hydrogen uptake and retention at low pressure [18-19]. Bai et al. [20-22] and Feng et al. [23] likewise illustrated that micro- and mesopore co-existence in MOFs induced a higher H_2 heat of adsorption for the intense physisorption from inter-crystalline mesopores [24-26] .

Heterogeneity, structural defects and disorders to varying degrees are key characteristics of solid-state materials and can significantly impact their physical and chemical characteristics. In certain instances, perfect crystals are desirable; but defects are not intrinsically detrimental to their application [27]. Structural defects are being introduced into MOFs to allow the diffusion of hydrogen, but these defects should be adequately tuned for hydrogen storage [28]. Different methods to detect structural defects in UiO-66 have already been introduced. Even though structural defects will promote the storage of hydrogen in MOF structures, they should be tuned for hydrogen adsorption at the optimum level. The 12-connected framework structure of UiO-66 has been shown to include missing linker deficiencies. However, the hydrogen adsorption behaviour has deviated from the anticipated results in the case of defect-free crystals [29-30]. The existence of structural defects in UiO-66 also explains why the experimental BET surface areas are greater than those calculated, which in turn results in greater adsorption of

hydrogen. In this work defects in UiO-66 have been studied and their effect on hydrogen storage compared to defect-free UiO-66 MOF material, which have already been well documented.

1.4 Purpose of study

Generally, the term 'defects' implies a certain disappointment, but scientists take a different view. They noticed that defects can be put to good use in the field of nanoporous materials if one can monitor and control them. The purpose of this study is to investigate modification of the properties of metal-organic frameworks (MOFs), specifically UiO-66 MOF, by tuning the structural defects to enhance hydrogen storage capacities. UiO-66 MOFs containing zirconium are unique because they can tolerate the loss of approximately 4-5 linkers without collapsing, i.e. maintaining their structure. Such defects offer an enticing opportunity to manipulate the properties of the material. Our area of research focuses on making hydrogen storage safe and affordable, which can be realised through a thorough understanding of fundamentals and principles towards the advancement of applied research. This is essentially the course that this study takes. The study demonstrates the concept and the results also form the basis for future work.

1.5 Aims of the project

Generation of structural defects in UiO-66 MOFs to facilitate hydrogen spill-over and to systematically evaluate the performance of the defective MOFs for hydrogen storage.

1.6 Objectives of the project are to:

- synthesise defect-free MOF crystals;
- generate structural defects in MOF structures;
- characterise the defective MOF structures;

- evaluate the hydrogen storage performance.

1.7 **Thesis outline**

Chapter 2 provides a theoretical basis for the study, including an overview of previous work on defects in MOFs and other related topics. Chapter 2 aims to provide foundational knowledge on the topic, identify gaps in research and conflicts in previous studies, and to address open questions from other research. Chapter 3 of this thesis includes a detailed description of all techniques used in the course of this work. Chapter 4 describes an in-depth study of the pristine (non-defective) UiO-66 MOF, showing that no/insignificant defects are detected in the material. The material was analysed for (BET) surface area and H_2 uptake and tested for thermal stability, crystallinity and pore size distribution with the aim of elucidating the nature of the framework for further reference in the following sections. Chapter 5 describes defect engineering of the UiO-66 MOF using a de-novo approach. Two different methodologies were studied, namely modulation and variation of linker concentration. Use of a modulator in the synthesis of UiO-66 MOF led us to hypothesise that an increase in the concentration of the modulator increases the defect concentration. It was assumed that the modulator improves the crystallinity of the materials, but this was not observed as the modulator plays the part of the linker in the framework, triggering deterioration in the expected octahedral shape of the UiO-66 MOF. As expected, however, we identified an increase in the surface area and hydrogen uptake, although not for all the concentrations of modulator used. Still focusing on the same MOF material, Chapter 6 describes post-synthetic modification of the as-synthesised pristine UiO-66 MOF that was previously synthesised and described in Chapter 4. Two types of post-synthetic modification methods were explored, namely acid /base treatment and mechanical exposure. Both methods have been documented to influence defective structures without any

spontaneous structural or phase changes. However, both approaches jeopardize the stability and crystallinity of the material. Gas sorption studies have been conducted to determine whether the defects influence the efficiency of the adsorption of hydrogen. Different techniques such as powder X-ray diffraction (PXRD), thermogravimetric analysis (TGA), differential scanning calorimetry (DSC), gas sorption, etc. were used extensively to research the systems and materials described in this thesis.

1.8 References

1. Asif, M. and Muneer, T., Energy supply, its demand and security issues for developed and emerging economies. *Renew. Sust. Energ. Rev.*, **2007**, *11*(7), 1388-1413.
2. Panwar, N.L., Kaushik, S.C. and Kothari, S., Role of renewable energy sources in environmental protection: A review. *Renew. Sust. Energ. Rev.*, **2011**, *15*(3), 1513-1524.
3. Demirbaş, A., Biomass resource facilities and biomass conversion processing for fuels and chemicals. *Energy Convers. Manage.*, **2001**, *42*(11), 1357-1378.
4. Karim, G.A., Hydrogen as a spark ignition engine fuel. *Int. J. Hydrogen Energy*, **2003**, *28*(5), 569-577.
5. Salvi, B.L. and Subramanian, K.A., Sustainable development of road transportation sector using hydrogen energy system. *Renew. Sust. Energ. Rev.*, **2015**, *51*, 1132-1155.
6. Conti, J.J., Holtberg, P.D., Beamon, J.A., Schaal, A.M., Ayoub, J.C. and Turnure, J.T., Annual energy outlook. *US Energy Information Administration*, **2014**, 2.
7. Hart, S.L., Beyond greening: strategies for a sustainable world. *Harvard Business Rev.*, **1997**, *75*(1), 66-77.
8. Omer, A.M., Energy, environment and sustainable development. *Renew. Sust. Energ. Rev.*, **2008**, *12*(9), 2265-2300.
9. Edwards, P.P., Kuznetsov, V.L., David, W.I. and Brandon, N.P., Hydrogen and fuel cells: towards a sustainable energy future. *Energy Policy*, **2008**, *36*(12), 4356-4362.
10. Obayopo, S.O., *Performance enhancement in proton exchange membrane cell-numerical modelling and optimisation* (Doctoral dissertation, University of Pretoria). **2013**
11. Sherif, S.A., Barbir, F. and Veziroglu, T.N., Wind energy and the hydrogen economy—review of the technology. *Sol. Energy*, **2005**, *78*(5), 647-660.
12. Dincer, I. and Acar, C., A review on clean energy solutions for better sustainability. *Int. J. Energy Res.*, **2015**, *39*(5), 585-606.

13. Omer, A.M., Energy, environment and sustainable development. *Renew. Sust. Energ. Rev.*, **2008**, *12*(9), 2265-2300.
14. Chu, S. and Majumdar, A., Opportunities and challenges for a sustainable energy future. *Nature*, **2012**,*488*(7411), 294.
15. Kirubakaran, A., Jain, S. and Nema, R.K., A review on fuel cell technologies and power electronic interface. *Renew. Sust. Energ. Rev.*, **2009**, *13*(9), 2430-2440.
16. De Paepe, M., D'Herdt, P. and Mertens, D., Micro-CHP systems for residential applications. *Energy Convers. Manage.*, **2006**, *47*(18-19), 3435-3446.
17. Rowsell, J.L. and Yaghi, O.M., Strategies for hydrogen storage in metal–organic frameworks. *Angew. Chem., Int. Ed.*, **2005**, *44*(30), 4670-4679.
18. Küsgens, P., Zgaverdea, A., Fritz, H.G., Siegle, S. and Kaskel, S., Metal-Organic Frameworks in Monolithic Structures. *J. Am. Ceram. Soc.*, **2010**, *93*(9), 2476-2479.
19. Belof, J.L., Stern, A.C., Eddaoudi, M. and Space, B., On the mechanism of hydrogen storage in a metal− organic framework material. *J. Am. Chem. Soc.*, **2007**, *129*(49), 15202-15210.
20. Xin, Z., Bai, J., Pan, Y. and Zaworotko, M.J., Synthesis and Enhanced H_2 Adsorption Properties of a Mesoporous Nanocrystal of MOF-5: Controlling Nano-/Mesostructures of MOFs To Improve Their H_2 Heat of Adsorption. *Chem. Eur. J.*, **2010**, *16*(44), 13049-13052.
21. Xin, Z., Bai, J., Shen, Y. and Pan, Y., Hierarchically micro-and mesoporous coordination polymer nanostructures with high adsorption performance. *Cryst. Growth Des.*, **2010**, *10*(6), 2451-2454.
22. Du, H., Bai, J., Zuo, C., Xin, Z. and Hu, J., A hierarchical supra-nanostructure of HKUST-1 featuring enhanced H_2 adsorption enthalpy and higher mesoporosity. *CrystEngComm*, **2011**, *13*(10), 3314-3316.

23. Feng, Y., Jiang, H., Chen, M. and Wang, Y. Construction of an interpenetrated MOF-5 with high mesoporosity for hydrogen storage at low pressure. *Powder Technol.* **2013**, *249*, 38-42.

24. Belof, J.L., Stern, A.C., Eddaoudi, M. and Space, B., On the mechanism of hydrogen storage in a metal− organic framework material. *J. Am. Chem. Soc.* **2007**, *129*(49), 15202-15210.

25. Xin, Z., Bai, J., Pan, Y. and Zaworotko, M.J., Synthesis and Enhanced H_2 Adsorption Properties of a Mesoporous Nanocrystal of MOF-5: Controlling Nano-/Mesostructures of MOFs To Improve Their H_2 Heat of Adsorption. *Chem. Eur. J.* **2010**, *16*(44), 13049-13052.

26. Xin, Z., Bai, J., Shen, Y. and Pan, Y., Hierarchically micro-and mesoporous coordination polymer nanostructures with high adsorption performance. *Cryst. Growth Des.* **2010**, *10*(6), 2451-2454.

27. Capper, P., *Bulk Cryst. Growth Electron., Opt. Optoelectron. Mater*. Ed., John Wiley & Sons. 2005, Vol. 14

28. Ren, J., Langmi, H.W., Musyoka, N.M., Mathe, M., Kang, X. and Liao, S., Tuning defects to facilitate hydrogen storage in core-shell MIL-101 (Cr) @ UiO-66 (Zr) nanocrystals. *Mater. Today: Proc.* **2015**, *2*(7), 3964-3972.

29. Du, H., Bai, J., Zuo, C., Xin, Z. and Hu, J., A hierarchical supra-nanostructure of HKUST-1 featuring enhanced H_2 adsorption enthalpy and higher mesoporosity. *CrystEngComm.* **2011**, *13*(10), 3314-3316.

30. Yang, Q., Wiersum, A.D., Jobic, H., Guillerm, V., Serre, C., Llewellyn, P.L. and Maurin, G., Understanding the thermodynamic and kinetic behaviour of the CO2/CH4 gas mixture within the porous zirconium terephthalate UiO-66 (Zr): a joint experimental and modelling approach. *J. Phys. Chem. C*, **2011**, *115*(28), 13768-13774.

CHAPTER 2: LITERATURE REVIEW

2.1 Design and Synthesis of MOFs

MOFs are also known as porous coordination polymers (PCPs); these are frameworks, which consist of metal centres and multidentate organic ligands. In the 1990's, a few infinite coordination polymers were synthesised by Prof. Richard Robson. After finding in 1969 that several coordination compounds such as Ni (4-Me-pyridine)$_4$(NCS)$_2$ could be used for gas adsorption, the idea arose of using metal-organic coordinating bonds to form porous materials. Through coordination polymerisation, Robson popularised construction of such porous materials [1-3]. Since then there has been vast progress in the study of MOFs. Metal ions and organic connectors can be combined to produce an essentially infinite number of structures. To date more than ten thousand MOFs have been synthesised, researched and investigated while applications of those MOFs, such as catalytic application potential [4-6], chemical sensing [7,8], energy storage & conversion [9-11], drug delivery and bio-imagery [12-14] and optoelectronics/ferroelectronics [15], nonlinear optics [16], and light emitting diodes (LEDs) [17]), have also been discovered and reported.

Conventional methods used for the synthesis of MOFs include solvothermal processes, where autogenic pressure is exerted in completely closed vessels, as well as methods for reacting under atmospheric pressure, known as the solvothermal method. Various methods have also been employed for synthesising MOFs with different sizes and morphologies, as shown in Figure 2.1: microwave-assisted, electrochemical mechanochemical and sonochemical methods [18].

**A large portion of this section is taken from the review paper mentioned in the publications section. The author played a significant role in the surveying, organisation and proof-reading of the review paper.*

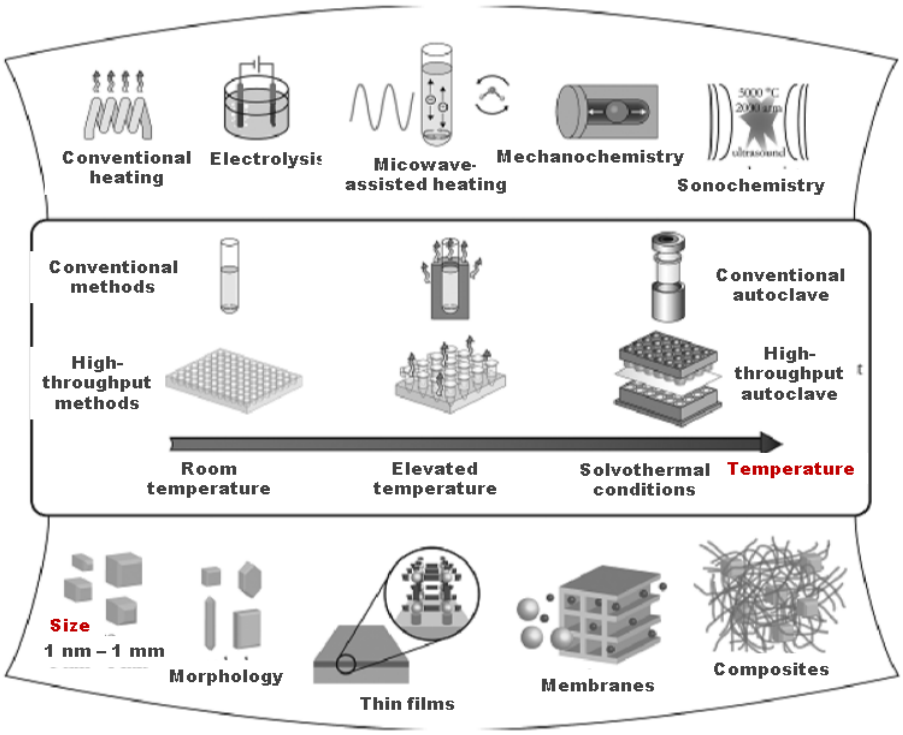

Figure 2.1. Methods of synthesis, potential temperatures and finished products. Reprinted with permission from Ref 18.

The solvothermal method is essential for the synthesis of MOFs, as it is a powerful technique for the development of single crystals vital for structural determination. Without knowing their crystal structures, the properties of MOFs are extremely difficult to interpret. One of the most significant features of MOF synthesis is therefore the growth of single crystals so that we may be able to understand their crystal structures. Metal salts and organic linkers are usually mixed in appropriate concentrations and modulators, which are structure-directing agents included in the solution to promote the growth of crystals. A few parameters affect crystal formation, including but not restricted to (1) the concentration and ratios of the metal salt and organic connectors; (2) the major solvent, (3) the polarity of the solvent, which can be modified with an addition of a small fraction of a second solvent, (4) the chosen modulators, which can affect the crystallinity of the final product and (5) conditions such as the temperature, the reaction

time and cooling rate. The size, quality and even phase of the resulting crystals can be affected by very small variations of these parameters.

In general, the reactants are separately dissolved in two immiscible solvent layers. After a few days at room temperature, crystals begin to grow at the layer interface. The two main aspects that affect the product are the selection of solvents for each layer and the concentration of starting material in each solvent. MOFs with various topologies and dimensionality (i.e. one dimensional (1D), two dimensional (2D) or three dimensional (3D) structures) can be formed based on different methodologies. Figure 2.2 shows how possible mixtures of metal ions and organic polydentate ligands can form 1D, 2D and 3D MOFs [19].

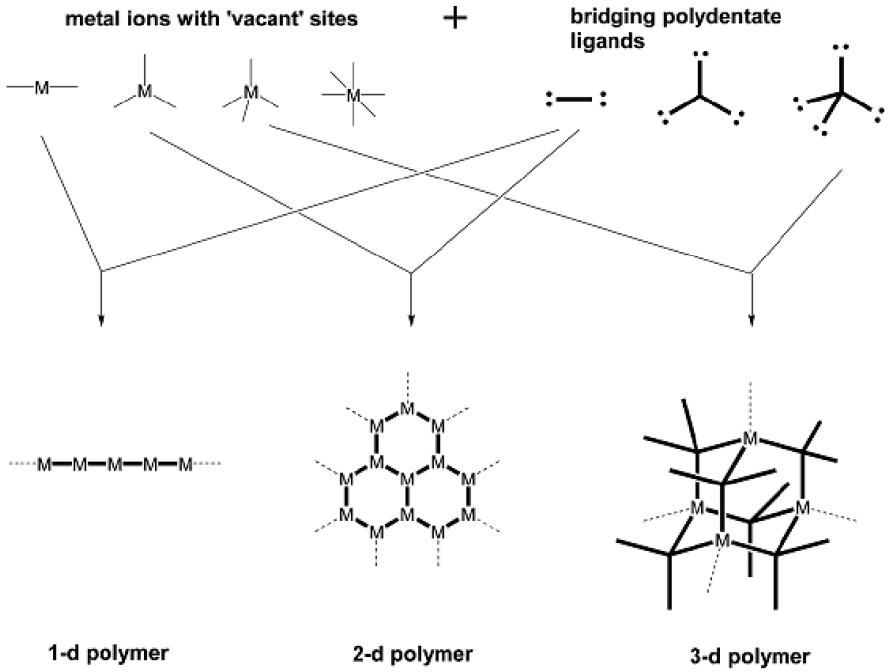

Figure 2.2. The building block, or 'modular' approach behind the formation of coordination polymers. Reprinted with authorisation from Ref 19. Royal Society of Chemistry.

The metal ions shown in Figure 2.2 can be replaced by complex structural units such as metal ions, metal clusters and metal-organic molecules (Figure 2.3) [20]. **A** consists of a single metal ion building block (may also be referred to as the primary building unit), **B** consists of a number

of metal ions called a secondary building unit (SBU), and **C** is assembled by several SBUs and is known as a super building block (SBB). The paddle-wheeled building unit is among the most common SBUs. The coordination geometry of each metal in a paddle-wheel unit is square pyramidal. Two metal ions are shared in a paddlewheel-shaped motif by four carboxylate groups which are situated on the equatorial plane. Each metal ion coordinates apically to a different molecule which may be a monodentate terminal molecule or a polydentate linker.

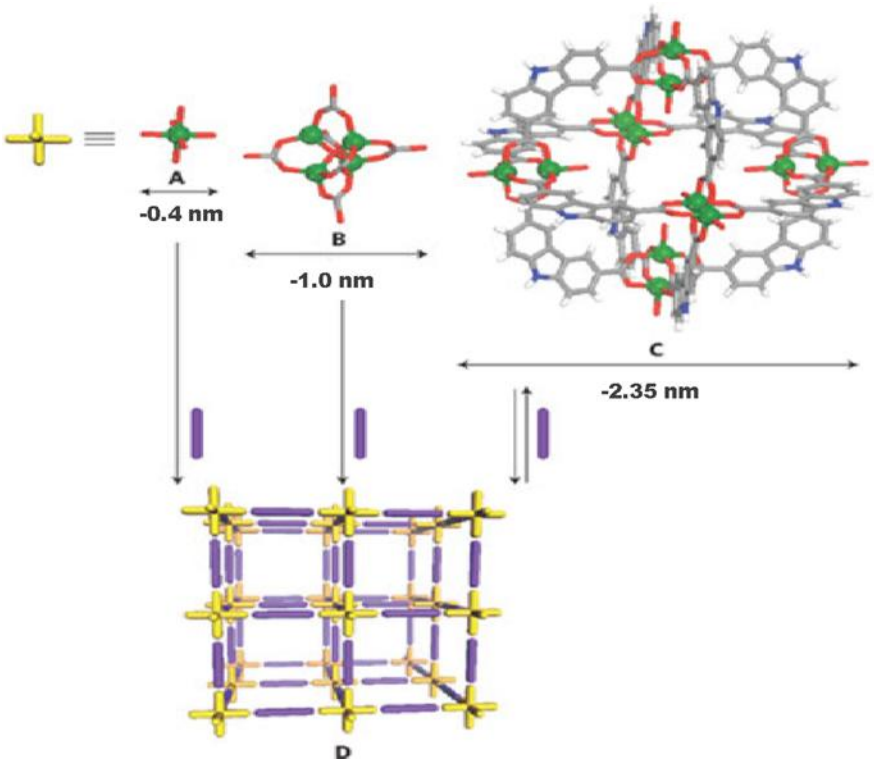

Figure 2.3. A linear ligand (purple spacing) joining a range of octahedral building blocks (yellow clusters) such as cations (**A**), metal clusters (**B**), or octahedral metal organic molecules (**C**) can be fashioned to form porous primitive cubic networks (**D**) (metal, green; oxygen, red; nitrogen, blue; carbon, grey; hydrogen, white). Polyhedral building components such as **C** provide a great level of control over the resulting structure and can be assembled step-by-step in a reversible way. Reprinted with permission from Ref. 20.

2.2 Characterisation of MOFs

The phase purity of the powdered material is determined by means of measuring powder X-ray diffraction (PXRD), i.e. by correlating the PXRD pattern of the powder sample to that simulated from single-crystal data.

Thermogravimetric analysis (TGA) measures thermal stability. As mentioned in an earlier section, guest molecules are usually embedded in the pores of the as-synthesised MOFs. The guest molecules leave the heated structure, causing a decrease in sample mass. The amount of guest in the structure can therefore be determined from the decrease in weight %.

Single-crystal XRD is an important tool for the identification of MOF structure. High quality single crystals of sufficient size are required to produce diffraction patterns from which the crystal structures can be resolved. Synchrotron radiation provides the most intense X-ray beams, allowing suitable diffraction patterns to be recorded for crystals smaller than 50 μm.

MOFs with permanent pores that maintain their structural integrity after the complete removal of guest molecules typically have fascinating adsorption properties and are a suitable candidate for gas storage or separation applications. Surface area and porosity must initially be quantified in order to test their adsorption potential. The N_2 adsorption isotherms are generally used for the calculation of pore size distribution and surface area at 77 K (or 87 K Ar adsorption and 195 K CO_2 adsorption). The surface area can be measured with BET and/or Langmuir models according to the different adsorption patterns. The former uses an adsorption model with several layers and the latter uses a single-layer adsorption model.

The adsorption characteristics of a MOF material can be measured by the adsorption-desorption isotherms of selected adsorbates. The adsorption of a given adsorbate on a MOF adsorbent depends on the pressure at a certain temperature. The overlap of adsorption and

desorption isotherms indicates that the process is reversible and balanced. The Henry constant can be computed using the Henry equation from the linear region of the isotherm that corresponds to the interaction between adsorbed and desorbed molecules at low load. Different methods can be employed to calculate the adsorption steric heat from isotherms at different temperatures to approximate the interaction between adsorbent and adsorbent.

2.3 **MOFs for energy applications**

Conventional porous materials like zeolites, metal phosphates and metallic sulphides have been well explored for their applications as a molecular sieve or catalyst in the past 240 years [21]. Adsorption properties [22, 23] of MOFs have also been intensively studied, for example methane storage [24], H_2 storage [25, 26], CO_2 capture [27, 28] and the separation of hydrocarbons [29, 30]. MOFs offer the advantages of tuning structure and porosity by combining different metal centres, with organic ligands of various forms, lengths and functional groups, in comparison to conventional porous frameworks such as zeolites, which have been used in industry but have a relatively limited pore sizes and forms.

In accordance with the standards set for hydrogen uptake in MOFs, much effort has been devoted to understanding the factors that determine hydrogen adsorption capacities with a view to developing novel, harmless and suitable storage materials for hydrogen storage. Specific surface area (SSA), volume of the pore, pores and binding sites for hydrogen (metal and ligand) etc., are important factors. Although industry has been using zeolites and activated carbons for decades, certain issues remain to be resolved. For instance, only certain structural types are confined to the natural and synthesised zeolites, leading to limited pores and forms. Furthermore, the interior surface of the zeolites cannot be modified to offer multiple functionalities. Activated carbons are amorphous materials, so characterising their structure is extremely challenging and it is difficult to correlate structure with properties. MOF structures

can generally be evaluated using single-crystal XRD. Their pore sizes, forms and internal surface functionalities can be engineered using different organic linkers and metal centres and in that way the adsorption properties can be tuned. For example, MOFs with even more open metal sites and Lewis base sites have proven to have a greater affinity for CO_2 in carbon capture from flue gas mixtures, which means that they can have a greater CO_2/N_2 separation factors [29]. This has led to a great deal of effort to produce MOFs with high densities of open metal sites.

Hydrogen is a desirable clean energy carrier, and feasible on-board implementation requires high gravimetric and volumetric hydrogen storage materials. Successional hydrogen-based DOE programmes have significantly stimulated research into hydrogen storage. Hydrogen storage by MOFs was first established in 2003 [4] (Figure 2.4). Several porous MOFs have shown much promise as adsorbents of hydrogen, and there has been a substantial growth in MOF research for high-capacity hydrogen storage. To date, MOF-210 with its high surface area has shown the best hydrogen storage capability with a total H_2 gravimetric uptake of 17.6 wt. % at 80 bar and 77 K. Although total gravimetric H_2 (77 K and high pressure) storage capacity has been projected as directly related to MOF surface area, it cannot be increased substantially due to synthetic problems in attaining MOFs with larger surface areas. The hydrogen storage at open metal sites (OMS), alkaline or alkali earth-metal ions (for example, Li^+ and Mg^{2+}), metal nanoparticles and small pores can likewise enhance hydrogen storage performance of MOFs [3]. These MOF adsorbents can achieve the required hydrogen capacity at low temperatures, however reaching the DOE hydrogen storage goal at ambient temperatures remains a great challenge. In order to obtain MOFs possessing suitable pore sizes, a bottom-up strategy is recommended whereby copper paddlewheels are combined with ligands containing 3,5-benezedicarboxylic acid moieties. This often yields frameworks with rhombi-cuboctahedral super-molecular building blocks (SBBs) that are 9Å in diameter [3]. Many

MOFs with suitable pores for H_2 are constructed in this approach [3, 26]. Their high H_2 storage capacities are tabulated in Table 2.1.

Table 2.1 Hydrogen uptake by various MOFs [25]

Compound	**H_2 uptake (wt %)**	**Temperature (K)**	**Pressure (bar)**
MOF-5	10	77	100
MOF-177	7.5	77	70
IRMOF-6	4.63	77	45
IRMOF-8	3.4	77	33.7
SNU-4	3.7	77	50
Mn-BTT	3.9	77	90
Cu-BTT	3.7	77	90
Fe-BTT	4.1	77	95
Ni-MOF-74	2.95	77	10
Co-MOF-74	3.15	77	10
HKUST-1	3.6	77	50
SNU-5	5.22	77	50
SNU-6	100	77	70
PCN-6	1.9	77	1
PCN-6’	1.1	77	1
PCN-10	6.84	30	3.5
PCN-12	3.05	77	1
PCN-12’	2.4	77	1
PCN-20	6	77	3
PCN-46	7.2	77	60
PCN-66	6.65	77	45
PCN-140	6	77	20

In recent times, there has been renewed interest in the chemical and materials science sectors in applications of MOFs for fuel storage, batteries, fuel cells, photo-induced hydrogen production and supercapacitors. Exploration of the different applications of MOFs has revealed that they are favourable for the storage and conversion of energy.

The demand for new energy technologies has prompted studies aimed at identifying the best photo- and electrochemical properties in porous materials that can store energy carriers or assist rapid mass and electron transport for energy storage and conversion. The main factors for evaluating energy system performance are appropriate surface area, coherent pore-size distributions, preferred morphology and higher functionality. MOFs have very porous structures, uniform spatial dispersion of components, tunable pore dimensions and topologies, and have hybrid organic/inorganic character and multifunctionality [31, 32], therefore surpassing other porous substances in energy applications. Moreover, a well-defined structure aids in rationalising the relationship between structure and properties, which is an essential aspect of materials optimisation.

The outstanding ambient-temperature gas storage capacity of MOFs has been driving rapid growth and providing many novel adsorbents with prospective applications in fuel cells, fuel tanks and stationary power facilities [33,34-38]. Photo and electroactive ligands and metal ions in MOFs may be utilised to stimulate energy-related chemical reactions in alternate energy cycles as energy acceptors or catalytic sites [39, 40- 54]. Effective approaches to the logical design and modification of these materials became possible with the advent of nano-technological and modern characterisation facilities [45-47].

2.4 **Background on UiO-66**

The archetypal MOF UiO-66 is the focus of this study. Originally reported by Lillerud's group a decade ago, it was first synthesized in the University of Oslo, so it is named after the university. Karl Petter Lillerud and co-workers first reported the synthesis procedure, as this was the first generation of Zr-based MOF, there was much exploring to do in terms of fine-tuning the recipe to achieve the best possible attributes as well as learning the mechanisms behind the synthesis. [48]. UiO-66 is a crystalline MOF composed of metal nodes consisting of a zirconium oxide complex bridged by terepthalic acid ligands. A representation of this structure is shown in Figure 2.4 [31]. In its most stable state, known as the hydroxylated form, the UiO-66 crystal is face-centered cubic with $Fm{-}3m$ symmetry and a lattice parameter of 20.7 Å. It has two distinct cages (a 7.5 Å tetrahedral cage and a 12 Å octahedral cage) and a pore opening of 6 Å. The zirconium oxide node in UiO-66 is classified as cuboctahedral, permitting the coordination of up to 12 extension points for BDC linkers. Half of the eight oxygen atoms in the hydroxylated version of this SBU are bound as individual atoms to three zirconium atoms, and the half are bound in hydroxide form to three zirconium atoms. The metal cluster is critical to the exceptional stability of UiO-66. It consists of an inner $Zr_6O_4(OH)_4$ core in which the triangular faces of a Zr_6 octahedron are alternatively capped by μ3-O and μ3-OH groups. Puchberger et al. [49] reported the same inner core of Zr_6 clusters as isolated units, with all polyhedron edges bridged by carboxylate groups ($-CO_2$) of dicarboxylic acids to form a $Zr_6O_4(OH)_4(CO_2)_{12}$ cluster. Owing to its high coordination numbers, UiO-66 exhibits exceptional thermal, chemical and mechanical stabilities. Furthermore, 12-coordinated UiO-66 allows the introduction of an unusually high degree of structural defects without undergoing structural collapse [31]. Due to its unusual tolerance for defect concentrations, UiO-66 was chosen as the material platform in this project for investigating the impact of defects on the chemical stability and gas adsorption by defective MOFs

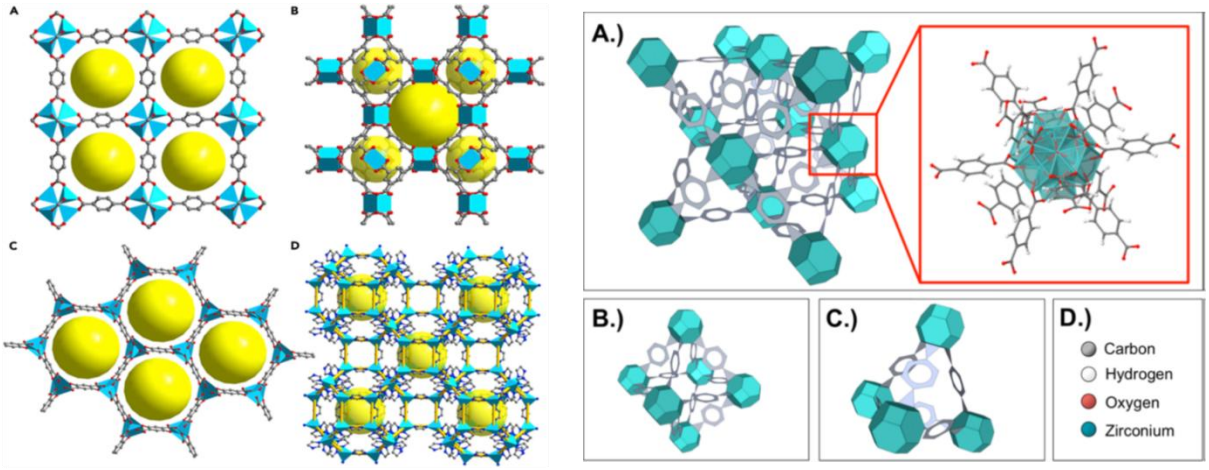

Figure 2.4. Left panel: Crystal structures of four representative MOFs, (A) MOF-5, (B) HKUST-1, (C) Mg-MOF-74, (D) ZIF-8. Colours: C, grey; O, red; and N, blue. The yellow sphere signifies the porosities, and the yellow cylinders display the topology of ZIF-8. Reprinted with permission from Ref. [50]. Right panel: An illustration of the UiO-66 structure. (A) The fcc UiO-66 structure composed of the metal node (blue) and ligand (gray) with an atomic representation of the node and 12-connected terepthalic acid linkers. (B) The node and ligand structure with the 12 Å UiO-66 octahdron cage. (C) The node and ligand structure with the 7.5 Å tetrahedron cage. (D) The color scheme for the atomic representation. Reprinted with permission from Ref. [31].

2.5 **Designation and classification of defects**

Recently, coordination network compounds (CNCs) have been reported to possess many systemic disorders and heterogeneities which break up the periodic atomic arrangements [51-52]. Goodwin and collaborators have defined [53-55] the topology [56-62] of the disordered CNCs [50, 63] based on the kind of building blocks, the connectivity patterns, the frequency and the atom/unit subtleties. Various techniques for the variation of building blocks within the framework lattice or in the pores have been shown to create heterogeneity without losing long-term order. In addition to this, a strategy was proposed as a viable approach to tuning the

properties of such materials. The incorporation of different types of organic linkers, or a combination of homologous linkers with specific chemical functions, as well as the combination of different metal-containing SBUs or more than one kind of metal ion with the same topological function inside a single MOF structure are desirable approaches to modifying the properties of such materials. [51, 52]; In the same way, defects may fundamentally be regarded as a specific heterogeneity, which means the elimination of some structural elements.

We defined CNC/MOF defects as sites where the periodic arrangement of atoms or ions in the static crystalline parent is interrupted as a result of missing or dislocated atoms or ions (Figure 2.5). Thermal motion or linker rotation of the constituent atoms is not regarded as a defect. In addition, a modification of parent framework which tends to occur periodically or homogenously, results in the formation of a daughter framework consisting of unsaturated coordination of the structure in the parent MOF.

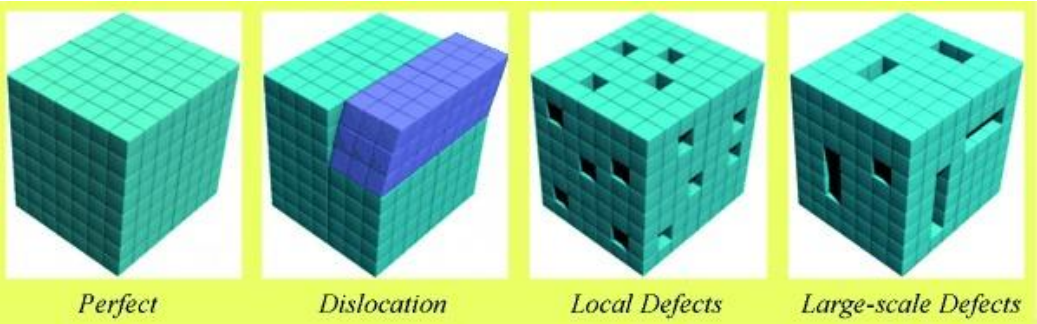

Figure 2.5. Defining defects: missing and improperly located atoms cause vacancies and material dislocation. Reprinted with permission from Ref. [64].

All structural discrepancies in solid matter are characterised in terms of their parameters in three chief areas: point defects (e.g. vacancies), line defects (e.g. delocalisation), planar defects (e.g. borders, and stacking defects). In addition, macropores, foreign inclusions and cracks created during solid production and treatment can also be perceived as macroscale volume deficiencies. These classifications could possibly be considered for CNCs as well. Defects may

be referred to as external or surface [65-68], or internal defects [69-76], depending on their locations.

These defects may be caused by partly missing metal nodes or links, which disrupts the regularity of the framework locally [73, 76, 77]. For defective CNC/MOF the charges are compensated, if necessary, either by reducing/oxidising framework elements [74, 76-78] or by including/removing counter-ions [30] during synthesis or post-synthesis. The creation of linker vacancies can also result in the occurrence of altered co-coordinatively unsaturated metal sites (mCUS) [74, 75, 78, 80] or additional CUSs [71, 76, 79-82], which may differ considerably from the systematic CUSs. Such mCUS can therefore also be characterised as point defects. The distribution, size and correlation/interaction status of deficiencies in this context may be categorised into two groups: a) local defects, which are, point or isolated faults and b) large-scale faults (e.g. mesopores; Figure 2.5). Two different cases may arise, depending primarily on the volume of defects within a structure and the effective size of the defect field. A random allocation of isolated or point defects can be identified at small defect concentrations and miniscule defect fields. In contrast, high default levels and/or relatively large defect fields can lead to correlated or large-scale defects by clustering point defects. Correlation implies that the likelihood of a defect emerging anywhere in the crystal lattice largely relies on the existence of defects nearby. As a result, correlated linker/node vacancies can create mesopores which can significantly disturb the pathways for mass transport (sorption and catalysis), can diminish network inflexibility and density, produce unique electronic, magnetic and optical properties, and may cause inconsistent mechanical properties (e.g. negative thermal expansion, pressure-inducing softness, and crystalline-amorphous switching). For example, reorganised CUSs that can operate in a cooperative way may bring benefits in the implementation of complex, catalytically active sites [83-84] for targeted catalytic reactions.

2.6 Formation of structural defects in MOFs

A simple knowledge of the defects in MOFs shows that they only occur randomly during the synthesis of MOFs. But studies by Cliffe et al. [73] indicated that defects in MOFs could be introduced and controlled effectively and intentionally. They demonstrated this using the hafnium terephthalate MOF illustrated in Figure 2.6. There have been several studies which have proven that nano-sized materials, nanofibers and graphite affect the properties of MOFs and therefore impact their applicability [85-87]. Some ways of introducing defects in MOF structures have been demonstrated in the literature (Figure 2.7) [86, 84-88]. These techniques can be limited to two main paths, namely: (a) during MOF synthesis and (b) post MOF synthesis.

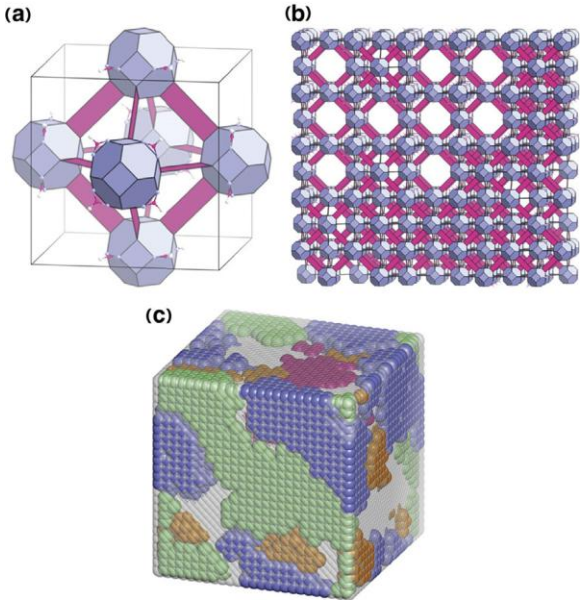

Figure 2.6. Structural description of UiO-66(Hf) defective nano-region. (a) Polyhedral illustration of the (ordered) reo defect structure single unit cell. (b) Defect-rich nano-regions are dispersed across the defect-free fcu matrix. (c) Atomic depictions of defect nano-regions in UiO-66(Hf) may be used for defect concentration and domain size parameters which were experimentally identified. Reprinted with permission from Ref. [73].

The synthesis of crystalline MOFs is sometimes tedious due to many attempts to combine metal ions with organic ligands frequently leading to amorphous products [89]. In 2009, in contrast to the less crystalline bulk material produced from conventional solvothermal synthesis, the Kitagawa group [90, 91] addressed the issues by manufacturing MOF nanoparticles of definite size, shape and greater crystallinity. In order to modulate coordination with metal ions, a modulator was included in the synthesis solution without simply acting as a bridging molecule but modifying the development of the framework. In general, different mechanisms of modulation are possible, for example, deprotonation of the linker molecule (deprotonation modulation) or coordination modulation (wherein the molecules of the modulator compete with the linker molecules for the coordination sites at the inorganic building units).The modulator competes with the BDC ligands for the Zn^{2+} cations via a self-assembly incorporation principle. In deprotonation modulation, the modulator acts as a base thus enhancing the deprotonation of linker molecules and assisting in the attachment of linker molecules to the inorganic building units (IBUs); this results in the formation of a MOF framework to be accelerated . In the concept of coordination modulation, the modulator competes with the linker molecules for the coordination sites at the IBUs. In this way, the formation of amorphous precursors or zirconia gel when the reaction begins is circumvented. Nucleation and growth can then happen from dissolved species and then continue at a reduced rate due to the necessary exchange of the coordinated modulator with bridging linker molecules, i.e. reaction rates are decreased. Correspondingly, also the number of nuclei formed is small; which can grow to larger crystals, thus the size control [92-93]. To date, modulation synthesis has been employed as an efficient way of increasing the reproducibility of the synthetic process, improving the crystallinity of the MOFs, as well as the facilitating control of material properties [94].

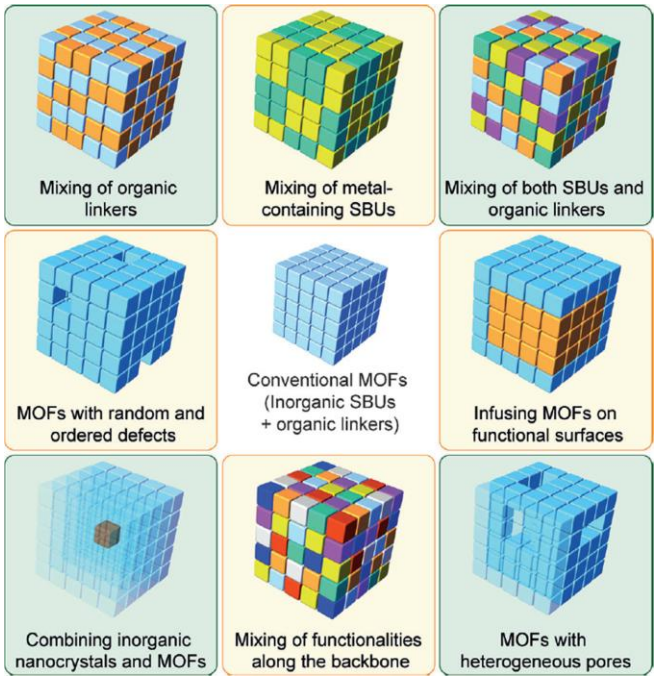

Figure 2.7. Different strategies to introduce defects in MOF structures. Reprinted with permission Ref. [88], Copyright © 2015 Wiley - VCH Verlag GmbH & Co. KGaA, Weinheim.

Control of defects by modulated reactions is commonly known as 'concentration of defects control' or 'arrangement of defects control'. Differences in solvent system, nature of the modulating systems, quantity of modulators and nature of the metal centres are imperative aspects that are mentioned in the literature.

2.6.1 Solvent systems

Kim et al. [95,96] described post-synthetic exchange in UiO-66 for a range of solvents (H_2O, DMF, MeOH and $CHCl_3$), resulting in different linker exchange yields. With some exceptions, the PSE studies published so far have concentrated on comparing the parent material and the samples that have been exchanged, with little insight into the mechanism at the molecular level. Therefore, several questions remain unanswered about the ligand exchange process, including its kinetics, the ratio of outgoing and incoming linkers, as well as the position of defects in the

structure, and solvent interactions [97]. However, factors such as the structure of solvents obviously play a big role in the exchange process.

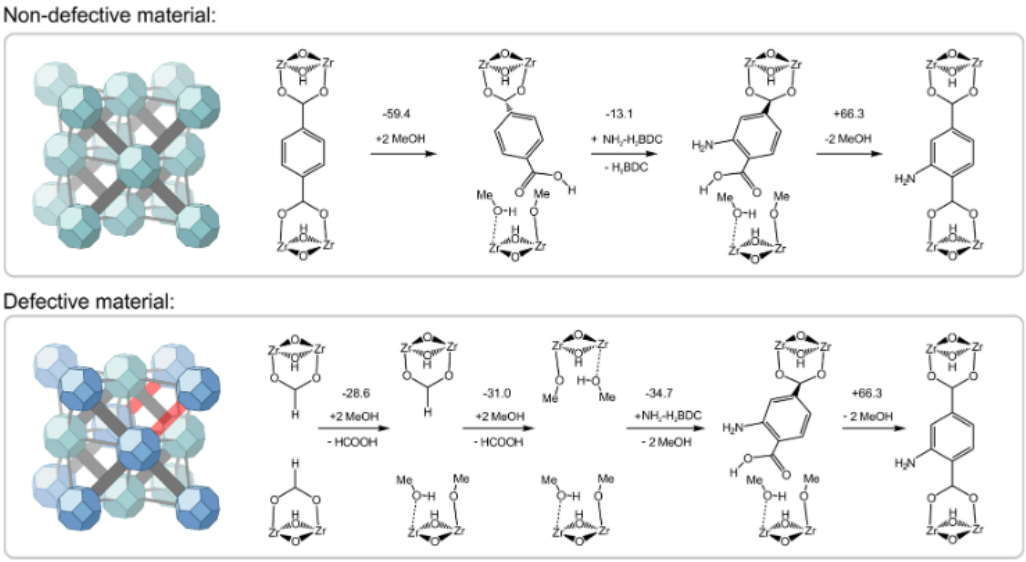

Figure 2.8. Proposed PSE process for non-defective and defective UiO-66. MeOH enables the exchange of ligands by the formation and stabilization of defects. Differences in enthalpy are given in kJ mol^{-1} at 313 K. Reprinted with permission from [98].

2.6.2 Nature of modulating systems

In order to test the role of the modulator, a family of UiO-66 MOFs had been produced under the same conditions with modulators other than acetic acid, namely formic acid, benzoic acid and trifluoroacetic acid. In the case of a given modulator / Zr ratio used in the synthesis, the total number of defects per node increased in the order of acetic acid < formic acid < benzoic acid ~ trifluoroacetic acid. The defects were created during the synthesis as the modulator and linker precursors (acetic acid, formic acid, benzoic acid, and BDC linker) competed for binding sites on the nodes while leaving some of these sites free. Trifluoroacetic acid (TFA) is a stronger acid (pKa = 0.23) than formic acid (FA, pKa = 3.75) and acetic acid (AA, pKa = 4.75) and it has been assumed that increasing the acid concentration of the modulator favors the development of a defect in the MOF [99]. Also, by varying the concentration of the modulator,

the linker vacancies can be tuned systematically, leading to dramatically enhanced porosity [100, 101]. If the modulator participates in the formation of the MOF structure, some modulators could remain within the structure and produce missing linker deficiencies in the principal structure [102]. Gutov et al. [103] conclusively proved that defects had a large reliance on the nature of the MOF synthesis modulator acidity in Figure 2.9, which showed unique and highly promising physical and chemical characteristics. Recent studies by Cai et al. [104] have demonstrated the synthesis of modulator-induced defective hierarchical (HP) MOFs with high stability and controllable pores. Their synthetic technique can also be modified for functionalised and extended UiO-66 structures as well as other several MOFs.

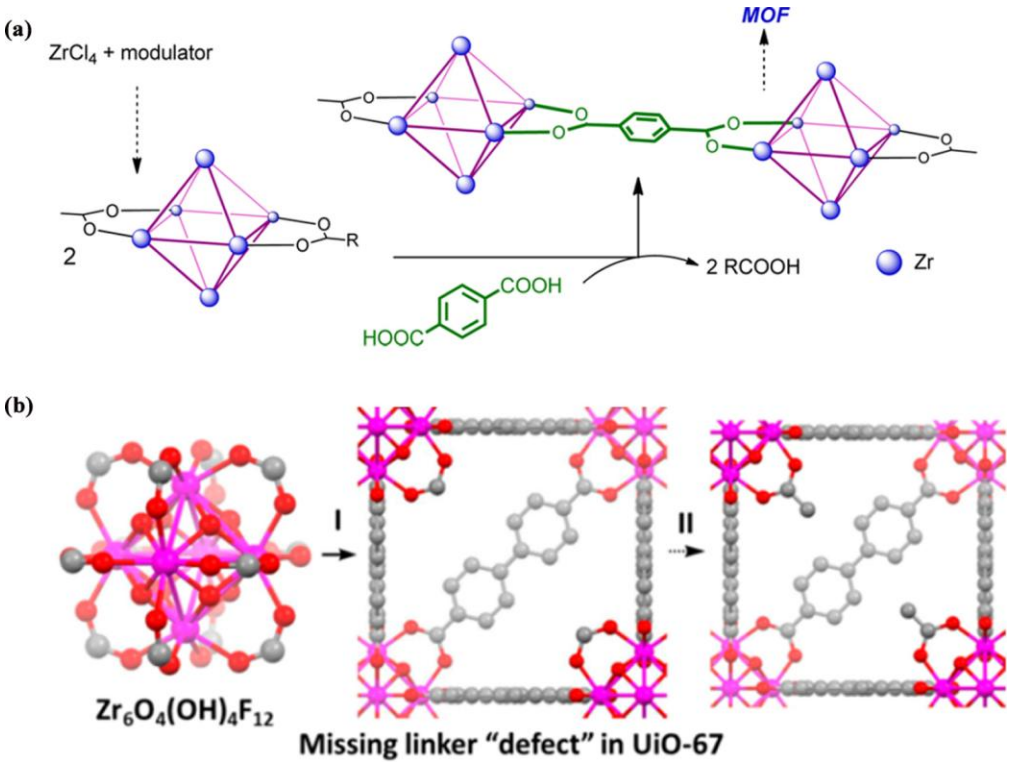

Figure 2.9. (a) modulated stepwise growth of the UiO-type Zr-MOF network. (b) The proposed reaction scheme for defective Zr-MOF development by means of H_2bdc as a ligand in excess formic acid modulator (reaction I), and the replacement of anions, capping defects, with organic acid (here, acetic acid) (reaction II). Reprinted with permission from Ref. [104].

Vermoortele et al. [76] illustrated their use of the synthesis modulation approach as a convenient means of increasing the chemical applicability of Zr-MOF by the addition of trifluoroacetic acid in the synthetic process. In the resulting materials, trifluoroacetate (TFA) groups substituted a portion of the terephthalate binders and thus created structural defects. In addition, because of the volatile and labile nature of TFA (bp = 72 °C), thermal activation of the Zr-MOF material resulted in the dihydroxylation and in the exclusion of the three-fluoroacetate groups, giving rise to a vast array of open sites as shown in Figure 2.10. Subsequently, Vandichel et al. [83] constructed free energy diagrams, which were used under actual synthesis conditions for rationalising modulators. Detailed studies of active site engineering may be founded on the application of theoretical rationalisation. Yu et al. [105] developed the two-photon MOF reacting crystal ZJU-56-0.20, using a photoactive linker to modulate the fluorescence feature of a MOF spatially. The defective MOFs can be used as data storage media, for two-photon imagery, 3D patterning and for sensor arrays.

2.6.3 Quantity of modulators

Li et al. (106) showed that the structural defects in MOFs resulting from the missing linkers can be methodically modified by altering the quantity of modulator in the synthesis reaction. The Zr-MOF synthesis modulator serves to modulate the crystal growth and assists in the establishment and promotion of defects. Other scientists [87,107] similarly reported on the impact of varying of the modulator/linker ratio and stressed that this influences the type of defects created, the degree of crystallinity and the morphology of the MOF.

2.6.4 The nature of the metal clusters

MOFs are materials formed via the coordination of metal clusters and organic linkers in three dimensions. Bristow et al. showed that as water / DMF was added to the UiO-66 synthesis mixture such that the Zr centers remain completely coordinated, the defect concentration was minimized. This confirms that undercoordinated metal centre is energetically unfavourable [108]. Although it is more complicated to apply a multivariate strategy to metal centres than to organic linkers, some work has revealed the possibility for developing multiple metal centres within one system and then forming defective MOFs with mixed-metal centres or mixed-metal MOFs (MM-MOFs) [52]. Mixed-metal centre defects (or cation defects) are one of the most common defects in MOFs. Heterometal clusters or ions are intentionally introduced into a MOF framework while retaining the structural integrity in the actual long-range order [54]. There are two synthetic approaches to achieve the formation of this type of defect in MOFs.

2.6.5 Inherent defects

As a result of stacking failures or dislocations, inherent defects arise during crystal growth and may occur without specific engineering. It also means that, in addition to mixing the ordinary parent framework building blocks under regular synthetic conditions, no other manipulation needs to be done during the synthesis. CNC/MOFs are susceptible to the development of inherent deficiencies caused by misconnection or dislocation during crystallisation [67] or by post-crystallisation cleavage [19]. Inherent defects are also found in several MOFs as free pendant linkers or missing linkers. Indeed, the rise in the temperature of the reaction and starting metal proportion can significantly lower the concentration of the reactive vacancies [109], which could lead to the formation of vacancies. Clearly, rapid development may not provide enough time to conform quantitatively to the developing crystal lattice in the correct location, and defects cannot be rectified when the coordination bond is not adequately

reversible. In fact, the rapid crystallisation of IRMOF-3 and MOF-5 gives rise to the formation of terephthalates, with simultaneous interior surface decoration, as shown by FTIR [109]. This is an easy and convenient way of deliberately producing new acidic and hydrophilic catalysts different from the parent MOF. Some of the authors studied inherent defects in MOFs in membranes and thin films and highlighted the significance of the monolayer self-assembled membrane (SAM) used because their contamination or defective structure may lead to significantly faulty SURMOFs [110, 111].

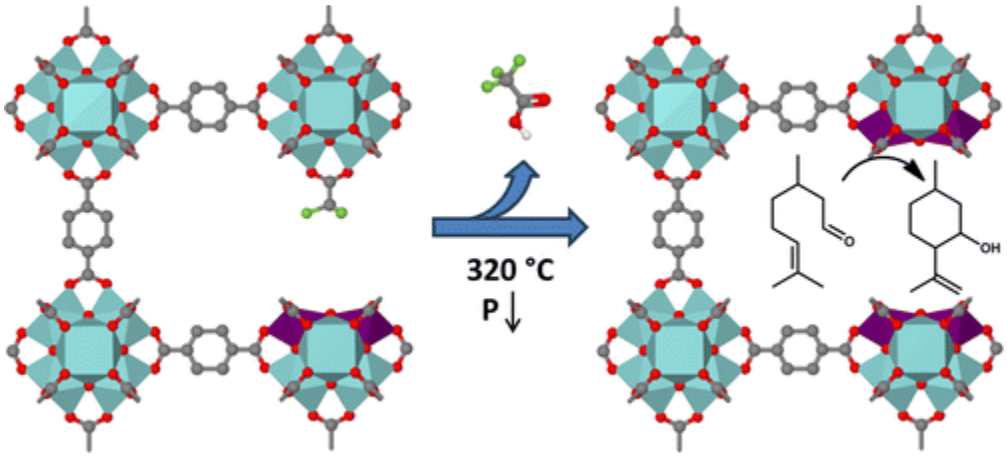

Figure 2.10. Schematic showing thermal removal of TFA from UiO-66 creating open sites. Reprinted with permission from Ref. [76].

2.7 **Defect engineering**

It is still challenging to directly introduce defects into MOFs, i.e. synthetically control the concentration of defects and their chemical nature. Two synthetic methods are generally employed for preparing MOFs with different defect types: (i) de novo synthesis and (ii) post-synthetic processing. Figure 2.11 provides a schematic description of all methods used to produce MOF defects.

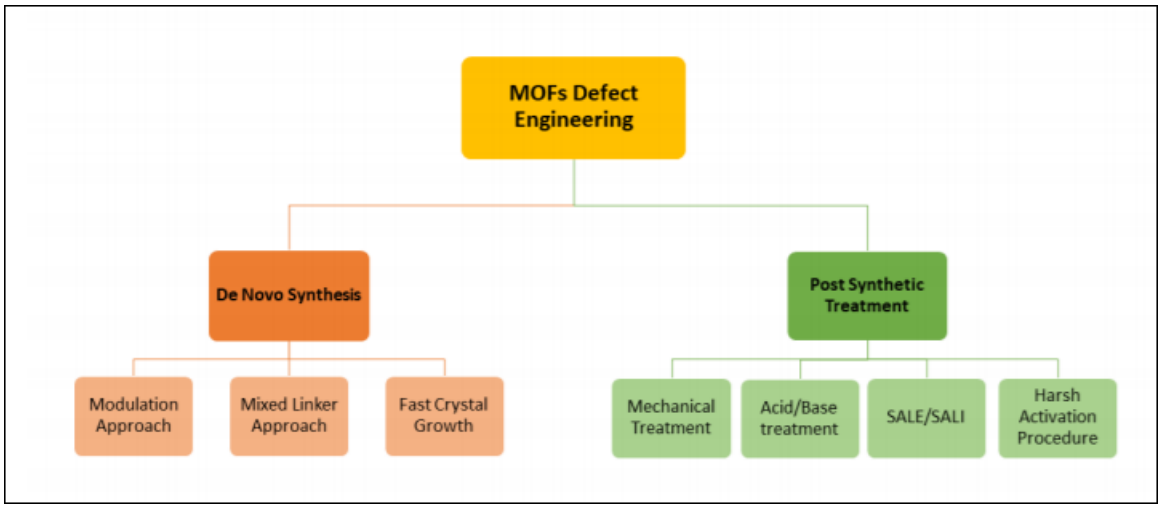

Figure 2.11. Representation of all key MOF defects procedures. Reproduced with permission from Ref. [112].

2.7.1 Defects formed during de novo synthesis

To date, the most popular de novo strategy to the synthesis of defective MOFs, besides varying the linker molecules in the course of MOF synthesis, entails adding large amounts of monocarboxylic acids. This "modulation approach" is a synthetic method utilised to reduce the speed of MOF crystallisation in order to achieve a greater degree of crystallinity. Today, it is recognised that minute quantities of monocarboxylic acids, the modulator, slows down the crystallisation process and produces a material that has fewer defects, whereas high concentrations of the modulator potentially lead to a higher concentration of defects. Ravon et al. reported the first use of this approach in 2010; they used 2-methyl-toluic acid as a modulator for synthesising MOF-5 [70]. Since then, several groups have synthesised defective MOFs using formic acid (FA), acetic acid (AA) or trifluoro acetic acid (TFA) and its derivatives as typical modulators (see Figure 2.12, left panel).

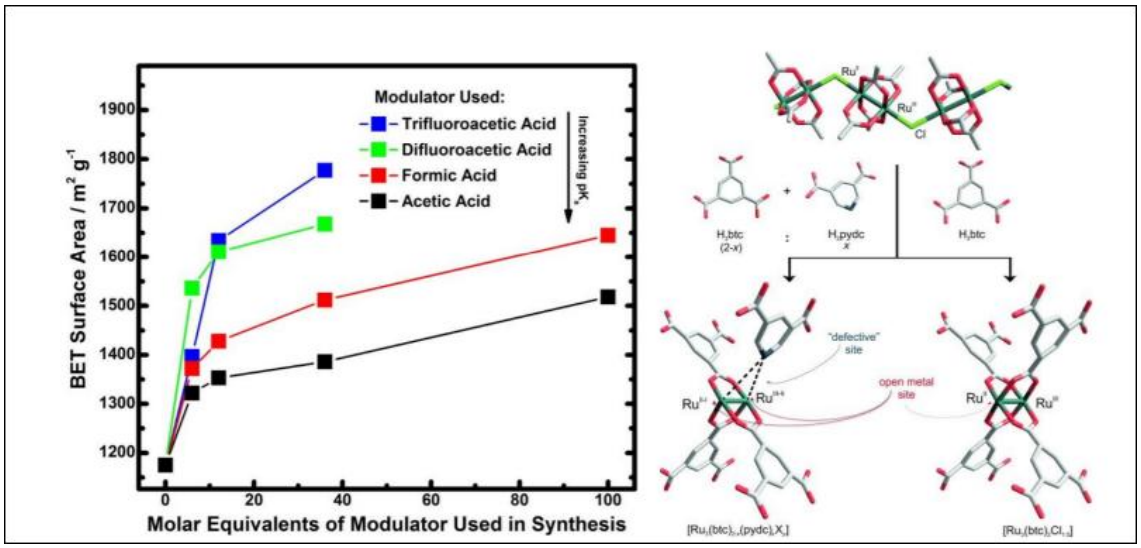

Figure 2.12: Left panel: An indication of the number of Zr_6 formula deficiencies in UiO-66 in relation to different modulators. Reproduced with permission from Ref. [87]. Right panel: Ru-HKUST-1 mixed linker approach resulting in node errors. Reproduced with permission from Ref. [64].

In the course of their study, Vermoortele et al. [76] removed TFA using heat treatment at temperatures of 320 °C and created unsaturated sites that are highly reactive Lewis acid sites, which suggested the application of these systems in catalysis. It was not until 2016 that Shearer et al. systematically analysed the impact on default chemistry of UiO-66 [87] by using various modulators such as FA, AA, TFA and DFA. TFA proves to be most appropriate modulator for synthesising defective UiO-66 based on its pKa (which is solvent-dependant). The parent framework linker was substituted partly by a linker which possessed a different functional group (for example, 1,3,5-tricarboxylate (BTC3-) pyridine-3,5-dicarboxylate (pydc1-)) [80]. Figure 2.12 (right panel) demonstrates the work of Kozachuk et al. [78] based on the Ru-HKUST-1 approach. The parent framework connector is substituted partly by a linker with an alternate group. Rapid crystallisation results in the formation of point defects such as missing linkers and cluster faults. The result is a formal reduction in the number of Ru centres, caused by the conditions of the reaction [64]. To further increase the functionality of MOF-5 and

IRMOF-3 using such an approach, point defects may be substituted by other species (counter anions) of the MOF mother structure; e.g., OH groups in MOF-5 and IRMOF-3 MOF [114].

2.7.2 Defect formation by post-synthetic treatment

The following processes involve post synthetic modifications in which preformed MOFs undergo solid solution reactions or surface changes in order to integrate additional functionality. In place of establishing novel conditions for MOF synthesis [66], post-synthetic adjustments to the parent MOFs could incorporate various chemical functionalities into the existing MOF structures. Mixed-linker MOFs, mixed-metal MOFs or core-shell MOFs may result from solid-solution reactions. The variations induced offer the potential to adjust the pores, compositions and other characteristics. This topic was comprehensively examined by Burrows [52]. Secondly, post synthetic treatments would make it likely to produce a range of active defect locales for enhanced functionalities in MOF structures [116]. In UHM-3 surface assembled MOFs, Wang et al. [117] reported coordinated defects that are tunable and may be used for the adsorption and separation of gas. As illustrated in Figure 2.13, a solid substrate was produced with a liquid-phase epitaxy method by using an orientation-grown, homogeneous and virtually defect-free (less than 1%) UHM-3 MOF thin film. Then a post-synthetic thermal treatment was implemented for the controlled induction of Cu(I) defect sites. Thirdly, the existence of defects would give the existing MOF structures additional opportunity to carry out a secondary PSM phase. In some surface variations to the pre-moulded MOFs it would, for example, be possible to load catalyst-like materials effectively into MOFs [118–127]. Finally, several studies revealed that post-synthetic modification permitted certain materials not obtainable with other synthetic methods [128–130] to be achievable.

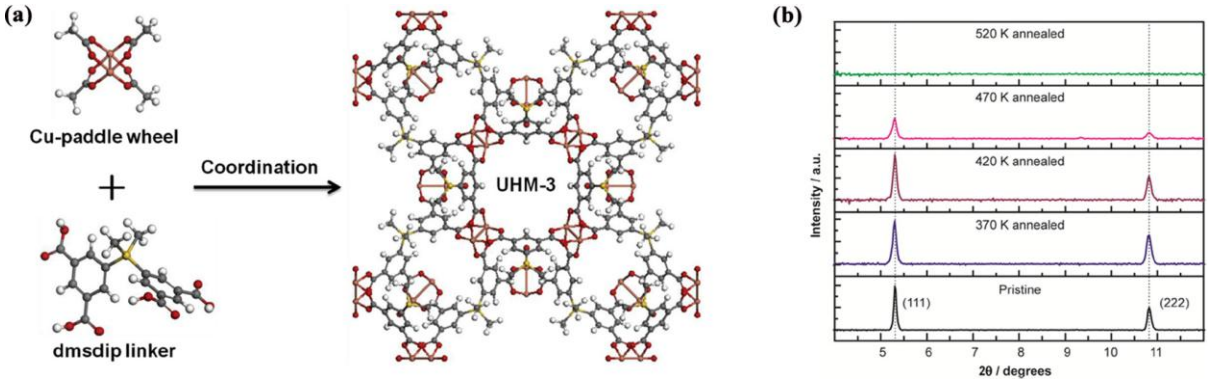

Figure 2.12. (a) UHM-3 ball-and-stick representation: oxygen (red), hydrogen (grey), carbon (dark grey), copper (magenta) and silicon (yellow). (b) PXRD patterns for UHM-3 SURMOF samples which were annealed at various temperatures. Reprinted with permission from Ref. [117], Copyright 2015 Elsevier Inc.

2.8 **Detection of structural defects in MOFs**

In view of the effects that defects have on the physicochemical properties of MOFs, increasing pores in the crystal structure and reducing the density and the thermal and mechanical properties of the material should be straightforward [131]. The first indication of structural defects or linker vacancies in the MOFs arise from the deterioration of thermal stability of the MOF structure which is considered 'deficiency free' [132]. Various techniques or a combination of these techniques have been utilised in the literature to detect any structural defects in MOFs. These include PXRD, high-resolution neutron diffraction (HRNPD), ultraviolet-visible (UV-vis) spectroscopy, thermogravimetric analysis (TGA), BET surface area (SBET) and pore volume (Vpore) measurements, Fourier transform infrared (FTIR) spectroscopy, electrospray ionisation mass spectrometry (ESI-MS), nuclear magnetic resonance (NMR) spectroscopy, single-crystal X-ray diffraction (SCXRD), atomic force microscopy (AFM), confocal fluorescence microscopy (CFM) and an integration of these techniques.

2.8.1 PXRD: The presence of prohibited symmetry reflections

The structural changes can be studied in detail by making use of PXRD, whereby one can compare the simulated XRD pattern of a non-defective MOFs to that of a defective material. Jakobsen et al. [133] found two large peaks with lower intensity, at 2 degrees below the (111) reflection (7.4° 2-theta) by comparing PXRD patterns of UiO-66 (Hf) and UiO-66 (Zr). Both of these peaks were due to prohibited reflections for the space group *Fm*-3*m*. When the MOF was activated, these peaks disappeared, demonstrating a solvent effect. Øien et al. [134] observed diffuse dispersions for UiO-66 in the anticipated positions of the symmetry-forbidden diffraction peaks, indicating that the defects and/or missing clusters are no longer in range. The earlier work [73, 135] elucidated this in detail. Also, the chemical stability of the MOFs can be analysed and monitored by using this technique.

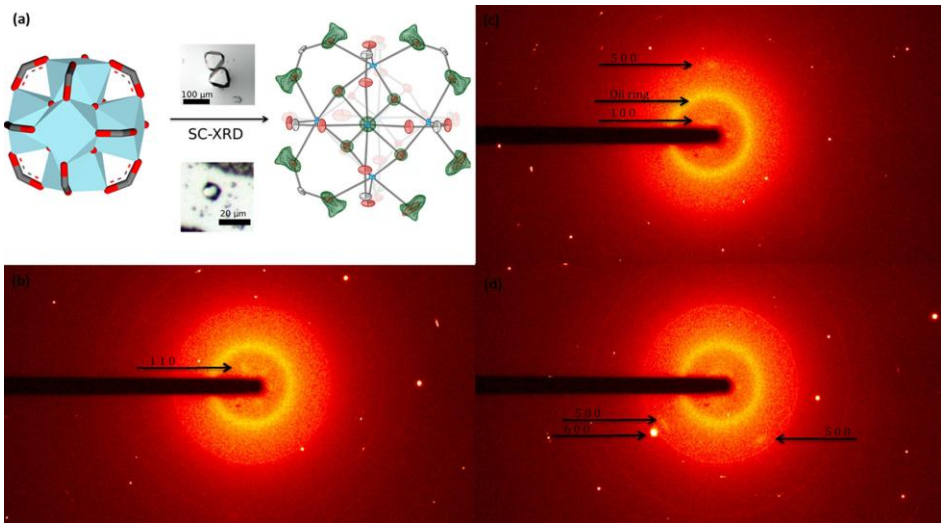

Figure 2.13. (a) Missing linkers in UiO-66 partial unit cells, (b) diffuse reflections (110), (c) diffuse reflections (100), (500), and (d) diffuse reflections (500). Reprinted with permission from Ref. [134].

Shearer and co-workers labelled two symmetry-prohibited reflections [72], as shown in Figure 2.15.

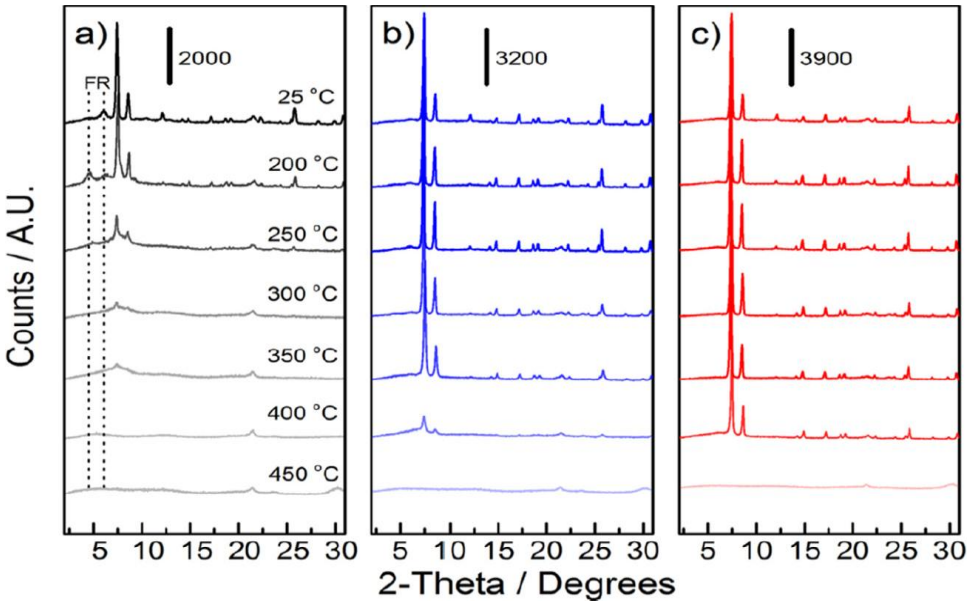

Figure 2.14. PXRD patterns recorded at various temperatures after heating UiO-66 samples for 12 h. (a) 373 K; (b) 433 K; (c) 493 K. The two reflections labelled 'FR' and marked out by vertical dotted lines are prohibited. Reprinted with permission from Ref.[140].

2.8.2 HRNPD: Presence of missing-linker defects

Wu et al. [69] conducted a high-resolution neutron powder diffraction examination on a UiO-66(Zr) deuterated sample made using a modulator method to detect the presence of missing linker defects in MOF structures. Compared to PXRD, neutron diffraction is considered a better choice given that it is more sensitive to the presence of hydrogen atoms in a structure [69,142]. Figure 2.16 shows measurements from neutron powder diffraction. It is acknowledged that sample deuteration is strongly recommended so that the incoherent diffraction background produced by an ordinary hydrogenous sample can otherwise be substantially eliminated and diffraction patterns of high quality can be obtained to monitor the structural information changes regarding the missing linkers.

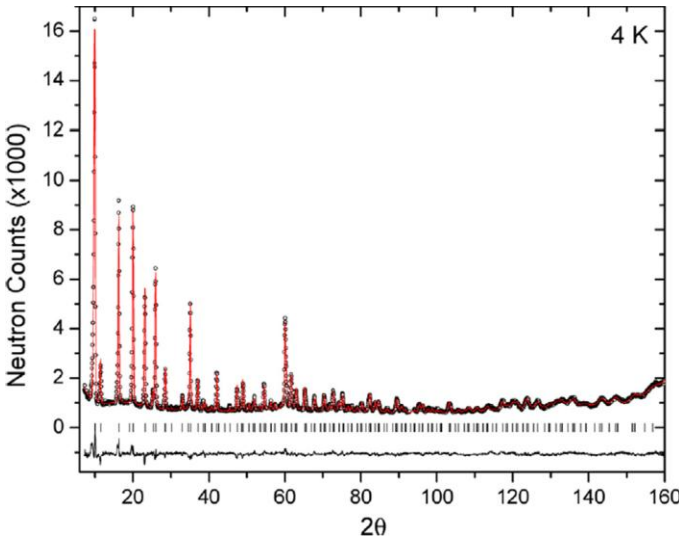

Figure 2.15. Experimental neutron powder diffraction profiles for dehydroxylated deuterated UiO-66 at 4 K (circles), calculated (lines) and difference (line underneath the observed and estimated patterns). The missing linker defects were identified in the structural model of Wu et al. by a linker occupancy parameter, of which 0.917 was the refined value. The estimated locations of the Bragg peaks were shown by vertical bars. Fitness: Rwp = 0.0452, Rp = 0.0364, χ^2 = 1.65. Reprinted with permission from Ref. [92].

2.8.3 DRIFTS spectra with vibrational modes

The ways in which the defects have previously been suggested to be compensated are by formate (via the decomposition of DMF), oxide, hydroxide, water, or chloride. Moreover, monocarboxylic acids can compensate linker deficiencies when heavily modulated synthesis procedures are used. DRIFT can therefore be used to determine whether the hydroxyl or water has replaced the missing linker as these additional bands would be present in the spectrum Szilágyi et al. [137] used the post-synthetic modification method on MIL-101(Cr) and DRIFTS spectroscopy to explain data on metal linkers (illustrated in Figure 2.17) in order to comprehend the nature and type of defects in MOF structures. Uncoordinated carboxylate groups were revealed in the -OH and C=O stretching modes. They also discovered that the vibrational changes were proportional to the functional group substitution and concluded that the defects

were thus an effect of dangling linkers. Certain vibrational modes were present only in the PSM sample. For PSM, the -OH stretching mode belonging to the carboxylate appears at 3301 cm^{-1}, the free C=O stretching mode appears at 1685 cm^{-1} (which is very similar to what was measured for the NH_2-BDC) [138] and the CH out-of-plane deformation mode appears at 848 cm^{-1}. These additional modes only exist in the post-synthetically modified sample, which means that defects have been incorporated in the pristine MIL-101. Additional −OH and C=O stretching modes display the presence of uncoordinated carboxylate groups.

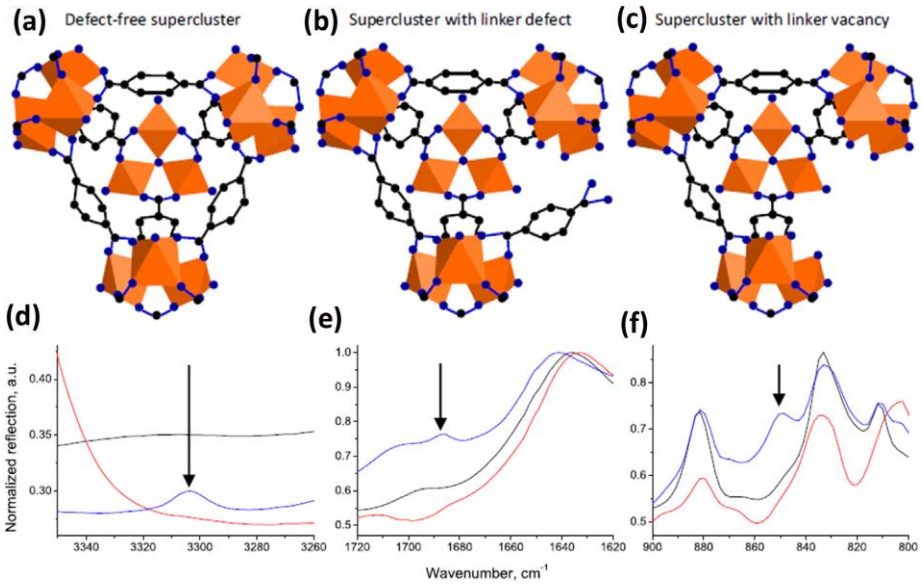

Figure 2.16. MIL-101(Cr) supercluster (a) defect-free, (b) dangling linker, and (c) linker vacancy; orange polyhedra represent cationic units, while black and blue represent C and O atoms. DRIFT spectra MIL-101 (black), NH_2-MIL-101 (red), and PSM (blue) in (d) -OH stretching, (e) C=O stretching, and (f) C-H bending regions. Reprinted with permission from Ref. [137].

2.8.4 TGA: less weight loss than theoretically expected

Dissimilar TGA results prove the non-stoichiometric structures of MOFs, and directly support the hypothesis that the frameworks do not include certain linkers. In this instance, during thermal decomposition, the measured loss of weight is often substantially lower than expected,

indicating lighter frameworks [141, 142]. As shown in Figure 2.18, at 300 °C the mass was regarded as dry mass for all samples, and this correlates with the point of dehydration and desolvation of the MOF [143], following the initial mass losses. Although it cannot be precisely specified stoichiometrically with TGA measurements, the physisorbed water and solvent molecules can be observed in the initial weight loss [144]. As reported, the loss of $ZrO(CO_2)(C_6H_4)$, per Zr atom, is observed as a plateau in the 573-923 K range of a TGA plot [143].

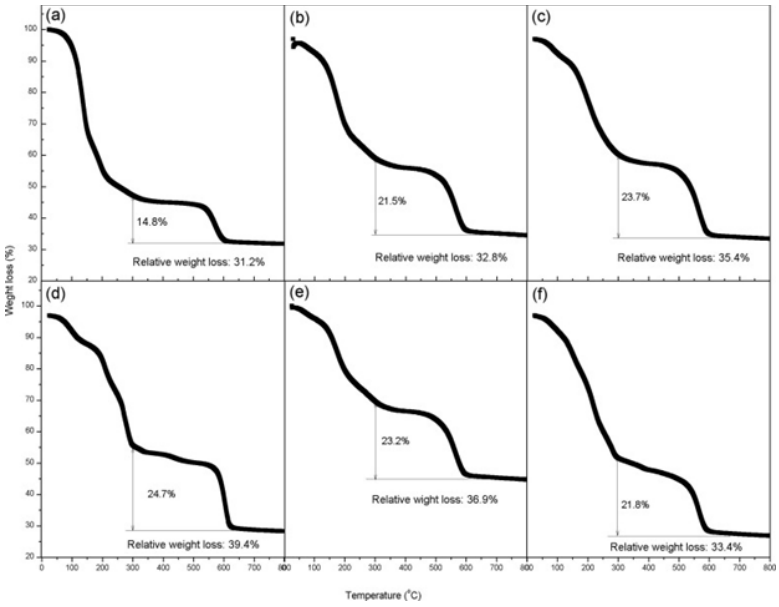

Figure 2.17. TGA thermograms of UiO-66(Zr) TGA curves for samples with reaction times indicated as: (a) 2 h, (b) 4 h, (c) 8 h, (d) 24 h, (e) 48 h and (f) 72 h. Reprinted with permission from Ref. [143].

A mass difference occurring between 300 and 650 °C can be attributed to the framework mass loss since the mass remains constant beyond 650 °C. At the end a theoretical mass loss of 54.6% should be attained for UiO-66, considering the breakdown of BDC linkers in relation to the mass at 300 °C. As illustrated in Figure 2.18, relative weight losses for reaction times of 2, 4, 8, and 24 h samples for UiO-66 are 31.2, 32.8, 35.4 and 39.4 weight % for each sample,

respectively, indicating that at shorter times there were more missing linkers in the materials as compared to longer times.

2.8.5 SBET/Vpore measurements

The amount of hydrogen that is adsorbed by a material is dependent on the surface area and pore volume. One reason MOFs are of high interest for gas storage is because of their large surface areas and studies continue to research better materials and modify existing ones in order to offer higher surface areas. Due to the defective MOF structures, gas adsorption might diverge from the expected behaviour of defect-free crystals [151,152]. The diffusion of gas into MOF materials may greatly be helped by the structural defects, as Psofogiannakis et al. [153] pointed out. The standard BET surface area and pore volume measurements are calculated from of N_2 (or He) gas sorption isotherms [154,155]. Because MOFs with missing ligand tend to have lower densities, defective MOFs show higher surface areas and pores volumes if the percentages of missing connectors are higher [156,157]. For example, for a defect-free UiO-66 crystal composed of $Zr_6O_4(OH)_4(bdc)_6$ the theoretical pore volumes (0.4 $cm^3.g^{-1}$) and the BET surface area (944 $m^2.g^{-1}$) are adequate. When one connector was removed artificially from each metal centre in the unit, the connector deficits induced porous structures, with a remarkably higher calculated pore volume (0.50 cm^3) and surface area of (1433 $m^2.g^{-1}$) [158]. Structural defects in MOFs can sustain the claim that the experimental BET measurements are significantly higher than the measured values [159]. UiO-66 simulated models where zero to six linkers per unit cell are missing (Figure 2.19a) had higher nitrogen adsorption. Moreover, the number of missing linkers per cell unit was linearly correlated to the surface area of the UiO-66 MOF material (Figure 2.19b).

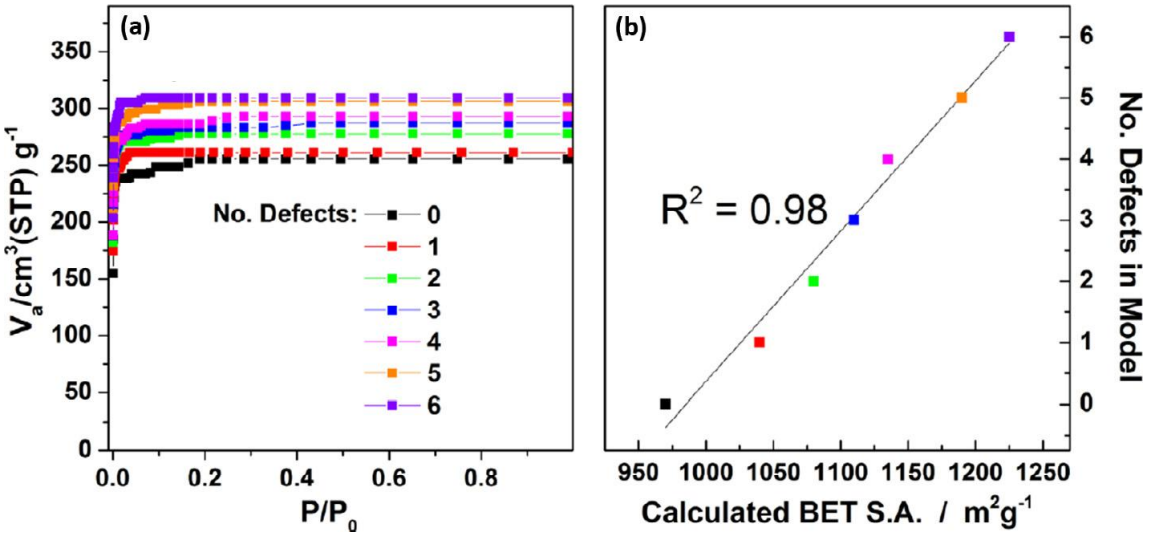

Figure 2.18. (a) Nitrogen adsorption isotherms simulated in UiO-66 models where 0–6 linkers are missing per unit cell; (b) linear fit obtained when the number of missing linkers per unit cell is plotted against calculated BET surfaces. The legend in part (a) explains the colour scheme. No. Defects = number of linkers per unit cell. Reprinted with permission from Ref. [140].

2.8.6 FTIR: multiple OH stretching bands

A missing linker defect structure is generated by removing a number of BDC linkers from the pristine UiO-66 framework. The missing negative charge may be compensated for by adding a negative ligand or by removing a positive proton from the node to ensure the neutrality of the node. To preserve the charge neutrality of the MOF structure, for instance, OH functional groups from the modulator or solvent must compensate for the dangling bonds of the positively charged inorganic moieties in the modulation synthesis, making it possible to detect more OH stretching bands. FTIR was utilised to detect the multiple OH stretching bands [160–162] under that presumption. The early study [152] used an in-situ IR technique (Mettler Toledo EasyMaxTM 102 sets reactor together with a ReactIRTM 15 spectrometer) as indicated in Figure 2.20a, to monitor the Zr-fumarate (Zr-fum) MOF crystallisation process in real synthesis conditions. In Fig 2.20b the 3D graph of the FTIR spectrum which was collected over time

demonstrated the consumption of reactants and the formation of Zr-fum MOF in a DMF-based system, showing both modulator (HCOOH) and solvent (DMF) participation in compensating for the missing linker or cluster defects when the structure of the Zr-fum MOF was formed.

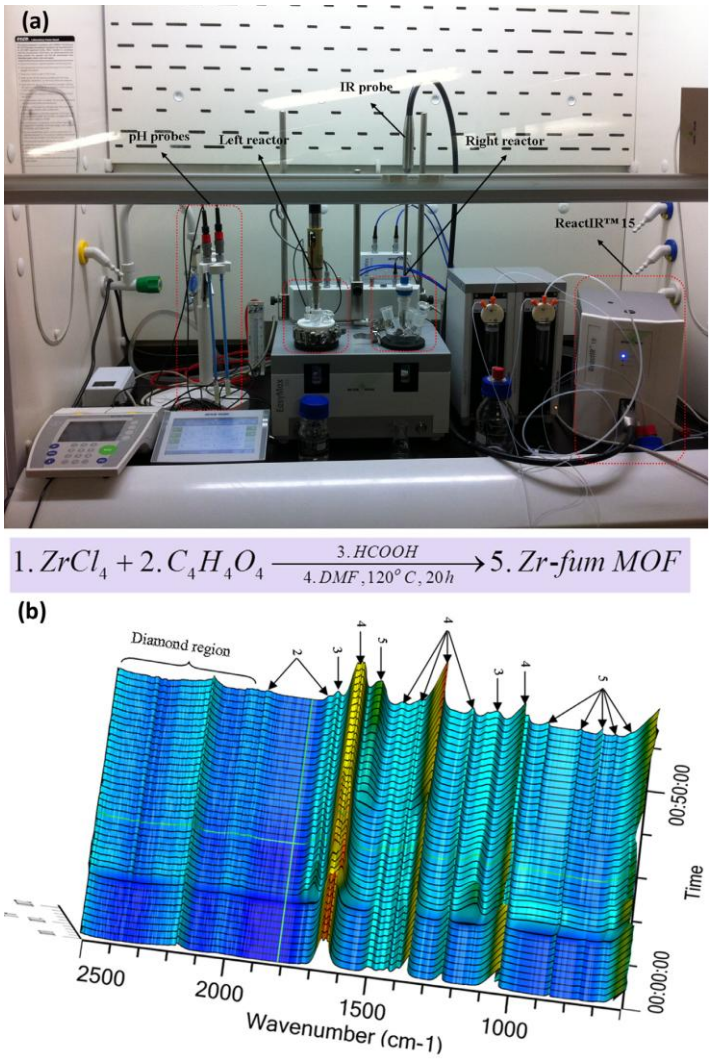

Figure 2.19. (a) In situ IR monitoring system: Mettler Toledo EasyMaxTM 102 sets a 15-spectrometer reactor. (b) 3-dimensional FTIR plot collected over time showing reactant consumption and the formation of the Zr-fum MOF product under DMF-based system. Reprinted with permission from Ref. [152].

2.9 **Conclusion**

The main goal of this dissertation is to develop the knowledge and methods that are needed to engineer, optimize and improve the performance of UiO-66 MOFs for practical applications in hydrogen adsorption. This chapter focuses on establishing the knowledge required to achieve this goal. Knowledge about how MOFs are designed is essential in order to establish how they can be modified/improved. The applicability of MOFs in hydrogen storage also provides insight into how one can optimise the hydrogen that these MOFs can adsorb and store; this includes studying and manipulating the pores. Achieving the DOE standards for hydrogen storage is difficult and only few materials are able to reach this target, and some of the results in this study were able to reach the target of 7 wt% absolute hydrogen adsorption at high pressures. Therefore, for defect-engineering studies we can modify the UiO-66 MOF based on techniques that have been mentioned herein to improve the hydrogen uptake capacities and ultimately achieve the standards set by the DOE for hydrogen storage.

2.10 **References**

1. He, Y., Li, B., O'Keeffe, M. and Chen, B., Multifunctional metal–organic frameworks constructed from meta-benzenedicarboxylate units. *Chem. Soc. Rev*, **2014**, *43*(16), 5618-5656.
2. Hoskins, B.F. and Robson, R., Design and construction of a new class of scaffolding-like materials comprising infinite polymeric frameworks of 3D-linked molecular rods. A reappraisal of the zinc cyanide and cadmium cyanide structures and the synthesis and structure of the diamond-related frameworks [N (CH3) 4][CuIZnII (CN) 4] and CuI [4, 4', 4", 4"'-tetracyanotetraphenylmethane] BF4. xC6H5NO2. *J. Am. Chem. Soc*. **990**, *112*(4), 1546-1554.
3. Abrahams, B.F., Hoskins, B.F. and Robson, R., A honeycomb form of cadmium cyanide. A new type of 3D arrangement of interconnected rods generating infinite linear channels of large hexagonal cross-section. *J. Chem. Soc., Chem. Commun*. **1990** , (1), 60-61.
4. Lee, J., Farha, O.K., Roberts, J., Scheidt, K.A., Nguyen, S.T. and Hupp, J.T., Metal–organic framework materials as catalysts. *Chem. Soc. Rev*. **2009**, .*38*(5), 1450-1459.
5. Corma, A., García, H. and Llabrés i Xamena, F.X., Engineering metal organic frameworks for heterogeneous catalysis. *Chem. Rev*. **2010**, *110*(8), 4606-4655.
6. Yoon, M., Srirambalaji, R. and Kim, K., Homochiral metal–organic frameworks for asymmetric heterogeneous catalysis. *Chem. Rev*., **2011**, *112*(2), 1196-1231.
7. Kreno, L.E., Leong, K., Farha, O.K. and Allendorf, M., RP Van duyne, and JT Hupp. *Chem. Rev*, **2012**, *112*(2), 1105-1125.
8. Hu, Z., Deibert, B.J. and Li, J., Luminescent metal–organic frameworks for chemical sensing and explosive detection. *Chem. Soc. Rev*. **2014**, *43*(16), 5815-5840.

9. Narayan, T.C., Miyakai, T., Seki, S. and Dincă, M., High charge mobility in a tetrathiafulvalene-based microporous metal–organic framework. *J. Am. Chem. Soc.* **2012**, *134*(31), 12932-12935.
10. Sun, L., Miyakai, T., Seki, S. and Dincă, M., Mn2 (2, 5-disulfhydrylbenzene-1, 4-dicarboxylate): A Microporous Metal–Organic Framework with Infinite (− Mn–S−)∞ Chains and High Intrinsic Charge Mobility. *J. Am. Chem. Soc.* **2013**, *135*(22), 8185-8188.
11. Li, Y., Pang, A., Wang, C. and Wei, M., Metal–organic frameworks: promising materials for improving the open circuit voltage of dye-sensitized solar cells. *J. Mater. Chem.* **2011**, *21*(43), 17259-17264.
12. Horcajada, P., Gref, R., Baati, T., Allan, P.K., Maurin, G., Couvreur, P., Ferey, G., Morris, R.E. and Serre, C., Metal–organic frameworks in biomedicine. *Chem. Rev.* **2011**, *112*(2), 1232-1268.
13. Horcajada, P., Chalati, T., Serre, C., Gillet, B., Sebrie, C., Baati, T., Eubank, J.F., Heurtaux, D., Clayette, P., Kreuz, C. and Chang, J.S., Porous metal–organic-framework nanoscale carriers as a potential platform for drug delivery and imaging. *Nat. Mater.* **2010**, 9(2), 172.
14. Della Rocca, J., Liu, D. and Lin, W., Nanoscale metal–organic frameworks for biomedical imaging and drug delivery. *Acc. Chem. Res*, **2011**, *44*(10), 957-968.
15. Zhang, W. and Xiong, R.G., Ferroelectric metal–organic frameworks. *Chem. Rev.* **2011**, *112*(2), 1163-1195.
16. Wang, C., Zhang, T. and Lin, W., Rational synthesis of non-centrosymmetric metal–organic frameworks for second-order nonlinear optics. *Chem. Rev.* **2011**, *112*(2), 1084-1104.
17. Sun, C.Y., Wang, X.L., Zhang, X., Qin, C., Li, P., Su, Z.M., Zhu, D.X., Shan, G.G., Shao, K.Z., Wu, H. and Li, J., Efficient and tunable white-light emission of metal–organic frameworks by iridium-complex encapsulation. *Nat. Commun.* **2013**, *4*, 2717.

18. Stock, N. and Biswas, S., Synthesis of metal-organic frameworks (MOFs): routes to various MOF topologies, morphologies, and composites. *Chem. Rev*. **2011**, *112*(2), 933-969.

19. James, S.L., Metal-organic frameworks. *Chem. Soc. Rev*. **2003**, *32*(5), 276-288.

20. Zaworotko, M.J., Metal–organic materials: a reversible step forward. *Nat. Chem*. **2009**, *1*(4), 267.

21. Kulprathipanja, S., *Zeolites Ind. Sep. Catal.*. Ed.; John Wiley & Sons. 2010

22. Li, J.R., Kuppler, R.J. and Zhou, H.C., Selective gas adsorption and separation in metal–organic frameworks. *Chem. Soc. Rev*., **2009,** *38*(5), 1477-1504.

23. DeCoste, J.B. and Peterson, G.W., Metal–organic frameworks for air purification of toxic chemicals. *Chem. Rev*. **2014**, *114*(11), 5695-5727.

24. He, Y., Zhou, W., Qian, G. and Chen, B., Methane storage in metal–organic frameworks. *Chem. Soc. Rev*., **2014**, *43*(16), 5657-5678.

25. Getman, R.B., Bae, Y.S., Wilmer, C.E. and Snurr, R.Q., Review and analysis of molecular simulations of methane, hydrogen, and acetylene storage in metal–organic frameworks. *Chem. Rev*., **2011**, *112*(2), 703-723.

26. Suh, M.P., Park, H.J., Prasad, T.K. and Lim, D.W., Hydrogen storage in metal–organic frameworks. *Chem. rev*., **2011**, *112*(2), 782-835.

27. Zhang, Z. J.; Zhao, Y. G.; Gong, Q. H.; Li, Z.; Li, J. *Chem. Commun*. **2013**, *49*, 653.

28. Sumida, K., Rogow, D.L., Mason, J.A., McDonald, T.M., Bloch, E.D., Herm, Z.R., Bae, T.H. and Long, J.R., Carbon dioxide capture in metal–organic frameworks. *Chem. Rev*. **2011**, *112*(2), 724-781.

29. Li, J.R., Sculley, J. and Zhou, H.C., Metal–organic frameworks for separations. *Chem. Rev*. **2011**, *112*(2), 869-932.

30. Wu, H., Gong, Q., Olson, D.H. and Li, J., Commensurate adsorption of hydrocarbons and alcohols in microporous metal organic frameworks. *Chem. Rev*. **2012**, *112*(2), 836-868.

31. Furukawa, H., Cordova, K.E., O'Keeffe, M. and Yaghi, O.M., The chemistry and applications of metal-organic frameworks. *Science* **2013**, *341*(6149), 1230444.

32. http://www.bza.org/zeolites.html accessed on 15-05-2015.

33. Sing, K. S. W., Everett, D. H., Haul, R. A. W., Moscou, L., Pierotti, R. A., Rouquerol, J., Siemieniewska, T., *Pure Appl. Chem*. **1985**, 57, 603.

34. Rouquerol, J., Avnir, D., Fairbridge, C. W., Everett, D. H., Haynes, J. H., Pernicone, N., Ramsay, J. D. F., Sing K. S. W., K. K. Unger, *Pure Appl. Chem*. **1994**, 66, 1739.

35. Kitagawa, S., Matsuda, R., *Coord. Chem. Rev*. **2007**, 251, 2490.

36. Rowsell, J. L. C., Yaghi, O. M., *Microporous Mesoporous Mater*. **2004**, 73, 3.

37. Kitagawa S., R. Kitaura, S.I. Noro, *Angew. Chem. Int. Ed*. **2004**, 43, 2334

38. Hoskins, B. F., Robson, R., Design and construction of a new class of scaffolding-like materials comprising infinite polymeric frameworks of 3D-linked molecular rods. A reappraisal of the zinc cyanide and cadmium cyanide structures and the synthesis and structure of the diamond-related frameworks [N (CH3) 4][CuIZnII (CN) 4] and CuI [4, 4', 4", 4"'-tetracyanotetraphenylmethane] BF4. xC6H5NO2. *J. Am. Chem. Soc*. **1990**, 112, 1546.

39. Fujita, M., Kwon, Y. J., Washizu, S., Ogura, K., Preparation, clathration ability, and catalysis of a two-dimensional square network material composed of cadmium (II) and 4, 4'-bipyridine. *J. Am. Chem. Soc*. **1994**, 116, 1151.

40. Yaghi, O. M., Li, G., Li, H., Selective binding and removal of guests in a microporous metal–organic framework. *Nature* **1995**, 378, 703.

41. Venkataraman, D., Gardner, G. B., Lee, S., Moore, J. S., Zeolite-like behavior of a coordination network. *J. Am. Chem. Soc*. **1995**, 117, 11600.

42. Kondo, M., Yoshitomi, T., Seki, K., Matsuzaka, H., Kitagawa, S., Three‐Dimensional Framework with Channeling Cavities for Small Molecules:{[M_2(4,4′-bpy)$_3$(NO_3)$_4$]·xH_2O}$_n$ (M = Co, Ni, Zn). *Angew. Chem. Int. Ed. Engl.* **1997**, 36, 1725.

43. Eddaoudi, H. Li, M., Groy, T. L., Yaghi, O. M., Establishing microporosity in open metal–organic frameworks: gas sorption isotherms for Zn (BDC)(BDC= 1, 4-benzenedicarboxylate). *J. Am. Chem. Soc.* **1998**, *120*, 8571.

44. Li, H., Eddaoudi, M., O'Keeffe, M., Yaghi, O. M., Design and synthesis of an exceptionally stable and highly porous metal-organic framework. *Nature* **1999**, 402, 276.

45. Atwood, J. L., Steed, J. W., Encyclopedia of Supramolecular Chemistry. 2004; Vol. 2.

46. Desiraju, G. R., Crystal Engineering, the Design of Organic Solids. Elsevier: Amsterdam, 1989.

47. Desiraju, G.R., Supramolecular synthons in crystal engineering—a new organic synthesis. Angew. *Chem Int. Ed. Engl.* **1995**, 34, 2311-2327.

48. Cavka, J.H., Jakobsen, S., Olsbye, U., Guillou, N., Lamberti, C., Bordiga, S. and Lillerud, K.P., A new zirconium inorganic building brick forming metal organic frameworks with exceptional stability. *J. Am. Chem. Soc.*, **2008**, 130(42), 13850-13851.

49. Puchberger, M., Kogler, F. R., Jupa, M., Gross, S., Fric, H., Kickelbick, G., and Schubert, U. Eur. J. Inorg. Chem.2006 3283 3293

50. Cairns, A.B. and Goodwin, A.L., Structural disorder in molecular framework materials. *Chem. Soc. Rev.* **2013**, *42*(12), 4881-4893.

51. Foo, M.L., Matsuda, R. and Kitagawa, S., Functional hybrid porous coordination polymers. *Chem. Mater.*, **2013**, *26*(1), 310-322.

52. Burrows, A.D., Mixed-component metal–organic frameworks (MC-MOFs): enhancing functionality through solid solution formation and surface modifications. *CrystEngComm*, **2011**, *13*(11), 3623-3642.

53. Yoshida, Y., Inoue, K. and Kurmoo, M., On the Nature of the Reversibility of Hydration□ Dehydration on the Crystal Structure and magnetism of the Ferrimagnet [MnII (enH)(H_2O)][CrIII ($CN)_6$]· H_2O. *Inorg. Chem.*, **2008**, *48*(1), 267-276.

54. Takamizawa, S. and Kohbara, M.A., Closed-pore crystal capable of adsorbing CO 2 onto isolated cavities generated by disorderly mixing of substituents on host skeleton. *Dalton Trans.* **2007** , (33), 3640-3645.

55. Bennett, T.D. and Cheetham, A.K., Amorphous metal–organic frameworks. *Acc. Chem. Res*, **2014**, *47*(5), 1555-1562.

56. Bürgi, H.B. and Weber, T., Disorder and Motion in Crystal Structures: Nuisance and Opportunities. *CHIMIA International Journal for Chemistry*, **2001**, *55*(6), 510-516.

57. Yang, S., Lin, X., Lewis, W., Suyetin, M., Bichoutskaia, E., Parker, J.E., Tang, C.C., Allan, D.R., Rizkallah, P.J., Hubberstey, P. and Champness, N.R., A partially interpenetrated metal–organic framework for selective hysteretic sorption of carbon dioxide. *Nature Mater.* **2012**, *11*(8), 710.

58. Choi, S.B., Furukawa, H., Nam, H.J., Jung, D.Y., Jhon, Y.H., Walton, A., Book, D., O'Keeffe, M., Yaghi, O.M. and Kim, J., Reversible interpenetration in a metal–organic framework triggered by ligand removal and addition. *Angew. Chem. Int. Ed.*, **2012**, *51*(35), 8791-8795.

59. Sánchez-Andújar, M., Presedo, S., Yáñez-Vilar, S., Castro-García, S., Shamir, J. and Señarís-Rodríguez, M.A., Characterization of the Order− Disorder Dielectric Transition in the Hybrid Organic− Inorganic Perovskite-Like Formate Mn $(HCOO)_3$ [$(CH_3)_2NH_2$]. *Inorg. Chem.*, **2010**, *49*(4), 1510-1516.

60. Fairbank, V.E., Thompson, A.L., Cooper, R.I. and Goodwin, A.L., Charge-ice dynamics in the negative thermal expansion material Cd (CN) 2. *Phys. Rev. B*, **2012**, *86*(10), 104113.
61. Martí-Gastaldo, C., Antypov, D., Warren, J.E., Briggs, M.E., Chater, P.A., Wiper, P.V., Miller, G.J., Khimyak, Y.Z., Darling, G.R., Berry, N.G. and Rosseinsky, M.J., Side-chain control of porosity closure in single-and multiple-peptide-based porous materials by cooperative folding. *Nat. Chem.*, **2014**, *6*(4), 343.
62. Shen, P., He, W.W., Du, D.Y., Jiang, H.L., Li, S.L., Lang, Z.L., Su, Z.M., Fu, Q. and Lan, Y.Q., Solid-state structural transformation doubly triggered by reaction temperature and time in 3D metal-organic frameworks: great enhancement of stability and gas adsorption. *Chem. Sci.* **2014**, *5*(4), 1368-1374.
63. Welberry, T.R., TR Welberry and BD Butler, *Chem. Rev.*, **1995**, *95*, 2369.
64. Fang, Z., Bueken, B., De Vos, D.E. and Fischer, R.A., Defect-engineered metal–organic frameworks. *Angew. Chem. Int. Ed.* **2015**, *54*(25), 7234-7254.
65. Choi, J.S., Son, W.J., Kim, J. and Ahn, W.S., Metal–organic framework MOF-5 prepared by microwave heating: factors to be considered. *Microporous and Mesoporous Mater.*, **2008**, *116*(1-3), 727-731.
66. Walker, A.M., Slater, B., Gale, J.D. and Wright, K., Predicting the structure of screw dislocations in nanoporous materials. *Nat. Mater.* **2004**, *3*(10), 715.
67. Shöâeè, M., Agger, J.R., Anderson, M.W. and Attfield, M.P., Crystal form, defects and growth of the metal organic framework HKUST-1 revealed by atomic force microscopy. *CrystEngComm*, **2008**, *10*(6), 646-648.
68. Carlucci, L., Ciani, G., Moret, M., Proserpio, D.M. and Rizzato, S., Polymeric layers catenated by ribbons of rings in a three-dimensional self-assembled architecture: a nanoporous network with spongelike behavior. *Angew. Chem. Int. Ed.*, **2000**, *39*(8), 1506-1510.

69. Wu, H., Chua, Y.S., Krungleviciute, V., Tyagi, M., Chen, P., Yildirim, T. and Zhou, W., Unusual and highly tunable missing-linker defects in zirconium metal–organic framework UiO-66 and their important effects on gas adsorption. *J. Am. Chem. Soc.*, **2013**, *135*(28), 10525-10532.

70. Ravon, U., Savonnet, M., Aguado, S., Domine, M.E., Janneau, E. and Farrusseng, D., Engineering of coordination polymers for shape selective alkylation of large aromatics and the role of defects. *Microporous and Mesoporous Mater.*, **2010**, *129*(3), 319-329.

71. Vermoortele, F., Vandichel, M., Van de Voorde, B., Ameloot, R., Waroquier, M., Van Speybroeck, V. and De Vos, D.E., 2012. Electronic effects of linker substitution on Lewis acid catalysis with metal–organic frameworks. *Angew. Chem. Int. Ed.*, *51*(20), pp.4887-4890.

72. Shearer, G.C., Chavan, S., Ethiraj, J., Vitillo, J.G., Svelle, S., Olsbye, U., Lamberti, C., Bordiga, S. and Lillerud, K.P., Tuned to perfection: Ironing out the defects in metal–organic framework uio-66. *Chem. Mater.* **2014**, *26*(14), 4068-4071.

73. Cliffe, M.J., Wan, W., Zou, X., Chater, P.A., Kleppe, A.K., Tucker, M.G., Wilhelm, H., Funnell, N.P., Coudert, F.X. and Goodwin, A.L., Correlated defect nanoregions in a metal–organic framework. *Nat. Commun.*, **2014**, *5*, 4176.

74. Fang, Z., Dürholt, J.P., Kauer, M., Zhang, W., Lochenie, C., Jee, B., Albada, B., Metzler-Nolte, N., Pöppl, A., Weber, B. and Muhler, M., Structural complexity in metal–organic frameworks: Simultaneous modification of open metal sites and hierarchical porosity by systematic doping with defective linkers. *J. Am. Chem. Soc.* **2014**, *136*(27), 9627-9636.

75. Park, J., Wang, Z.U., Sun, L.B., Chen, Y.P. and Zhou, H.C., Introduction of functionalized mesopores to metal–organic frameworks via metal–ligand–fragment coassembly. *J. Am. Chem. Soc.* **2012**, *134*(49), 20110-20116.

76. Vermoortele, F., Bueken, B., Le Bars, G., Van de Voorde, B., Vandichel, M., Houthoofd, K., Vimont, A., Daturi, M., Waroquier, M., Van Speybroeck, V. and Kirschhock, C., Synthesis modulation as a tool to increase the catalytic activity of metal–organic frameworks: the unique case of UiO-66 (Zr). *J. Am. Chem. Soc.* **2013**, *135*(31), 11465-11468.

77. St. Petkov, P., Vayssilov, G.N., Liu, J., Shekhah, O., Wang, Y., Wöll, C. and Heine, T., Defects in MOFs: A thorough characterization. *ChemPhysChem*, **2012**, *13*(8), 2025-2029.

78. Kozachuk, O., Luz, I., Llabrés i Xamena, F.X., Noei, H., Kauer, M., Albada, H.B., Bloch, E.D., Marler, B., Wang, Y., Muhler, M. and Fischer, R.A., Multifunktionale, Defekt-manipulierte Metall-organische Gerüste mit Rutheniumzentren: Sorption und katalytische Eigenschaften. *Angew. Chem.*, **2014**, *126*(27), 7178-7182.

79. Vermoortele, F., Ameloot, R., Alaerts, L., Matthessen, R., Carlier, B., Fernandez, E.V.R., Gascon, J., Kapteijn, F. and De Vos, D.E., Tuning the catalytic performance of metal–organic frameworks in fine chemistry by active site engineering. *J. Mater. Chem.*, **2012**, *22*(20), 10313-10321.

80. Marx, S., Kleist, W. and Baiker, A., Synthesis, structural properties, and catalytic behavior of Cu-BTC and mixed-linker Cu-BTC-PyDC in the oxidation of benzene derivatives. *J. Catal*, **2011**, *281*(1), 76-87.

81. Valvekens, P., Jonckheere, D., De Baerdemaeker, T., Kubarev, A.V., Vandichel, M., Hemelsoet, K., Waroquier, M., Van Speybroeck, V., Smolders, E., Depla, D. and Roeffaers, M.B.J., Base catalytic activity of alkaline earth MOFs: a (micro) spectroscopic study of active site formation by the controlled transformation of structural anions. *Chem. Sci.* **2014**, *5*(11), 4517-4524.

82. Valvekens, P., Jonckheere, D., De Baerdemaeker, T., Kubarev, A.V., Vandichel, M., Hemelsoet, K., Waroquier, M., Van Speybroeck, V., Smolders, E., Depla, D. and Roeffaers,

M.B.J., Base catalytic activity of alkaline earth MOFs: a (micro) spectroscopic study of active site formation by the controlled transformation of structural anions. *Chem. Sci.*, **2014**, *5*(11), 4517-4524.

83. Vandichel, M., Hajek, J., Vermoortele, F., Waroquier, M., De Vos, D.E. and Van Speybroeck, V., Active site engineering in UiO-66 type metal–organic frameworks by intentional creation of defects: a theoretical rationalization. *CrystEngComm*, **2015**, *17*(2), 395-406.
84. Bloch, E.D., Queen, W.L., Hudson, M.R., Mason, J.A., Xiao, D.J., Murray, L.J., Flacau, R., Brown, C.M. and Long, J.R., Hydrogen storage and selective, reversible O2 adsorption in a metal–organic framework with open chromium (II) sites. *Angew. Chem. Int. Ed.*, **2016**, *55*(30), 8605-8609.
85. Fei, H., Pullen, S., Wagner, A., Ott, S. and Cohen, S.M., Functionalization of robust Zr (iv)-based metal–organic framework films via a postsynthetic ligand exchange. *Chem. Commun.* **2015**, *51*(1), 66-69.
86. Furukawa, H., Müller, U. and Yaghi, O.M., "Heterogeneity within order" in metal–organic frameworks. *Angew. Chem. Int. Ed.*, **2015**, *54*(11), 3417-3430.
87. modmo
88. McGuire, C.V. and Forgan, R.S., The surface chemistry of metal–organic frameworks. *Chem. Commun.*, **2015**, *51*(25), 5199-5217.
89. Lee, H.J., We, J., Kim, J.O., Kim, D., Cha, W., Lee, E., Sohn, J. and Oh, M., Morphological and structural evolutions of metal–organic framework particles from amorphous spheres to crystalline hexagonal rods. *Angew. Chem. Int. Ed.* **2015**, *54*(36), 10564-10568.
90. Diring, S., Furukawa, S., Takashima, Y., Tsuruoka, T. and Kitagawa, S., Controlled multiscale synthesis of porous coordination polymer in nano/micro regimes. *Chem. Mater.* **2010**, *22*(16), 4531-4538.

91. Tsuruoka, T. and Furukawa, S., Y. T, K. Yoshida, S. Isoda and S. Kitagawa. Nanoporous nanorods fabricated by coordination modulation and oriented attachment growth. *Angew. Chem., Int. Ed*, **2009**, *48*, 4739-4743.

92. T. Tsuruoka, S. Furukawa, Y. Takashima, K. Yoshida, S. Isoda and S. Kitagawa, Nanoporous Nanorods Fabricated by Coordination Modulation and Oriented Attachment Growth. *Angew. Chem*., 2009, 121, 4833

93. S. Diring, S. Furukawa, Y. Takashima, T. Tsuruoka and S. Kitagawa, Controlled Multiscale Synthesis of Porous Coordination Polymer in Nano/Micro Regimes. *Chem. Mater*., 2010, 22, 4531

94. Li, Y.W., Yan, H., Hu, T.L., Ma, H.Y., Li, D.C., Wang, S.N., Yao, Q.X., Dou, J.M., Xu, J. and Bu, X.H., Two microporous Fe-based MOFs with multiple active sites for selective gas adsorption. *Chem. Commun.*, **2017**, *53*(15), 2394-2397.

95. Kim, M., Cahill, J.F., Su, Y., Prather, K.A. and Cohen, S.M., Postsynthetic ligand exchange as a route to functionalization of 'inert' metal–organic frameworks. Chem. Sci., **2012**, 3(1), pp.126-130.

96. Kim, M.; Cahill, J. F.; Fei, H.; Prather, K. A.; Cohen, S. M.Postsynthetic Ligand and Cation Exchange in Robust Metal-OrganicFrameworks.*J. Am. Chem. Soc*., **2012**, 134, 18082−18088

97. Taddei, M.; Wakeham, R. J.; Koutsianos, A.; Andreoli, E.;Barron, A. R. Post-Synthetic Ligand Exchange in Zirconium-BasedMetal-Organic Frameworks: Beware of the Defects!Angew. *Chem., Int.Ed*., **2018**, 57, 11706−11710

98. Marreiros, J., Caratelli, C., Hajek, J., Krajnc, A., Fleury, G., Bueken, B., De Vos, D.E., Mali, G., Roeffaers, M.B., Van Speybroeck, V. and Ameloot, R.,. Active role of methanol in post-synthetic linker exchange in the metal–organic framework UiO-66. *Chem. Mater*., **2019**, 31(4), pp.1359-1369.

99. Yang, D.; Ortuno, M. A.; Bernales, V.; Cramer, C. J.; Gagliardi,L.; Gates, B. C., Structure and Dynamics of Zr6O8 Metal-OrganicFramework Node Surfaces Probed with Ethanol Dehydration as a Catalytic Test Reaction. *J. Am. Chem. Soc.* **2018**, 140, 3751-3759

100. Feng, D., Gu, Z.Y., Li, J.R., Jiang, H.L., Wei, Z. and Zhou, H.C., Zirconium-metalloporphyrin PCN-222: mesoporous metal–organic frameworks with ultrahigh stability as biomimetic catalysts. *Angew. Chem. Int. Ed.*, **2012**, *51*(41), 10307-10310.

101. Ma, J., Tran, L.D. and Matzger, A.J., Toward topology prediction in Zr-based microporous coordination polymers: the role of linker geometry and flexibility. *Cryst. Growth Des.* **2016**, *16*(7), 4148-4153.

102. Hu, Z., Castano, I., Wang, S., Wang, Y., Peng, Y., Qian, Y., Chi, C., Wang, X. and Zhao, D., Modulator effects on the water-based synthesis of Zr/Hf metal–organic frameworks: quantitative relationship studies between modulator, synthetic condition, and performance. *Cryst. Growth Des.* **2016**, *16*(4), 2295-2301.

103. Gutov, O.V., Hevia, M.G., Escudero-Adán, E.C. and Shafir, A., Metal–organic framework (MOF) defects under control: insights into the missing linker sites and their implication in the reactivity of zirconium-based frameworks. *Inorg. Chem.* **2015**, *54*(17), 8396-8400.

104. Cai, G. and Jiang, H.L., A Modulator-Induced Defect-Formation Strategy to Hierarchically Porous Metal–Organic Frameworks with High Stability. *Angew. Chem. Int. Ed.*, **2017**, 56(2), 563-567.

105. Yu, J., Cui, Y., Wu, C.D., Yang, Y., Chen, B. and Qian, G., Two-photon responsive metal–organic framework. *J. Am. Chem. Soc.*, **2015**, *137*(12), 4026-4029.

106. Li, B., Zhu, X., Hu, K., Li, Y., Feng, J., Shi, J. and Gu, J., Defect creation in metal-organic frameworks for rapid and controllable decontamination of roxarsone from aqueous solution. *J. Hazard. Mater.*, **2016**, *302*, 57-64.

107. O'Keeffe, M., Peskov, M.A., Ramsden, S.J. and Yaghi, O.M., The reticular chemistry structure resource (RCSR) database of, and symbols for, crystal nets. *Acc. Chem. Res*, **2008**, *41*(12), pp.1782-1789.

108. Bristow, J.K., Svane, K.L., Tiana, D., Skelton, J.M., Gale, J.D. and Walsh, A.,. Free Energy of Ligand Removal in the Metal–Organic Framework UiO-66. J. Phys. Chem. C, **2016**, 120(17), pp.9276-9281.

109. Tu, B., Pang, Q., Wu, D., Song, Y., Weng, L. and Li, Q., Ordered vacancies and their chemistry in metal–organic frameworks. *J. Am. Chem. Soc.*, **2014**, *136*(41), 14465-14471.

110. Shekhah, O., Liu, J., Fischer, R.A. and Wöll, C., MOF thin films: existing and future applications. *Chem. Soc. Rev.*, **2011**, *40*(2), 1081-1106.

111. Kind, M. and Wöll, C., Organic surfaces exposed by self-assembled organothiol monolayers: Preparation, characterization, and application. *Prog. Surf. Sci.*, **2009**, *84*(7-8), 230-278.

112. Dissegna, S., Epp, K., Heinz, W.R., Kieslich, G. and Fischer, R.A., Defective Metal-Organic Frameworks. *Adv. Mater.*, **2018**, *30*(37), 1704501.

113. Kozachuk, O., Luz, I., Llabres i Xamena, F.X., Noei, H., Kauer, M., Albada, H.B., Bloch, E.D., Marler, B., Wang, Y., Muhler, M. and Fischer, R.A., Multifunctional, defect-engineered metal–organic frameworks with ruthenium centres: sorption and catalytic properties. *Angew. Chem. Int. Ed.*, **2014**, *53*(27), 7058-7062.

114. Llabrés i Xamena, F.X., García Cirujano, F. and Corma Canós, A., An unexpected bifunctional acid base catalysis in IRMOF-3 for Knoevenagel condensation reactions. *Microporous and Mesoporous Mater.* **2012**, *157*, 112-117.

115. Nguyen, H.G.T., Weston, M.H., Farha, O.K., Hupp, J.T. and Nguyen, S.T., A catalytically active vanadyl (catecholate)-decorated metal organic framework via post-synthesis modifications. *CrystEngComm*, **2012**, *14*(12), 4115-4118.

116. Tanabe, K.K. and Cohen, S.M., Postsynthetic modification of metal–organic frameworks—a progress report. *Chem. Soc. Rev.*, **2011**, *40*(2), 498-519.

117. Wang, Z., Sezen, H., Liu, J., Yang, C., Roggenbuck, S.E., Peikert, K., Fröba, M., Mavrandonakis, A., Supronowicz, B., Heine, T. and Gliemann, H., Tunable coordinative defects in UHM-3 surface-mounted MOFs for gas adsorption and separation: A combined experimental and theoretical study. *Microporous and Mesoporous Mater.*, **2015**, *207*, 53-60.

118. Wang, L. and Yang, R.T., Hydrogen storage on carbon-based adsorbents and storage at ambient temperature by hydrogen spillover. *Catal. Rev.*, **2010**, *52*(4), 411-461.

119. Chen, H., Wang, L., Yang, J. and Yang, R.T., Investigation on hydrogenation of metal–organic frameworks HKUST-1, MIL-53, and ZIF-8 by hydrogen spillover. *J. Phys. Chem. C*, **2013**, *117*(15), 7565-7576.

120. Wang, C.Y., Tsao, C.S., Yu, M.S., Liao, P.Y., Chung, T.Y., Wu, H.C., Miller, M.A. and Tzeng, Y.R., Hydrogen storage measurement, synthesis and characterization of metal–organic frameworks via bridged spillover. *J. Alloys Compd.* **2010**, *492*(1-2), 88-94.

121. Yang, S.J., Cho, J.H., Nahm, K.S. and Park, C.R., Enhanced hydrogen storage capacity of Pt-loaded CNT@ MOF-5 hybrid composites. *Int. J. Hydrogen Energy*, **2010**, *35*(23), 13062-13067.

122. Li, Y. and Yang, R.T., Significantly enhanced hydrogen storage in metal– organic frameworks via spillover. *J. Am. Chem. Soc.* **2006**, *128*(3), 726-727.

123. Li, Q. and Lueking, A.D., Effect of surface oxygen groups and water on hydrogen spillover in Pt-doped activated carbon. *J. Phys. Chem. C*, **2011**, *115*(10), 4273-4282.

124. Lin, K.S., Adhikari, A.K., Chang, K.C., Tu, M.T. and Lu, W., Hydrogen adsorption in metal organic frameworks by hydrogen spillover. *Catal. Today*, **2011**, *164*(1), 23-27.

125. Anbia, M. and Mandegarzad, S., Enhanced hydrogen sorption on modified MIL-101 with Pt/CMK-3 by hydrogen spillover effect. *J. Alloys Compd*, **2012**, *532*, 61-67.

126. Li, B., Huang, X., Gong, R., Ma, M., Yang, X., Liang, L. and Tan, B., Catalyzed hydrogen spillover for hydrogen storage on microporous organic polymers. *Int. J. Hydrogen Energy*, **2012**, *37*(17), 12813-12820.

127. Wang, L., Stuckert, N.R., Chen, H. and Yang, R.T., Effects of Pt particle size on hydrogen storage on Pt-doped metal− organic framework IRMOF-8. *J. Phys. Chem. C*, **2011**, 115(11), 4793-4799.

128. Pullen, S., Fei, H., Orthaber, A., Cohen, S.M. and Ott, S., Enhanced photochemical hydrogen production by a molecular diiron catalyst incorporated into a metal–organic framework. *J. Am. Chem. Soc.* **2013**, *135*(45), 16997-17003.

129. Fei, H. and Cohen, S.M., Metalation of a thiocatechol-functionalized Zr (IV)-based metal–organic framework for selective C–H functionalization. *J. Am. Chem. Soc.*, **2015**, *137*(6), 2191-2194.

130. Fei, H., Shin, J., Meng, Y.S., Adelhardt, M., Sutter, J., Meyer, K. and Cohen, S.M., Reusable oxidation catalysis using metal-monocatecholato species in a robust metal–organic framework. *J. Am Chem. Soc.*, **2014**, *136*(13), 4965-4973.

131. Taddei, M., When defects turn into virtues: The curious case of zirconium-based metal-organic frameworks. *Coord. Chem. Rev.*, **2017**, *343*, 1-24.

132. Kandiah, M., Nilsen, M.H., Usseglio, S., Jakobsen, S., Olsbye, U., Tilset, M., Larabi, C., Quadrelli, E.A., Bonino, F. and Lillerud, K.P., Synthesis and stability of tagged UiO-66 Zr-MOFs. *Chem. Mater.*, **2010**, *22*(24), 6632-6640.

133. Jakobsen, S., Gianolio, D., Wragg, D.S., Nilsen, M.H., Emerich, H., Bordiga, S., Lamberti, C., Olsbye, U., Tilset, M. and Lillerud, K.P., Structural determination of a highly stable metal-organic framework with possible application to interim radioactive waste scavenging: Hf-UiO-66. *Phys. Rev. B*, **2012**, *86*(12), 125429.

134. Øien, S., Wragg, D., Reinsch, H., Svelle, S., Bordiga, S., Lamberti, C. and Lillerud, K.P., Detailed structure analysis of atomic positions and defects in zirconium metal–organic frameworks. *Cryst. Growth Des.* **2014**, *14*(11), 5370-5372.

135. Song, Y., Thirion, D., Subramanian, S., Lah, M.S. and Yavuz, C.T., Monitoring instability of linear amine impregnated UiO-66 by *in situ* temperature resolved powder X-ray diffraction. *Microporous and Mesoporous Mater.* **2017**, *243*, 85-90.

136. Sears, V.F., Neutron scattering lengths and cross sections. *Neutron News*, **1992**, *3*(3), 26-37.

137. Szilágyi, P.Á., Serra-Crespo, P., Gascon, J., Geerlings, H. and Dam, B., The impact of Post-synthetic linker Functionalization of MOFs on Methane storage: The role of Defects. *Frontiers Energy Res.* **2016**, *4*, 9.

138. Karabacak, M., Cinar, M., Unal, Z., and Kurt, M. FT-IR, UV spectroscopic and DFT quantum chemical study on the molecular conformation, vibrational and electronic transitions of 2-aminoterephthalic acid. *J. Mol. Struct.* **2010**, 982, 22–27.

139. Liang, Q., Zhang, M., Zhang, Z., Liu, C., Xu, S. and Li, Z., Zinc phthalocyanine coupled with UIO-66 (NH_2) via a facile condensation process for enhanced visible-light-driven photocatalysis. *J. Alloys Compd.*, **2017**, 690, 123-130.

140. Kozachuk, O., Meilikhov, M., Yusenko, K., Schneemann, A., Jee, B., Kuttatheyil, A.V., Bertmer, M., Sternemann, C., Pöppl, A. and Fischer, R.A., A Solid-Solution Approach to Mixed-Metal Metal–Organic Frameworks–Detailed Characterization of Local Structures, Defects and Breathing Behaviour of Al/V Frameworks. *Eur.J. Inorg. Chem.*, **2013**, 2013(26), 4546-4557.

141. Nikseresht, A., Daniyali, A., Ali-Mohammadi, M., Afzalinia, A. and Mirzaie, A., Ultrasound-assisted biodiesel production by a novel composite of Fe (III)-based MOF and phosphotangestic acid as efficient and reusable catalyst. *Ultrason. Sonochem*. **2017**, *37*, 203-207.

142. Wu, H., Yildirim, T. and Zhou, W., Exceptional mechanical stability of highly porous zirconium metal–organic framework UiO-66 and its important implications. *J. Phys. Chem. Lett*. **2013**, *4*(6), 925-930.

143. Ren, J., Langmi, H.W., Musyoka, N.M., Mathe, M., Kang, X. and Liao, S., Tuning defects to facilitate hydrogen storage in core-shell MIL-101 (Cr)@ UiO-66 (Zr) nanocrystals. *Mater. Today: Proc.*, **2015**, *2*(7), 3964-3972.

144. Azarifar, D., Ghorbani-Vaghei, R., Daliran, S. and Oveisi, A.R., A Multifunctional Zirconium-Based Metal–Organic Framework for the One-Pot Tandem Photooxidative Passerini Three-Component Reaction of Alcohols. *ChemCatChem*, **2017**, *9*(11), 1992-2000.

145. Yang, Q., Wiersum, A.D., Jobic, H., Guillerm, V., Serre, C., Llewellyn, P.L. and Maurin, G., Understanding the thermodynamic and kinetic behavior of the CO2/CH4 gas mixture within the porous zirconium terephthalate UiO-66 (Zr): a joint experimental and modelling approach. *J. Phys. Chem. C*, **2011**, *115*(28), 13768-13774.

146. Rodríguez-Albelo, L.M., López-Maya, E., Hamad, S., Ruiz-Salvador, A.R., Calero, S. and Navarro, J.A., Selective sulfur dioxide adsorption on crystal defect sites on an isoreticular metal organic framework series. *Nat. Commun.*, **2017**, 8, 14457.

147. Psofogiannakis, G.M. and Froudakis, G.E., Theoretical explanation of hydrogen spillover in metal− organic frameworks. *J. Phys. Chem. C*, **2011**, *115*(10), 4047-4053.

148. Barin, G., Krungleviciute, V., Gutov, O., Hupp, J.T., Yildirim, T. and Farha, O.K., Defect Creation by Linker Fragmentation in Metal–Organic Frameworks and Its Effects on Gas Uptake Properties. *Inorg. Chem.*, **2014**, *53*(13), 6914-6919.

149. Xydias, P., Spanopoulos, I., Klontzas, E., Froudakis, G.E. and Trikalitis, P.N., Drastic enhancement of the CO2 adsorption properties in sulfone-functionalized Zr-and Hf-UiO-67 MOFs with hierarchical mesopores. *Inorg. Chem.* **2013**, *53*(2), 679-681.

150. Shearer, G.C., Forselv, S., Chavan, S., Bordiga, S., Mathisen, K., Bjørgen, M., Svelle, S. and Lillerud, K.P., *In situ* infrared spectroscopic and gravimetric characterisation of the solvent removal and dehydroxylation of the metal organic frameworks UiO-66 and UiO-67. *Top. Catal.* **2013**, *56*(9-10), 770-782.

151. Cmarik, G.E., Kim, M., Cohen, S.M. and Walton, K.S., Tuning the adsorption properties of UiO-66 via ligand functionalization. *Langmuir*, **2012**, *28*(44), 15606-15613.

152. Ren, J., Musyoka, N.M., Langmi, H.W., North, B.C., Mathe, M., Pang, W., Wang, M. and Walker, J., *In situ* IR monitoring of the formation of Zr-fumarate MOF. *Appl. Surf. Sci.*, **2017**, 404, 263-267.

153. Yang, J., Ma, Z., Gao, W. and Wei, M., Layered Structural Co-Based MOF with Conductive Network Frames as a New Supercapacitor Electrode. *Chem. Eur. J*, **2017**, *23*(3), 631-636.

154. Mounfield III, W.P., Tumuluri, U., Jiao, Y., Li, M., Dai, S., Wu, Z. and Walton, K.S., Role of defects and metal coordination on adsorption of acid gases in MOFs and metal

oxides: an *in situ* IR spectroscopic study. *Microporous and Mesoporous Mater.*, **2016**, *227*, 65-75.

155. Jayachandrababu, K.C., Verploegh, R.J., Leisen, J., Nieuwendaal, R.C., Sholl, D.S. and Nair, S., Structure elucidation of mixed-linker zeolitic imidazolate frameworks by solid-state 1H CRAMPS NMR spectroscopy and computational modelling. *J. Am. Chem. Soc.*, **2016**, *138*(23), 7325-7336.

156. Xu, Y., Howarth, A.J., Islamoglu, T., Da Silva, C.T., Hupp, J.T. and Farha, O.K., Combining solvent-assisted linker exchange and transmetallation strategies to obtain a new non-catenated nickel (II) pillared-paddlewheel MOF. *Inorg. Chem. Commun.*, **2016**, *67*, 60-63.

157. Stephenson, C.J., Hupp, J.T. and Farha, O.K., Post-assembly Transformation of a Catalytically Active Composite Material, Pt@ ZIF-8, via Solvent-Assisted Linker Exchange. *Inorg. Chem.* **2016**, *55*(4), 1361-1363.

158. Deng, H., Doonan, C.J., Furukawa, H., Ferreira, R.B., Towne, J., Knobler, C.B., Wang, B. and Yaghi, O.M., Multiple functional groups of varying ratios in metal-organic frameworks. *Science*, **2010**, *327*(5967), 846-850.

159. Burrows, A.D., Frost, C.G., Mahon, M.F. and Richardson, C., Sulfur-tagged metal–organic frameworks and their post-synthetic oxidation. *Chem. Commun.*, **2009** , (28), 4218-4220.

160. Burrows, A.D., Frost, C.G., Mahon, M.F. and Richardson, C., Post-Synthetic Modification of Tagged Metal–Organic Frameworks. *Angew. Chem. Int. Ed.*, **2008**, *47*(44), 8482-8486.

CHAPTER 3: INSTRUMENTATION

3.1 Scanning Electron Microscopy (SEM)

SEM images were recorded at an accelerated voltage of 3 kV using a Carl Zeiss Auriga Cobra focused-ion beam scanning electron microscope (FIBSEM). Before imaging, the samples were mounted on carbon-adhesive tape specimen stubs and then sputter-coated with chromium under vacuum using a Quorum sputter coater to prevent electrostatic charging effects with. The high-energy electron beam may also be detrimental to some materials. Therefore, other methods of characterisation should be used to confirm the results of this technique. The SEM was used in this research to study the morphological appearance of the specimens. Such data have also been used to support studies of gas adsorption.

3.2 Powder X-ray diffraction (PXRD)

This technique is important to assess the crystallinity and structure of the material. Two different instruments were used, one based at Stellenbosch University and the other at the CSIR.

- A benchtop Bruker D2 PHASER was used for routine powder PXRD data collection. It is equipped with a Lynxeye 1D detector and uses Ni-filtered Cu α radiation λ= 1,5418 Å. The generator power was set at 30 kV and 10 mA, and the X-ray beam was limited by a 1.0 mm divergence slit and a 2.5 mm Söller collimator). When necessary, samples were crushed into a powder (with a mortar and pestle) and loaded onto zero-background sample holders.
- PXRD patterns were recorded at ambient conditions on a PANalytical X'Pert Pro powder diffractometer fitted with a pixel detector using Ni-filtered Cu α radiation 1.5418 Å between $3\,^\circ \leq 2\theta \geq 40\,^\circ$ at a scanning speed of $2\,^\circ\,min^{-1}$. For the preparation

of the sample before each measurement, the samples were crushed into a fine powder using a mortar and pestle.

3.3 Thermogravimetric analysis (TGA)

When choosing a porous material suitable for high temperature applications, its thermal stability is essential. Thermograms were recorded on a Mettler Toledo, TGA/SDTA 851e device; approximately 10 mg of sample was loaded onto the platinum pan and heated to 1000 ° C at a heating rate of 10°C.min^{-1} in controlled N_2 atmosphere.

3.4 Differential scanning calorimetry (DSC)

DSC provides information about the physical and chemical changes of a component as a function of temperature. Thermal events are observed as endothermic or exothermic peaks. For differential scanning calorimetry, a TA Instruments Q100 with Liquid Nitrogen Cooling System (LNCS) was used. DSC calculates the flow of power in and out of the sample as a function of time or temperature in a controlled atmosphere (typically N_2 with a flow rate of 50 ml/min) compared to a reference (empty pan equivalent to the sample pan). In a standard TA Instruments aluminium pan, a sample of 1–10 mg was placed and either analysed as an open pan or covered with an aluminium lid, crimped with a pin hole pricked in the lid. The reference pan protocol is the same as that for the sample pan. The sample was then heated and cooled at a rate of 10°C.min^{-1}. The data were exported using the software Universal Analysis 2000 v 4.5A software (TA Instruments) while figures were prepared using OriginPro.

3.5 BET surface area and pore size determination

Using the classical technique of adsorption of N_2 gas, the surface area and porosities of the prepared MOF materials were determined. The principle of BET functions as the foundation for an effective technique for the calculation of the precise surface area of materials and is

commonly employed for this purpose. The model is aimed at explaining the physisorption of gas molecules on a porous solid surface as an extension of the Langmuir theory based on a single layer of gas sorption on solid materials. The BET concept relates to multilayer adsorption of gas which does not react with the adsorbent chemically and measures the specific surface area of the adsorbent. Nitrogen gas (N_2) is widely used as the adsorbent for the determination of standard surface area and pore data at 77 K. The BET isotherm explains the multilayer sorption of gases under high pressure and low temperature conditions as per the equation:

$$\frac{P}{V_{total}(P-P_0)} = \frac{1}{V_{mono}(C)} + \frac{C-1}{V_{mono}(C)}\left(\frac{P}{P_0}\right) \qquad (4.1)$$

Where:

- V_{mono} is the adsorbed volume of gas at high pressure
- P and P_0 are the equilibrium and saturation pressures, respectively.
- C is the BET constant, and
- V_{total} is adsorbed volume of gas at high pressure to permit a gaseous adsorbate monolayer to be applied to the adsorbent.

Surface area and pore size distribution measurements were conducted on an ASAP 2020 HD analyzer (Micromeritics) and the P/P_0 range was chosen to be 0.05–0.3 for BET determination. All gas sorption isotherms are produced using ultra-high purity nitrogen gas (99.999%). The samples that were analysed were outgassed at a temperature sufficient to remove all the solvent molecules without compromising the structure of the MOF. For UiO-66 MOF a degas temperature of 150 °C was used. All MOF samples were outgassed to a pressure of less than 10^{-5} mbar. Both BET and Langmuir approaches were employed to assess the surface area. Pore volumes were measured using the Horvath-Kawazoe (H-K) method [2]. The techniques used are implemented by the ASAP 2020 program.

To measure the surface area and porosity using the ASAP 2020, it was important to determine the density of each sample. For this reason, the AccuPyc II 1340 Micromeritics Pycnometer was used with helium as an analysis gas.

3.6 **Hydrogen adsorption measurements**

Hydrogen adsorption was performed on the Micromeritics ASAP 2020 HD analyzer at 77 K following a volumetric process with a liquid nitrogen dewar used to sustain a constant temperature. The analysis was accomplished from maximum vacuum up to 1 bar.

3.7 **Mechanical studies**

For post-synthetic modification of the material using the mechanical approach, a FTS-1000 shaker mill was used. By combining impact and frictional forces, the FTS-1000 is able to grinds samples. The grinding jars oscillate back and forth by approximately 25 mm at a rate of up to 1800 rpm (30 Hz). This allows the grinding balls to move within the jar, resulting in high-energy collisions between each other and the internal walls of the jar. The specimen is caught and pulverized between these layers. Besides the high impact forces, frictional forces also lead to grinding and mixing. We note that by varying the number of grinding balls utilised, it is possible to change the ratio of impact to frictional force. A single large grinding ball was used for high impact strength and low friction and several small grinding balls for elevated frictional force.

Figure 3.1. A photograph of the shaker mill used for mechanical studies.

3.8 **Hydrogen adsorption at high pressure**

The hydrogen adsorption capacity of Zr-MOF was determined by gravimetric analysis using a Hiden XEMIS Intelligent Gravimetric Analyser, using 99.9999 % hydrogen filtered by a molecular sieve. Prior to the analysis, the MOF specimen were dried in an oven at 80 °C for 24 hours, then placed in the analysis chamber and degassed at 200 °C for 4–6 hours at 10^{-10} bar. Measurements of hydrogen uptake were performed over a pressure range of 0-1 and 100 bar at 77 (in a liquid nitrogen bath) and 298 K.

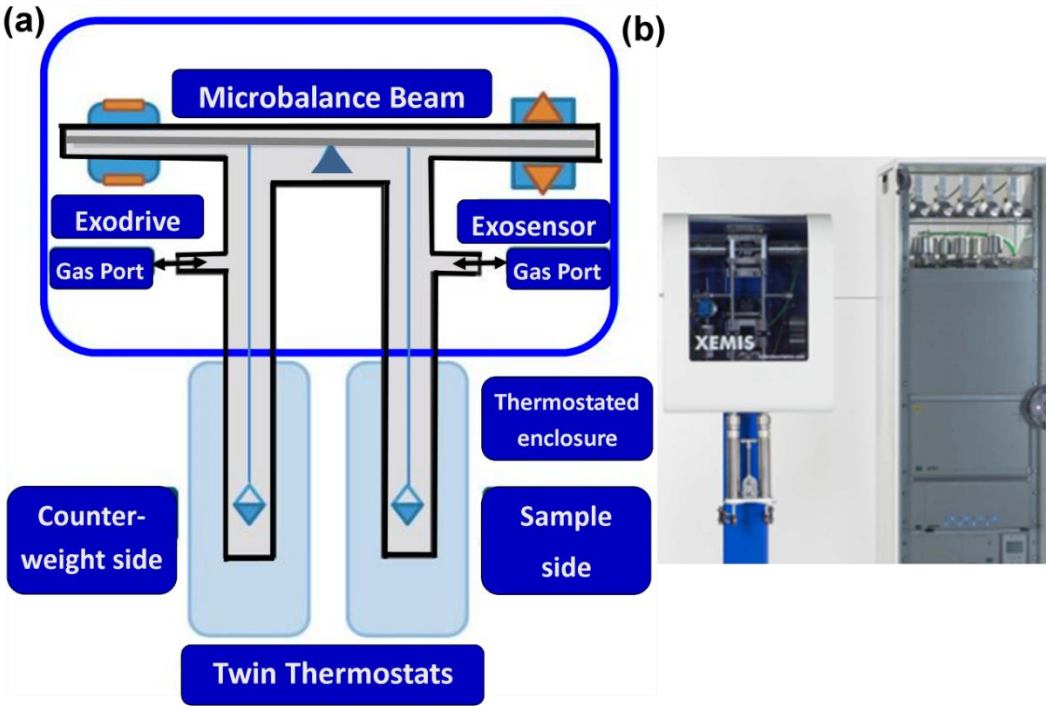

Figure 3.2. (a) Schematic illustration and (b) a photograph of the Hiden Xemis instrument used for high pressure H_2 uptake.

3.9 Fourier-transform infrared spectroscopy (FT-IR)

Fourier transform infrared spectra were generated at room temperature in attenuated total reflection (ATR) mode using a Thermo Scientific Nicolet iS10 (Smart iTR) spectrometer equipped with a diamond-based ATR accessory. The ATR-FTIR spectra were obtained in the range of 4000 and 500 cm^{-1} with a spectral resolution of 4 cm^{-1}. A background spectrum was acquired before each sample was loaded to account for atmospheric changes.

3.10 **Potentiometric acid-base titrations**

Potentiometric acid-base titrations were conducted using a Potentiometric AT-710 M auto titrator. Calibrations were carried out with pH 2.00 and 9.00 buffer solutions before each titration. Sample preparation required the use of a minimum of 40 mg of sample previously activated for 12 hours at 100 °C in a vacuum oven. The samples were ground into a fine powder with a mortar and a pestle prior to analysis. An equivalent amount of 0.01 $NaNO_3$ solution (50 mL for every 50 mg sample) was added and the solution was equilibrated for 2 hours. A stirrer bar was added to the beaker prior to each titration and the pH value was adjusted to 3.00 with 0.1 M HCl. The mixture was then titrated with a 0.1 M NaOH solution at a pH value of 10.50 with an injection volume of 0.02 mL at a rate of 0.02 mL/m^{-1}. In order to accurately represent the equivalence points, the first derivative of the titration curve (pH vs volume of 0.1 M NaOH Added) was used (dpH/dV vs volume of 0.1 M NaOH added). The associated pK_a values were established by the identification of the equivalence volumes on the first derivative plots (inflection points on pH vs pH vs volume of 0.1 M NaOH added) by taking the pH at one half of the titrant volume of NaOH used to reach the equivalence point.

3.11 **References**

1. Gil, A., Diaz, A., Montes, M. and Acosta, D.R., Characterization of the microporosity of pillared clays by nitrogen adsorption—application of the Horvath-Kawazoe approach. *J. Mater. Sci.* **1994**, 29(18), 4927-4932.

CHAPTER 4: SYNTHESIS OF NON-DEFECTIVE UIO-66 MOF

4.1 Abstract

Several synthetic processes have been presented for UiO-66, with a number of groups using their own approaches in preference of using one of the pre-existing procedures. Except for the two most recent reports in which the effects of HCl and acetic acid have been explored, there is a general lack of understanding of how the product is influenced by modifications in the synthetic parameters. The use of HCl acts as modulator in the synthesis in the synthesis of UiO-66 facilitating the decomposition of dimethylformamide into dimethylammonium and $HCOO^-$ at high temperatures.

The aim of this chapter is to elucidate the connection between some of the significant synthetic parameters and the physicochemical characteristics of the product and to discover a technique that provides a "non-defective" sample.

Two characteristics of this procedure stand out: (1) the use of 493 K as the temperature of synthesis and (2) an excess of H_2BDC so that the solution H_2BDC:Zr molar ratio is 2:1. This deviates from most other synthetic procedures in which the synthesis temperature is typically limited to 363−393 K and H_2BDC is added to the synthesis mixture in a 1:1 stoichiometric ratio with Zr. In addition, the impact of processes for DMF washing and methanol return was evaluated [1].

4.2 Synthesis

4.2.1 Reagents and chemicals

Zirconium tetrachloride ($ZrCl_4$, Sigma–Aldrich, 99.5+ %), terephthalic acid (H_2BDC, Sigma–Aldrich, 98%), Hydrochloric acid (HCl, Sigma–Aldrich, 35%), N,N-dimethylformamide (DMF, Sigma–Aldrich, 99.8%), and methanol (MeOH, Sigma–Aldrich, 99+ %) were purchased and used without additional purification.

4.2.2 Procedure

The non-defective UiO-66 sample was synthesised based on a previously reported method with minor changes [1]. The crude UiO-66 samples were synthesised by adding sequentially 3.78 g $ZrCl_4$ (16.2 mmol), 2.86 ml 35% HCl (32.4 mmol), and 5.38 g H_2BDC (32.4 mmol) to a conical flask of 250 ml comprising 97.4 ml N,N'-dimethyl formamide (DMF, 1260 mmol). The mixtures were stirred until the solutions were completely transparent before being transferred into Teflon liners of 200 mL and sealed in autoclaves of stainless steel where they were heated for 20 hours at 493 K. The resulting microcrystalline powders were centrifuged and washed with 60 mL fresh DMF in which they were stirred throughout the night at approximately 70 °C. The following day, although for a short duration (approx. 2 hours each time), three more DMF washings were performed at room temperature. The washed products were recovered by centrifugation and dried overnight in an oven set at 60 °C. A further "activation" method for removing DMF and remaining modulator molecules from pores was applied to the product. This was accomplished by placing the samples in crucibles of alumina and heating them in an oven for 24 hours at 200 °C. The activated UiO-66 samples are not totally void as they re-adsorb atmospheric water vapour when cooled to ambient temperature.

4.3 Results

4.3.1 SEM, TEM and EDS results

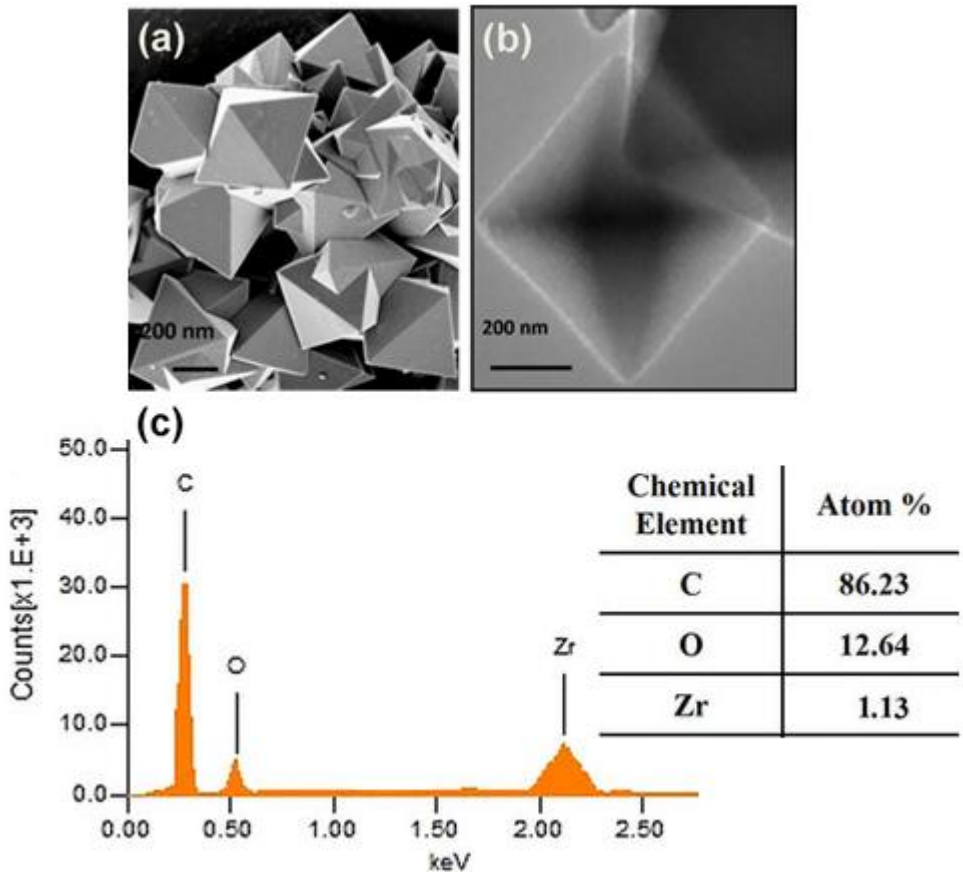

Chemical Element	Atom %
C	86.23
O	12.64
Zr	1.13

Figure 4.1. (a) SEM image, (b) TEM image and (c) EDS spectrum of the synthesised pristine UiO-66 MOF.

The UiO-66 nanocrystals are well-defined with an octahedral morphology with sharp edges and an average size of 600 nm. The non-defective UiO-66 MOF surface is smooth and even. It should be noted that a consistent crystalline structure of UiO-66 is hard to produce especially with DMF as a solvent. In literature, UiO-66 SEM images showed morphologies composed of irregular microcrystallites [2]. According to Figure 4.1a, a characteristic UiO-66 sample synthesised at the specified conditions produced individual nanocrystals in octahedral form. The TEM image shown in Figure 4.1b report that the sizes are consistent with those acquired for SEM. Uniformity is also observed. This confirmed the effective preparation of UiO-66(Zr). It can therefore be asserted that HCl favors the formation of well-defined crystalline UiO-66

MOFs. The EDS spectrum, Figure 4.1c confirms that the elements Zr, C, and O are present in the framework. The results show an average atomic zirconium content of 40% in the resulting elemental mapping of the quantitative analyses.

4.3.2 TGA and DSC results

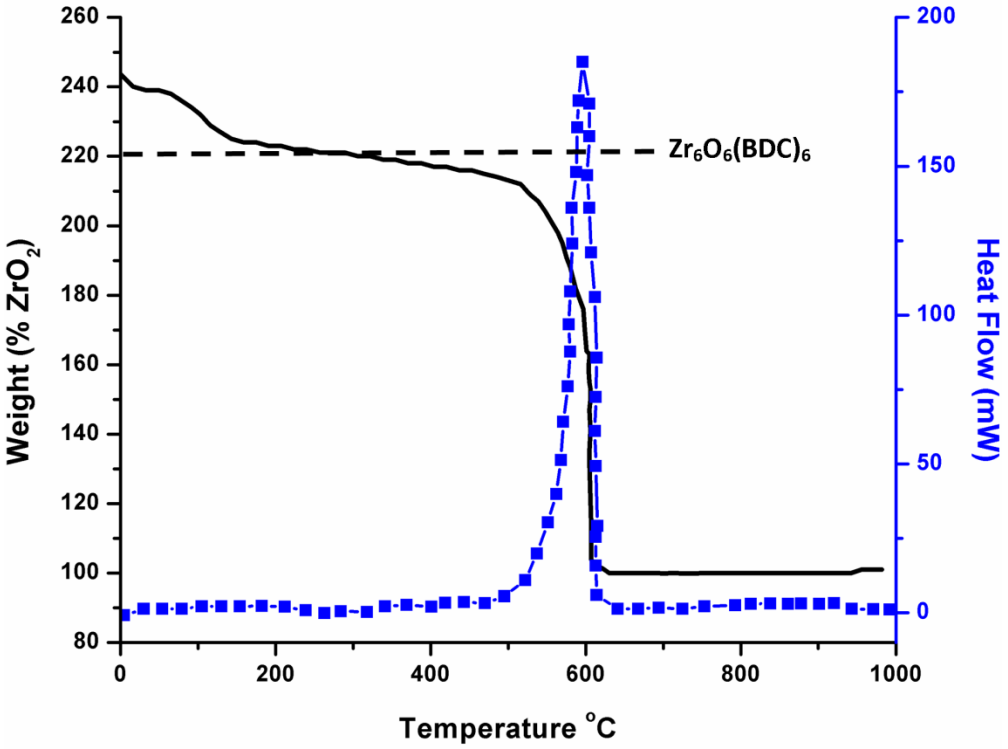

Figure 4.2. TGA-DSC results obtained for the HCl synthesised pristine UiO-66 MOFs. The sample was activated at 473 K before analysis.

The quantitative interpretation of TGA data from UiO-66 MOFs was conducted with the essential assumption that the residue is pure ZrO_2 in all the TGA experiments. In this case, TGA measurements were carried out in an oxygen mixture (synthetic air), with a moderately slow temperature ramp (5 °C/min) up to 1000 °C. In order to confirm this assumption, the environment ensures full combustion of organic matter and conversion to zirconium (IV) oxide.

Considering the chemical equation $Zr_6O_6(bdc)_6$ for aerobic decomposition of UiO-66 (dehydroxylated) , if the end weight of a TGA analysis on UiO-66 is normalised to 100%, the TGA plateau (of a vacant, solvent-free and dehydroxylated MOF) must optimally be observed at 220.2% on the TGA curve. The experimental result reported for the non-defective MOF corresponds to this theoretical weight, meaning that the UiO-66 structure synthesised herein is defect-free. This observation verifies that the UiO-66 framework is not linker/cluster deficient. The TGA traces in Figure 4.2 show three well-resolved weight losses. These losses are allocated to firstly, the volatilisation of adsorbate (in this case H_2O, which may have filled the pores of the framework) and loss of solvent. This occurs within an approximate temperature range of 25 –100°C or the boiling point of the solvent, which is 426 K for DMF. Secondly, the removal of monocarboxylates ligands [3] (in this case terephthalic acid) and the dehydroxylation of Zr_6 nodes [4-7]. These two weight loss events are present in the same temperature range of between 473–623 K. The loss of monocarboxylate is characterised by a small exothermic DSC peak, and lastly, the decomposition of the framework [2, 3, 5]. This occurs over a temperature range of approx. 663−798 K, together with a very dominant exothermic DSC peak, as shown.

4.3.3 PXRD patterns

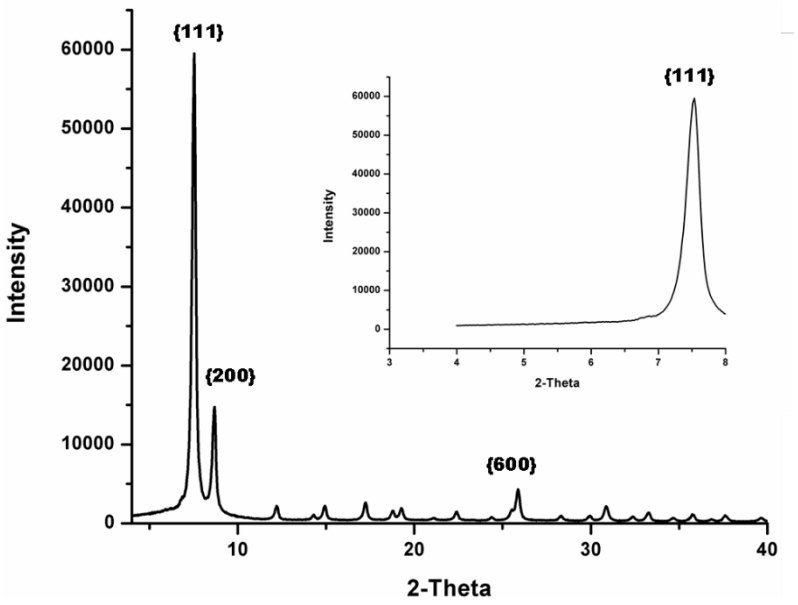

Figure 4.3. PXRD spectra of a non-defective UiO-66 MOF sample.

To verify the synthesis of the non-defective UiO-66 MOF and to measure the phase of the synthesised material, PXRD analysis was carried out. Figure 4.3 shows the diffraction pattern for the synthesised sample and reveals that the material is inherently crystalline. Patterns suggest that the UiO-66 MOF was successfully synthesised with the same topological structure as in the literature [8]. This confirms that HCl acts as a crystallising agent in this procedure [8] as no modulator was used in this synthesis (the role of a modulator will be explained in later chapters). The peak intensity and the sharpness of the peaks show that large crystalline frameworks are formed. Most patterns usually have a very large peak that spans approximately a 2θ range between 2–7°. This peak is not attributable to the UiO-66 phase and is observed for defective UiO-66 material. The inset shown in Figure 4.3 is a zoomed in image of this region and it reveals that the synthesised UiO-66 material does not contain this peak, further confirming the absence of cluster defects in this sample [25].

4.3.4 IR spectra

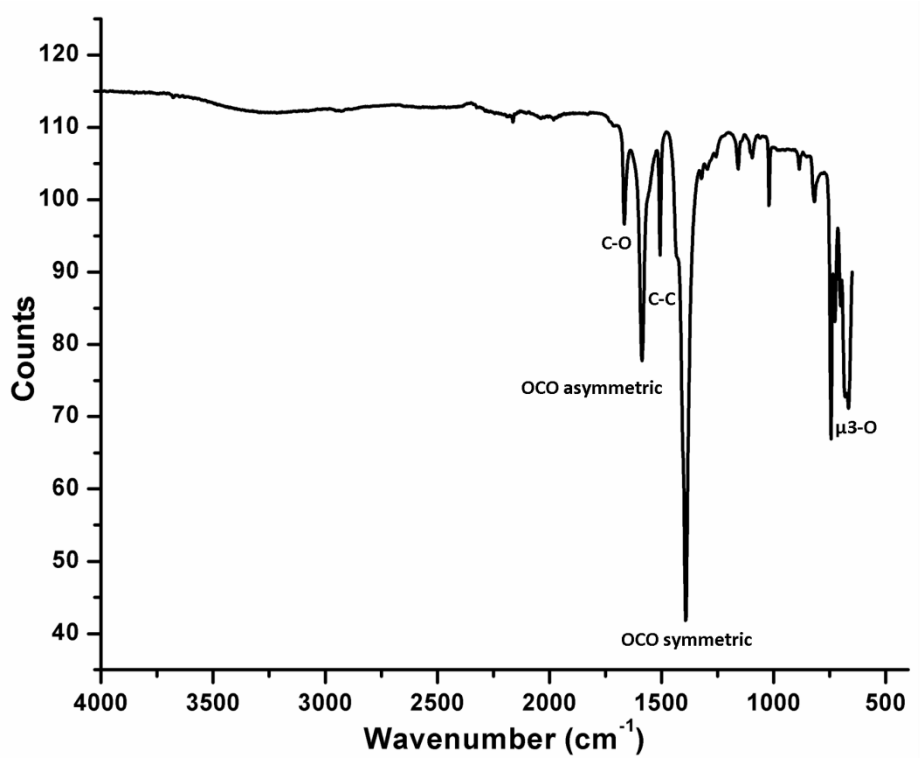

Figure 4.4. FT-IR spetra of the as-synthesised pristine UiO-66 MOF.

The IR spectra of the UiO-66 sample shows evidence for typical functional groups in UiO-66(Zr), indicated in Figure 4.4 The small band at about 1650 cm^{-1} represents the asymmetric C-O stretch of any remaining DMF inside the pores. The two intense bands at 1590 and 1395 cm^{-1} are due to the OCO asymmetrical and symmetrical stretching vibrations from the OCO asymmetrical and symmetrical stretching vibrations of the carboxylate group in H_2BDC. The small band at approximately 1510 cm^{-1} is due to the vibration of C-C in the benzene ring. The low frequency bands at 810, 740 and 710 cm^{-1} represent the C-H vibrations, C-C stretch, OH and OCO bends in H_2BDC. The band around 556 cm^{-1} is assigned to the asymmetrical Zr-(OC) asymmetric stretch and the bands around 657 and 474 cm^{-1} correspond respectively to the μ_3-O and μ_3-OH stretches. This confirms the structure of UiO-66.

4.3.5 Raman Spectroscopy

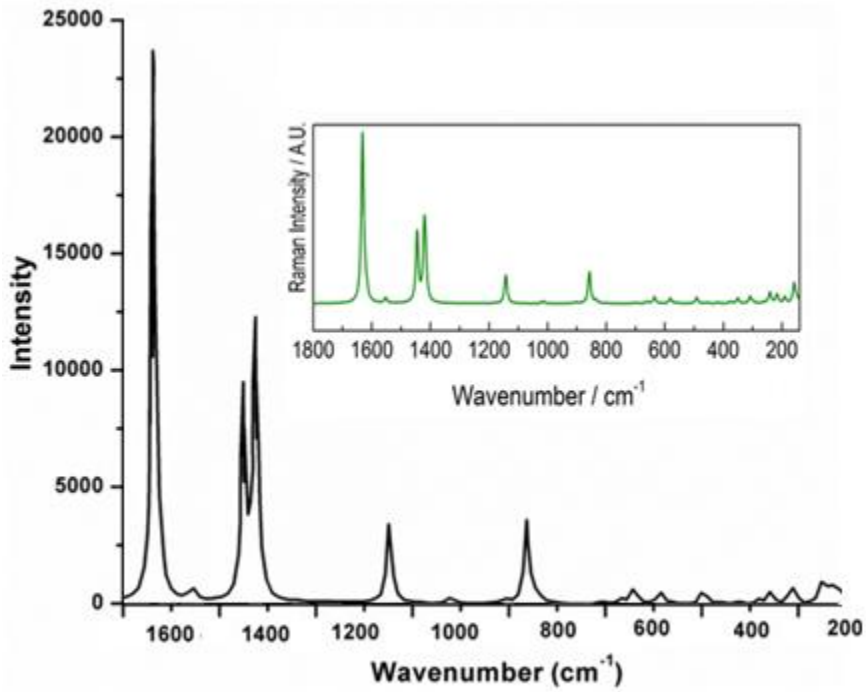

Figure 4.5. Comparison of the Raman spectrum of the as-synthesised pristine UiO-66 MOF with that simulated from an ideal model UiO-66 structure (insert) obtained with permission from Ref. [9].

It is apparent that the simulated Raman spectrum is closely comparable to that recorded experimentally on MOF UiO-66. This clearly highlights the ideal nature of the synthesised sample. The full range of the synthesised UiO-66 MOF can now be unequivocally allocated by envisaging the appropriate vibrational modes on the ideal MOF. This is only feasible owing to the close equivalence of experimental and simulated spectrum as shown in Figure 4.5. The assignment of the peaks is tabulated in Table 4.1.

Table 4.1. Raman peak assignment for both experimental and simulated spectra [9].

Experimental	**Simulated**	**Peak designation**
160.2	160 (163)	Cluster torsion mode
212.5	217 (221)	Zr-μ_3O asymmetric stretching
307.5	308 (314)	C-C-C out of phase bending
355.0	351 (358)	Out of phase framework bending
497.4	491 (501)	Zr-μ_3O symmetric stretching
580.5	581 (593)	C-C-C aromatic carboxylate in plane bending
640.0	635 (648)	In plane C-C-C aromatic ring bending
829.8	836 (853)	O-H bending
859.9	858 (875)	O-H bending and C-C symmetric breathing
1145.8	1143 (1166)	C-C symmetric breathing
1420.2	1420 (1449)	C-C aromatic to carboxylate stretch
1445.9	1445 (1474)	OCO carboxylate symmetric stretch
1632.9	1632 (1665)	C-C aromatic in phase stretch

4.3.6 Pore size distribution

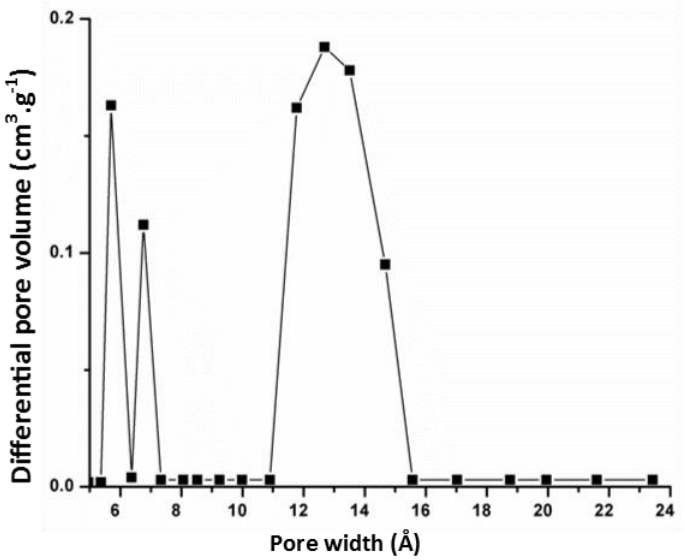

Figure 4.6. Pore size distribution (PSD) in the micropore region of the UiO-66 MOF synthesised under ideal conditions.

The pore size distribution curves shown in Figure 4.6 corresponds well with the reported pore sizes of ~6, 8 and 11 Å, corresponding to free diameters in tetrahedral cages, three-way windows and octahedral UiO-66 cages, respectively.

4.3.7 N_2 adsorption isotherm

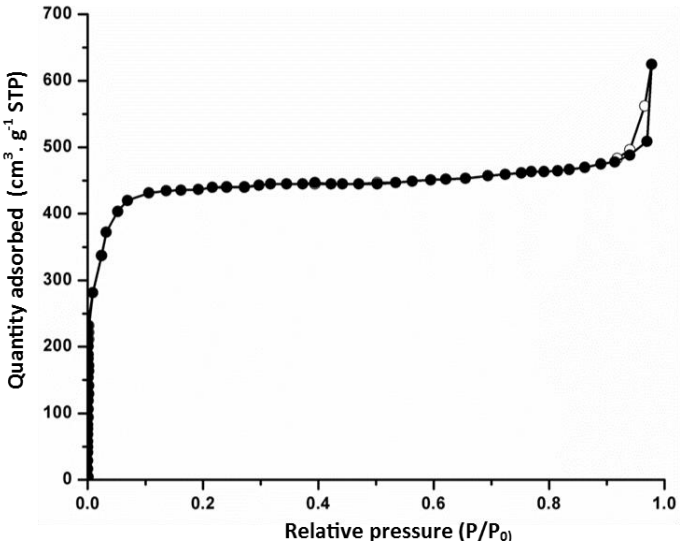

Figure 4.7. N_2 adsorption isotherm for UiO-66 MOF sample at 77 K.

The nitrogen adsorption isotherm (Figure 4.7) for UiO-66 is of type I, indicating that the UiO-66 is microporous. The synthesised defect-free material showed excellent N_2 adsorption capacity, which is higher than many reported data. The BET surface area was calculated to be 1275 $m^2.g^{-1}$.

4.3.8 Hydrogen uptake isotherm

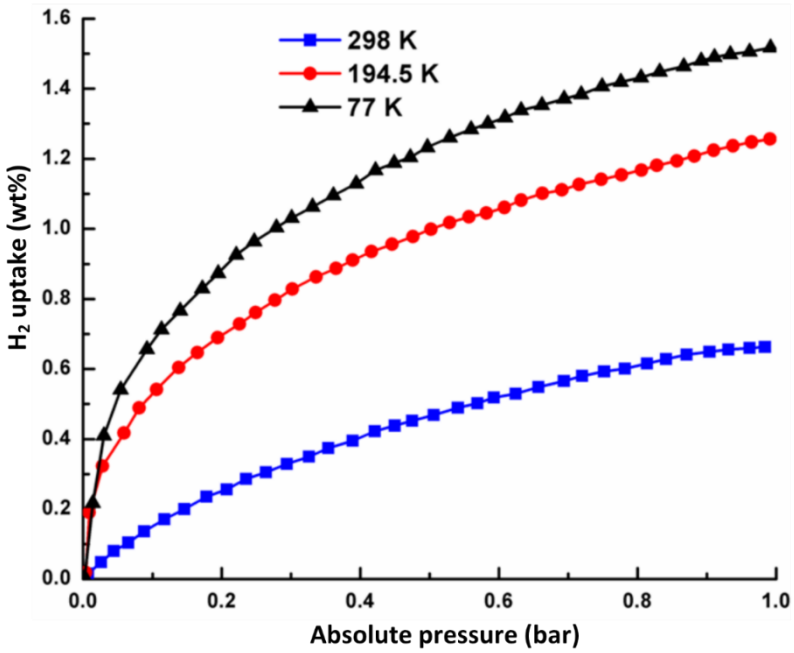

Figure 4.8. Low pressure gravimetric H_2 adsorption isotherms of UiO-66 (ideal) Zr-MOF at 77, 194.5 and 298 K.

In Figure 4.8, the hydrogen adsorption isotherm is plotted at three different temperatures and pressure of up to 1 bar. Hydrogen uptake for Zr-MOF at 77 K is 1.51 wt. %, similar to the literature data [24]. The hydrogen adsorption at 194.5 and 298 K is 1.19 and 0.59 wt. %, respectively. The H_2 adsorption increased with decreasing temperature with pressure of up to 1 bar and the curves were not saturated. Consequently, higher potential for hydrogen adsorption would be anticipated at high pressures. When the surface effect reaches saturation, the micropore volume becomes the dominant influence on the potential for hydrogen adsorption.

4.3.9 High pressure hydrogen uptake

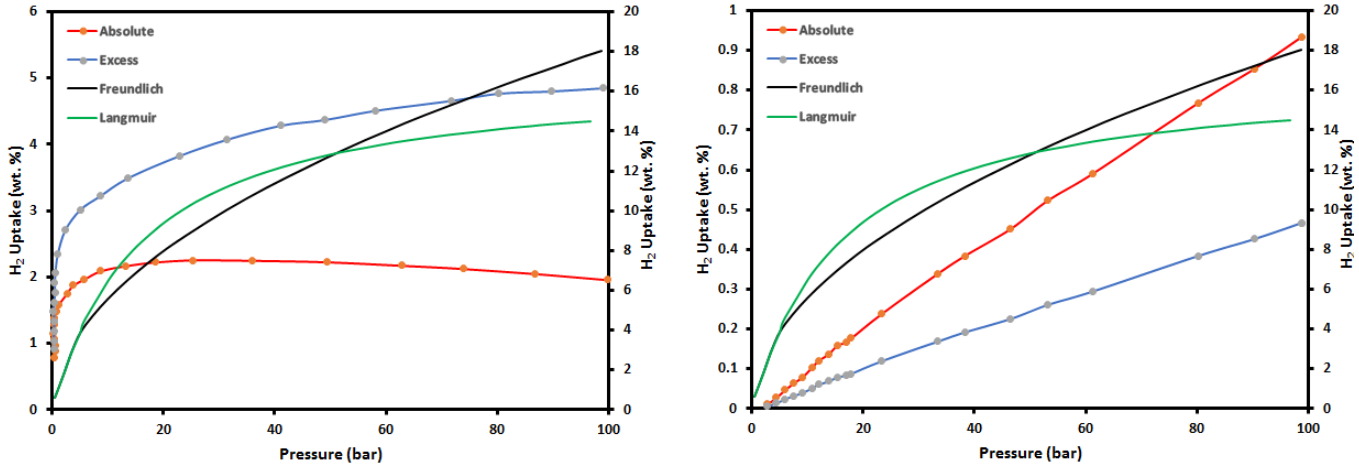

Figure 4.9. High pressure gravimetric hydrogen adsorption isotherms in Zr-MOF (UiO-66) at (a) 77 and (b) 298 K.

An Xemis instrument was used to determine the adsorption isotherm of Zr-MOF's at high pressures. Excess and absolute isothermic adsorption of hydrogen onto Zr-MOF at 77 K and 298 K for pressures of up to 100 bar are shown in Figure 4.9. At about 25-30 bar the maximum excess hydrogen intake at 77 K shows that a Zr-MOF adsorbent has not been fully saturated, which means hydrogen can be further adsorbed at higher pressures than 20 bar for absolute adsorption. Figure. 4.9b shows high temperature adsorption, at 298 K. H_2 is expected to be physically adsorbed into pore materials as the temperature rises suggesting that higher pressure is required to boost adsorption. The absolute adsorption at 77 K reached a maximum of 4.95 wt. %, which is higher than most reported data for UiO-66 MOF at 100 bars [14].

Table 4.2 Contrast of texture characteristics and absorbance of hydrogen on the synthesized Zr-MOF with literature results.

Properties	**Literature figures**	**This work**
Crystal size (nm)	200 [10], 100 [11], 150-200 [12], 200 [13]	>500
BET specific surface area ($m^2 \cdot g^{-1}$)	1080 [10], 1434 [11], 1358 [12], 1020 [13]	1367
Pore volume ($cm^3 \cdot g^{-1}$)	0.65 [11]	0.56
Micropore volume ($cm^3 \cdot g^{-1}$)	0.43 [11]	0.44
H_2 uptake at 77 K, 1 bar (wt. %)	1.28 [10], 1.6 [10], 1.49 [12], 1.24 [13]	1.51
H_2 uptake at 77 K, high pressure (wt. %)	2.1 (excess), 5.0 (absolute) [14]	1.95
H_2 uptake at 298 K, high pressure (wt. %)	0.38 (excess), 1.15 (absolute) [14]	0.9

4.4 Adsorption theories

4.4.1 Adsorption equilibrium

The Langmuir and Freundlich isotherm models [15] are utilised to correlate the adsorption isotherms of hydrogen in Zr-MOF.

The Langmuir isotherm is given as:

$$q = \frac{a_m bp}{1+bp} \quad \text{..... (1)}$$

where q is the adsorbed H_2 on Zr-MOF (wt. %), p is the H_2 pressure (bar), a_m (wt. %) and b (bar^{-1}) are the Langmuir parameters. These parameters can be obtained from the slope and intercept of the linear Langmuir plot of ($1/a_m$) versus ($1/p$).

The Freundlich isotherm is given as:

$$q = kp^{\frac{1}{n}} \quad \text{(2)}$$

where k and n are the Freundlich parameters, which are obtained from the experimental H_2 adsorption isotherms.

4.4.2 Adsorption kinetics

Hydrogen adsorption kinetics are also essential for storage of hydrogen by a specified material. It is necessary to determine mass-transfer coefficients to evaluate the rate of H_2 adsorption by the Zr-MOF crystals. To date, no gas adsorption kinetic information has been recorded for Zr-MOF. A diffusion model was defined according to Ruthven so as to process the hydrogen kinetic information to obtain the intracrystalline diffusivity [16]. By ignoring the heat transfer between particle and surrounding fluid, the diffusion equation is given as a spherical coordinate, and is written as:

$$\frac{\partial q}{\partial t} = \frac{1}{r^2}\frac{\partial}{\partial r}\left(r^2 D_c \frac{\partial q}{\partial r}\right) \quad \text{(3)}$$

where r is the radius of the equivalent sphere, D_c is the intracrystalline diffusivity and $q(r,t)$ is the quantity adsorbed at time t and radial position r. For constant diffusivity for a particular pressure, Eq. (3) can be adapted to

$$\frac{\partial q}{\partial t} = D_c\left(\frac{\partial^2 q}{\partial r^2} + \frac{2}{r}\frac{\partial q}{\partial r}\right) \quad \text{(4)}$$

The result of the Eq. (4) for the equivalent radius is specified as

$$\frac{\bar{q} - q_0'}{q_0 - q_0'} = \frac{m_t}{m_{max}} = 1 - \frac{6}{\pi^2}\sum_{n=1}^{\infty}\frac{1}{n^2}exp\left(\frac{-\pi^2 D_c t}{r_c^2}\right) \quad \text{(5)}$$

where, $\bar{q}$ is the average adsorbate concentration in the particle, given by:

$$\bar{q} = \frac{3}{r_c^3}\int_0^{r_c} qr^2\, dr \quad \text{(6)}$$

For fraction uptake $\frac{m_t}{m_{max}}$ greater than 70%, Eq. (6) can reduced to

$$1 - \frac{m_t}{m_{max}} = \frac{6}{\pi^2} exp(\frac{-\pi^2 D_c t}{r_c^2}) \quad \text{.....(7)}$$

4.4.3 Activation energy for diffusion and heat of adsorption

The activation energy E_a. of H_2 molecules adsorbed onto Zr-MOF crystals can be determined using the Arrhenius equation [17]:

$$ln\, k_2 = ln\, A_0 - \frac{E_a}{RT} \quad (8)$$

where E_a. is the activation energy (kJ.mol^{-1}), k_2 is the pseudo-second-order rate constant, A_0 is the Arrhenius factor, R is the gas constant (8.314 J.mol^{-1}.K^{-1}) and T is the solution temperature (K). The values of A_0 and E_a. can be determined from the intercept and slope of the ln k_2 versus 1/T plot.

Isosteric heat of adsorption is also a significant criterion for storing hydrogen through physisorption, and can be obtained from van't Hoff equation:

$$\frac{\Delta H}{RT^2} = -(\frac{\partial\, ln\, p}{\partial T})_a \quad \text{.....(9)}$$

where ΔH is the isosteric heat of adsorption (kJ·mol^{-1}), T is temperature, p is pressure (bar), a is the adsorption amount (wt. %), and R is the universal gas constant. Integrating equation (9) we get:

$$ln\, p = \frac{\Delta H}{RT} + C \quad \text{.....(10)}$$

where C is a constant of integration

$$D_c = D_c^0 exp - \frac{E_a}{RT} \quad \text{.....(11)}$$

where D_c^0 is an equation constant, E_a is the activation energy for diffusion.

Both Langmuir and Freundlich equations were utilised to compare the hydrogen adsorption isotherms of Zr-MOF. The equation parameters from linear regression of the isotherms of hydrogen adsorption presented in Figure 4.9 are listed in Table 4.2. The Langmuir equation corresponds better than the Freundlich equation to the adsorption isotherms for low pressure hydrogen uptake. It must be emphasised that the adsorption isotherm only defines absolute adsorption and not excess adsorption, which is significantly lower than absolute adsorption because of the high-pressure buoyancy correction.

Table 4.3. Summary of adsorption isotherm model parameters for hydrogen in Zr-MOF

Isotherm model	**Parameters**	**T=77 K (high pressure)**	**T=298 K (high Pressure)**	**T=77 K (low pressure)**	**T=194.5 K (low pressure)**	**T=298 K (low pressure)**
Langmuir	a_m (wt. %)	3.28	0.90	1.25	1.00	0.99
	B (bar^{-1})	0.33	1.50	0.57	0.29	1.78
	R^2	0.82	0.63	0.88	0.76	0.64
Freundlich	κ	0.74	0.62	1.57	1.29	8.13×10^{-3}
	N	2.63	0.97	2.67	2.54	1.37
	R^2	0/79	0.63	0.92	0.89	0.82

Table 4.2 lists the values and the coefficients of the fitting parameters of the Freundlich and Langmuir isotherms. An analysis of the regression coefficient (R^2) can be used to determine the optimal isothermal model. Both the parameters derived from the implementation of the

Langmuir model may be of relevance to interpret the sorption information, and the calculated equilibrium value may very well be an internal reference indicator for understanding how favoured adsorption is. Normally, for Langmuir adsorption parameters, relatively small numbers of *b* (Langmuir variable) indicate that the absorbent is effective at a low solution rate. It can be noted from Figure 4.9 that the experimental isotherm information is reasonably consistent with Langmuir model predictions at low pressures. The information in Table 4.2 reveals that the *k* values gradually decrease with temperature, which is consistent with the behaviour of physisorption [18], and adsorption intensity (n) >1 shows that adsorption of H_2 on Zr-MOF is favourable under the investigated circumstances. These results imply that the Freundlich isothermic equation corresponds well with the experimental data.

By calculating the quantity of H_2 adsorbed on a monolayer may be used to measure the degree of coverage that gives an indication on the surface which is still accessible for adsorption. and suggests the effectiveness for further adsorption by increasing pressure as described below. The percentage of monolayer coverage can be determined by the following equation under the conditions studied:

$$X_{monolayer} = \frac{qA_0N_A}{S_A} \quad \text{..... (10)}$$

where q (mmol.g^{-1}) is the uptake capacity, S_A is the Langmuir surface area (1275 m^2.g^{-1}), A_0 is the adsorbate cross-sectional area estimated from the molecular kinetic diameter assuming a spherical shape (0.14 Å^2 for H_2) [19,20], and N_A is Avogadro's number (6.02 × 10^{23} molecules/mol).

In the low-pressure range of 0.1-1 bar, the degree of exposure of H_2 to Zr-MOF crystals is as low as 20%, which suggests that Zr-MOF can adsorb more H_2 by increasing the pressure [21]. From Figure 4.9 it is noticed that the experimental isothermic information shows a small

increase in the adsorbed amount of H_2 with an increase in pressure, and that the highest adsorption capacity of H_2 on Zr-MOF is observed at 77 K and 100 bar. The coverage of H_2 on Zr-MOF crystals is calculated as 70%, and there is resistance to further sorption resulting in an isothermic adsorption plateau.

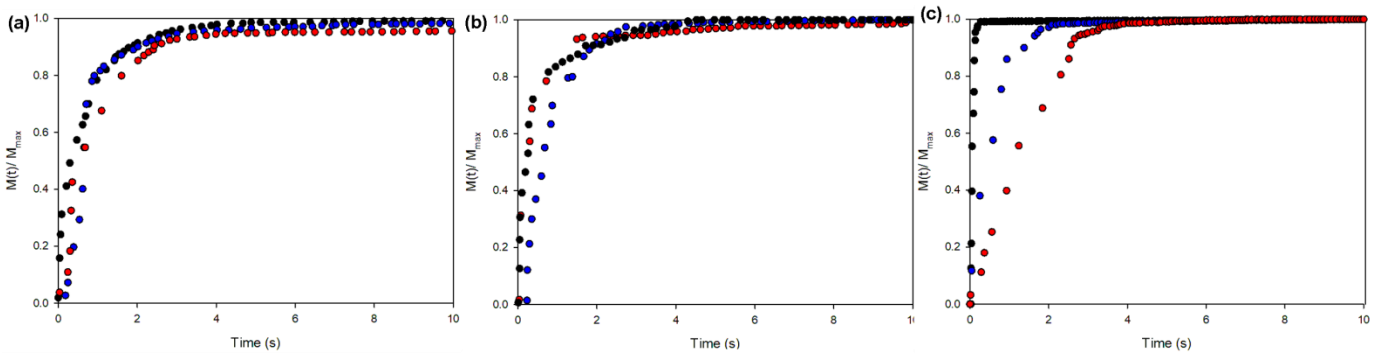

Figure 4.10. Hydrogen adsorption kinetics in pristine Zr-MOF (UiO-66) at (a) 77 K, (b) 194.5 K and (c) 298 K at pressures 0.35 (Red), 0.65 (Blue) and 1.00 bar (Black).

Table 4.4. Diffusion time constants for hydrogen adsorption in Zr-MOF at various temperatures.

	T = 77 K	**T = 194.5 K**	**T = 298 K**
P (bar)	D_c/r_c^2 (s^{-1})	D_c/r_c^2 (s^{-1})	D_c/r_c^2 (s^{-1})
0.35	0.041	0.046	0.123
0.65	0.065	0.087	0.160
1.00	0.082	0.105	0.201
Average	**0.063**	**0.238**	**0.484**

The hydrogen adsorption kinetic information was recorded by the Micromeritics ASAP 2020 adsorption instrument during measurement of the low-pressure hydrogen adsorption isotherms presented in Figure 4.8. Figure 4.10 shows the fractional adsorption uptake curves at different hydrogen pressures and at three temperatures (77 , 194.5 and 298 K). It was presumed that the Zr-MOF crystals were ideal regions to apply the diffusion model provided in Eq. (7), correlating hydrogen adsorption kinetic information. The formula enables us to measure the hydrogen diffusion (s^{-1}) time constants at different temperatures, namely 77, 194.5 and 298 K and their average values are indicated in Table 4.3. Figure 4.11 show how diffusion time constants increase with temperature and hydrogen pressure, which is anticipated due to elevated kinetic energy at high temperatures. The increase with pressure is due to surface diffusion, where the increased amount of hydrogen adsorption facilitates hydrogen transport at lower hydrogen pressure in the pores of Zr-MOF.

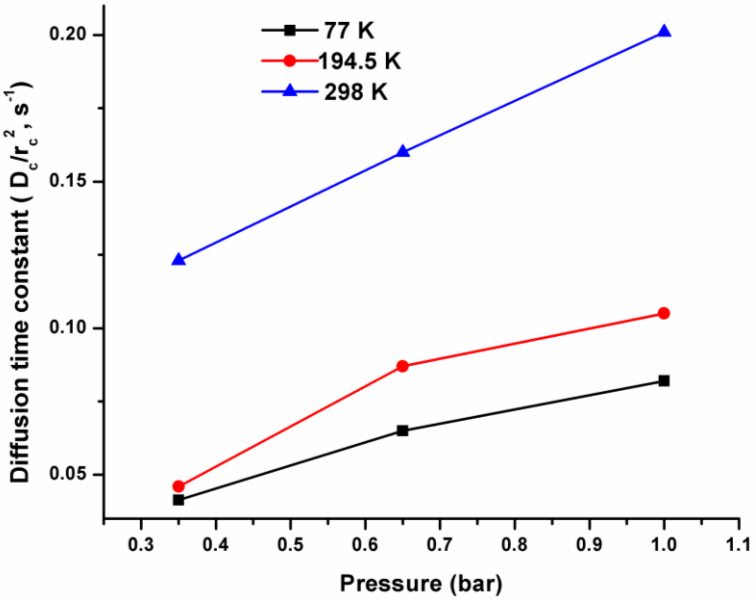

Figure 4.11. Effect of pressure and temperature on hydrogen pore diffusivity in an ideal UiO-66-MOF (Zr)

The significance of hydrogen adsorption/desorption kinetics is clearly stated in the DOE requirements for hydrogen storage. In automotive fuel cell applications, the time interval for adsorption and removal of hydrogen from the hydrogen storage tank is limited. The kinetic findings of this study reveal that the adsorption of hydrogen by UiO-66 is efficient enough to prevent the adsorption and discharge of hydrogen from the porous media from causing problems.

From the diffusivity data at three different temperatures, we estimated the activation energy for hydrogen diffusion inside UiO-66 according to Eq. (11). It was found that the activation energy for hydrogen diffusion in UiO-66 MOF is 3.66 kJ.mol^{-1}, which is higher as compared with the activation energy for small hydrocarbon molecules diffusion in zeolite. In this study, the heat of adsorption was measured using two hydrogen adsorption isotherms at 77 and 298 K. The isotherms were first converted to isosteres, p vs T plots at the specified amount of adsorption. The adsorption heat was then determined in accordance with Eq. (10) from the isostere slopes. Figure 4.13, shows that adsorption energy decreases significantly with hydrogen loading.

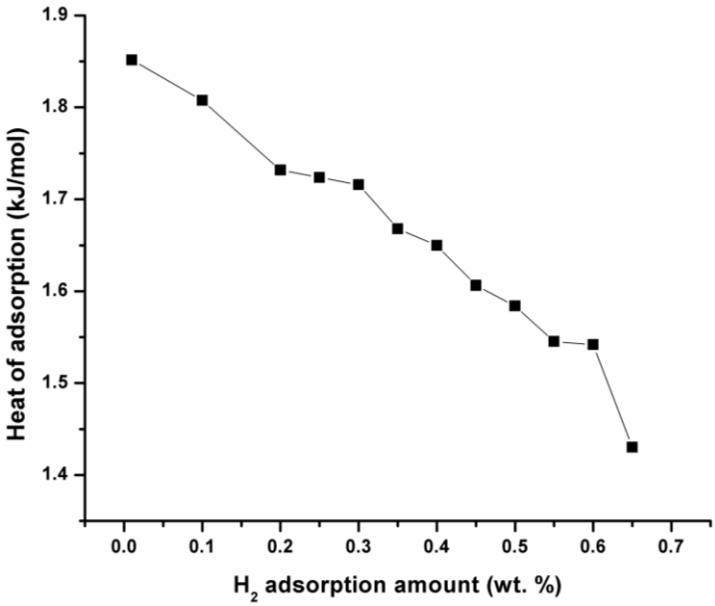

Figure 4.13. Effect of adsorption amount on isosteric heat of hydrogen adsorption in Zr-MOF.

The heat of adsorption was measured using the three isotherms at 77 , 194.5 and 298 K in this study. Figure 4.13 shows the impact of the adsorbed hydrogen on isosteric heat. The heat adsorption value for hydrogen obtained in the Zr-MOF is approximately 1.85 kJ·mol^{-1}, this is lower than the reported value of the 4.00 kJ·mol-1 by Gogotsi group [22].

The dramatic drop in hydrogen uptake at ambient temperature is due to the small heat of adsorption. Therefore, it is important to raise the heat of adsorption to improve hydrogen storage capacity at ambient temperature and at low to medium pressure. This observation agrees with the results of molecular simulation, which show that the adsorption of hydrogen in MOF materials is determined by low-pressure heat of adsorption, specific surface area at medium pressure and pore quantity at high pressures [23].

4.5 **Conclusion**

We have successfully produced non-defective UiO-66 MOF. By using TGA and PXRD we have been able to elaborate on the missing linkers and missing clusters. The synthetic method utilised HCl, which promoted the formation of octahedral crystals of size ~ 600 nm. HCl has a double function during crystal formation: it accelerates the hydrolysis of $ZrCl_4$ and promotes the deprotonation of the carboxylic acids. HCl therefore favors the incorporation of the H_2BDC linkers. As we did not observe any formation of defects, we are able to conclude that HCl does not bring about the formation of extra active sites. The Freundlich adsorption equation can be used for low pressure isotherms and hydrogen adsorption at high pressure. Kinetic adsorption data were obtained, and hydrogen adsorption was calculated for diffusivity in Zr-MOF adsorbent. The hydrogen adsorption activation energy in Zr-MOF and the isosteric heat of adsorption were estimated.

The hydrogen diffusion activation energy was estimated to be 4.65 kJ·mol^{-1} and the heat of adsorption is lower than 2 kJ·mol^{-1}. The results obtained for hydrogen uptake, BET surface

area and pore size distribution are aligned with reported data for a simulated pristine UiO-66 MOF. We are therefore satisfied with the information reported herein for a pristine UiO-66 MOF material.

4.6 References

1. Shearer, G.C., Chavan, S., Ethiraj, J., Vitillo, J.G., Svelle, S., Olsbye, U., Lamberti, C., Bordiga, S. and Lillerud, K.P., Tuned to perfection: ironing out the defects in metal–organic framework UiO-66. Chem. Mater., 2014, 26(14), 4068-4071.
2. Valenzano, L. Civalleri, B. Chavan, S. Bordiga, S. Nilsen, M. H. Jakobsen, S. Lillerud, K. P. and Lamberti, C. *Chem.Mater.*, **2011**, 23, 1700.
3. Cmarik, G.E., Kim, M., Cohen, S.M. and Walton, K.S., Tuning the adsorption properties of UiO-66 via ligand functionalization. *Langmuir*, **2012**, *28*(44), 15606-15613.
4. Yang, D., Ortuño, M.A., Bernales, V., Cramer, C.J., Gagliardi, L. and Gates, B.C., Structure and dynamics of Zr6O8 metal–organic framework node surfaces probed with ethanol dehydration as a catalytic test reaction. *J. Am. Chem. Soc.*, **2018**, 140(10), 3751-3759.
5. Lemaire, P.C., Lee, D.T., Zhao, J. and Parsons, G.N., Reversible low-temperature metal node distortion during atomic layer deposition of Al2O3 and TiO2 on UiO-66-NH_2 metal–organic framework crystal surfaces. *ACS Appl. Mater. Interfaces*, **2017**, *9*(26), 22042-22054.
6. Nath, I., Chakraborty, J. and Verpoort, F., Metal organic frameworks mimicking natural enzymes: a structural and functional analogy. *Chem. Soc. Rev*. **2016**, 45(15), 4127-4170.
7. Aguilera-Sigalat, J., Fox-Charles, A. and Bradshaw, D., Direct photo-hydroxylation of the Zr-based framework UiO-66. *Chem. Commun.*, **2014**, 50(97), 15453-15456.
8. Cavka, J.H., Jakobsen, S., Olsbye, U., Guillou, N., Lamberti, C., Bordiga, S. and Lillerud, K.P., A new zirconium inorganic building brick forming metal organic frameworks with exceptional stability. *J. Am. Chem. Soc.*, **2008**, 130(42), 13850-13851.

9. Shearer, G.C., Chavan, S., Ethiraj, J., Vitillo, J.G., Svelle, S., Olsbye, U., Lamberti, C., Bordiga, S. and Lillerud, K.P., Tuned to perfection: ironing out the defects in metal–organic framework UiO-66. *Chem. Mater.*, **2014**, *26*(14), 4068-4071.
10. Cavka JH, Jakobsen S, Olsbye U, Guillou N, Lamberti C, S. Bordiga, et al. A new zirconium inorganic building brick forming metal organic frameworks with exceptional stability. *J. Am. Chem. Soc.,* **2008**; 130:13850–1.
11. Abid HR, Tian HY, Ang HM, Ang MO, Tade MO, Buckley CE, et al. Nanosize Zr-metal organic framework (Uio-66) for hydrogen and carbon dioxide storage. *Chem. Eng. J.,* **2012**; 187:415–20.
12. Zhao Q, Yuan W, Liang JM, Li JP. Synthesis and hydrogen storage studies of metal-organic framework UiO-66. *Int. J. Hydrogen Energy*, **2013**, 38: 13104-13109.
13. Hafizovic J, Olsbye U, Lillerud KP, Jacobsen S, Guillou N. Metal organic framework compounds. US 2012/0115961 A1, May 10, **2012**.
14. Bambalaza, S.E., Langmi, H.W., Mokaya, R., Musyoka, N.M., Ren, J. and Khotseng, L.E.,. Compaction of a zirconium metal–organic framework (UiO-66) for high density hydrogen storage applications. *J. Mater. Chem. A*, **2018,** 6(46), pp.23569-23577
15. Saha D, Wei ZJ, Deng SG. Equilibrium, kinetics and enthalpy of hydrogen adsorption in MOF-177. *Int. J. Hydrogen Energy*. **2008**, 33, 7479-7488.
16. Ruthven DM. Principles and adsorption and adsorption processes. Ed.; Willey Interscience pp.160-68. 1984.
17. Schoenecker, P.M., Belancik, G.A., Grabicka, B.E. and Walton, K.S., Kinetics study and crystallization process design for scale-up of UiO-66-NH_2 synthesis. *AIChE J.* **2013**, *59*(4), 1255-1262.

18. Bambalaza, S.E., Langmi, H.W., Mokaya, R., Musyoka, N.M., Ren, J. and Khotseng, L.E., Compaction of a zirconium metal–organic framework (UiO-66) for high density hydrogen storage applications. *J. Mater. Chem. A*, **2018**, 6(46), 23569-23577.

19. Emmett PH, Brunauer S. The use of low temperature van der Waals adsorption isotherms in determining the surface area of iron synthetic ammonia catalysts. *J Am Chem Soc* **1937**, 59, 1553–64.

20. Nijkamp MG, Raaymakers JEMJ, van Dillen AJ, de Jong KP. Hydrogen storage using physisorption-materials demands. *Appl. Phys A*. **2002**, 72, 619–23.

21. Rossetti I, Ramis G. Quantification of 'delivered' H_2 by a volumetric method to test H_2 storage materials. *Int. J. Hydrogen Energy*, **2013**, 38, 13309–13317.

22. Yushin, G., Dash, R., Jagiello, J., Fischer, J.E. and Gogotsi, Y., Carbide-derived carbons: effect of pore size on hydrogen uptake and heat of adsorption. *Adv. Funct. Mater.*, **2006**, *16*(17), 2288-2293.

23. Frost H, Düren T, Snurr RQ. Effects of surface area, free volume, and heat of adsorption on hydrogen uptake in metal-organic frameworks. *J. Phys. Chem. B* **2006**, 110, 9565–70.

24. Zhao Q, Yuan W, Liang JM, Li JP. Synthesis and hydrogen storage studies of metal-organic framework UiO-66. *Int. J. Hydrogen Energy*, **2013**, 38: 13104-13109.

25. Cliffe, M.J., Wan, W., Zou, X., Chater, P.A., Kleppe, A.K., Tucker, M.G., Wilhelm, H., Funnell, N.P., Coudert, F.X. and Goodwin, A.L., Correlated defect nanoregions in a metal–organic framework. *Nat. Commun.*, **2014**, 5, 4176.

CHAPTER 5: DE-NOVO DEFECT ENGINEERING

5.1 Modulator variation

5.1.1 Abstract

The presence of porosity is one of the main characteristics of MOF materials that give them attractive properties necessary for potential application in various areas, such as fuel storage (hydrogen and methane), carbon capture and catalytic applications, just to mention a few [2-5]. Rather wide pores within a MOF are highly detrimental to hydrogen storage, as H2 molecules close to the centre of the pore are less likely to encounter any attraction from the surface of the pore walls. Correspondingly, these low-density solids may have relatively low volumetric H2 adsorption capacities. Indeed, it is obvious that a substantial micropore volume comprised of small voids is more suitable for an efficient storage medium [6]. For such a purpose, framework interpenetration, hydrogen spill-over and porosity tailoring have been established to adjust pore size and structure in MOFs for optimum hydrogen adsorption at low pressure and ambient temperatures [7]. Hydrogen spill-over is the surface migration of activated H atoms from a hydrogen-rich metal cluster to the surface of a catalyst where hydrogen dissociation is impossible. Bai et al. [8-10] and Feng et al. [11] also confirmed that the coexistence of micro- and mesopores in MOFs mediate greater H2 heat of adsorption for sufficiently strong physisorption adsorption from inter-crystalline mesopores. As verified by Psofogiannakis et al. [12] the adsorption of hydrogen in MOF materials is significantly influenced by structural defects. UiO-66 is well recognised as the prototypical Zr-MOF with a face-centred cubic crystalline structure. The Zr ion is bound to eight oxygen atoms in the as-synthesised product, and six of them cluster tightly to form the Zr6O4(OH)4 metal centre [13, 14]. A perfect UiO-66 crystal has a 12-connected framework structure; however, it was recently proven that an 'ideal' material may have missing-linker defects, and the hydrogen adsorption

behavior patterns deviate from those anticipated for a defect-free crystal [15-16]. Many methods have been pursued to identify the structural defects in UiO-66 for hydrogen storage as it has been established that the diffusion of atomic H in the MOFs is significantly aided by structural defects. It has been shown that the UiO-66 can tolerate up to 4.3 missing linker defects per [Zr6O4(OH)4]12+ node, with more defect densities compromising the structural integrity and porosity of the network [17].

In this research, a series of experiments were undertaken to consider the effect of the amount of modulator on the framework of the UiO-66(Zr) samples and their hydrogen storage efficiency. Structural defects within UiO-66 also disclosed the observations that the BET values of the defective MOFs were considerably larger than those of the non-defective ones, which then in turn led to more adsorption of hydrogen.

5.1.2 Synthesis

5.1.2.1 Reagents and Chemicals

Zirconium chloride ($ZrCl_4$, Sigma-Aldrich, >99.5%), terephthalic acid (Sigma-Aldrich, 98%), formic acid (HCOOH, Sigma-Aldrich, >95%) and N,N-dimethylformamide (DMF, Sigma-Aldrich, 99.8%) were purchased and used with no further purification.

5.1.2.2 Preparation UiO-66 (Zr) nanocrystals with formic acid modulator

The non-defective UiO-66 sample was synthesised according to a previously reported procedure with minor changes [1]. Typically, 2.4 g (7.4 mmol) zirconium chloride and 1.0 g (6.0 mmol) terephthalic acid were dissolved in 100 ml DMF. The two solutions were mixed together and 20 ml formic acid was added. The mixture was placed in a pre-heated oven at 408 K for 2 days. Evacuated samples were obtained by washing the as-synthesised crystals twice a day for 3 days, first with DMF to remove any unreacted material and then with methanol. They were activated under vacuum at 423 K and the product was stored in a glovebox. Yield: 65%

(2.2 g). Depending on the amount of modulator used, a certain portion of the H_2BDC linkers are replaced, resulting in missing linker defects. Knowing this, defects were introduced by varying the volumes of the formic acid used in the above-mentioned procedure, keeping all the other variables constant, as shown in Table 5.1.

Table 5.1. Table showing amounts of formic acid used for the synthesis of defective material.

DMF: formic acid volume ratio	**Amount of formic acid added (ml)**	**Yield (%)**
1:1	100	59 (2.0 g)
1:1.5	150	62 (2.1 g)
1:2	200	56 (1.9 g)
1:2.5	250	53 (1.8 g)

5.1.3 Results and discussion

5.1.3.1 SEM images

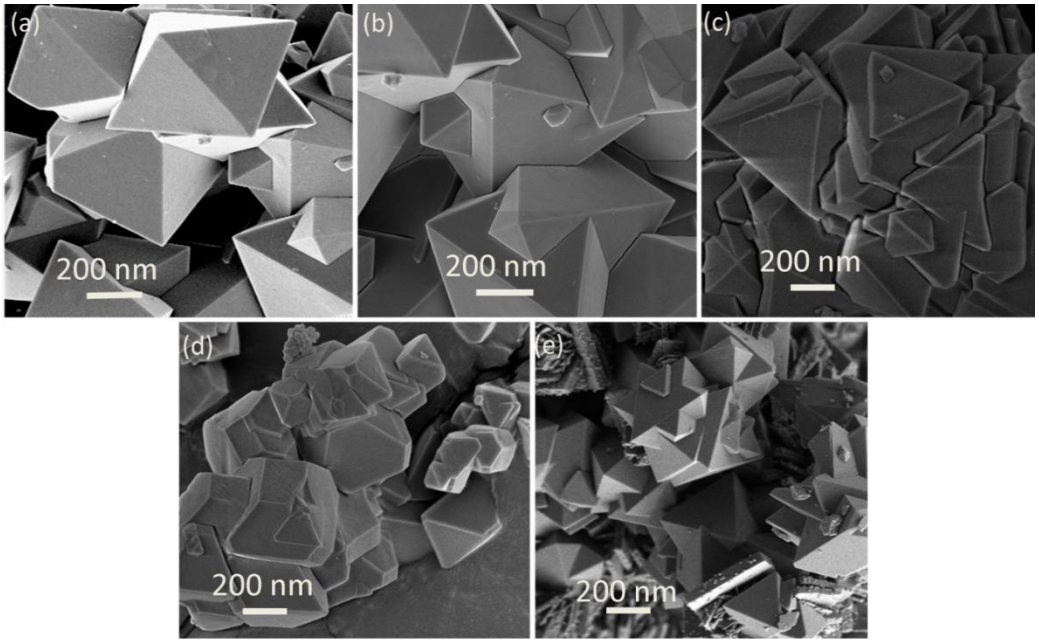

Figure 5.1. SEM images of (a) non-defective UiO-66 and (b) 1:1 (c) 1:1.5 (d) 1:2 (e) 1:2.5 defective UiO-66 modulated using formic acid of 100 - 250 ml.

With regard to UiO-66, it is known that reacting $ZrCl_4$ with H_2BDC linker precursor results in intergrown aggregates of small crystallites. This is a significant limitation in the identification of defects in UiO-66 MOFs. In this study we employed formic acid as a modulator to overcome this limitation. The addition of a monocarboxylic acid such as formic acid as a modulator makes it possible for the crystals to expand into significantly larger dimensions having well-defined octahedral form. [18]. Figure 5.1 allows us to conclude that with varying amounts modulator the sizes and shapes of the UiO-66 crystals vary significantly. However, no direct correlation was noticed between the amount of modulator and the size of the crystals. It was revealed that since the only variation on the synthesis procedure was the ratio of formic acid to DMF, we can conclude that 1:1.5 and 1:2 (DMF:FA) ratios resulted in smaller octahedral crystals, which

were not morphologically perfect. The ratios 1:1 and 1:2.5 showed larger and non-octahedron crystallites.

5.1.3.2 PXRD patterns

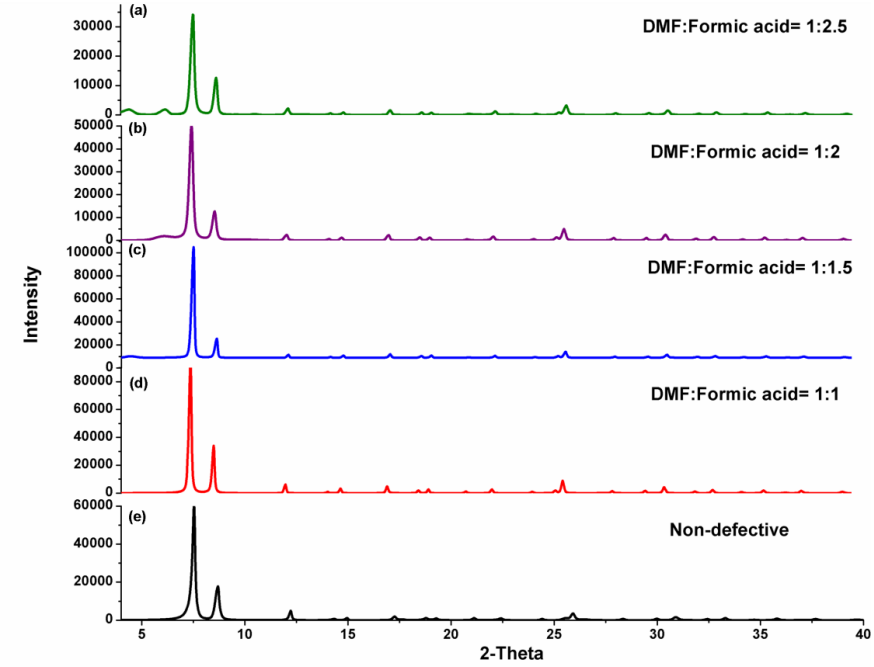

Figure 5.2. PXRD patterns of non-defective (synthesised with HCl) and defective (synthesised with formic acid) MOFs.

The PXRD displayed in Figure 5.2 shows a complete set of crystalline phase reflections, and the successful synthesis of Zr-MOF was verified by seven conventional signals at 2θ = 7.4°, 8.5°, 14.1°, 14.7°, 17°, 18.6° and 19.0°. The PXRD patterns confirm that no phase transition occurred as the modulator volume was increased, since the peak positions remained the same for all samples. New peaks are observed between 3-7° Θ; these peaks are due to reo phase, which is a form of UiO-66 with missing-cluster defects. The intensities of these new peaks increase with increasing modulator concentration, which suggests an increase in defect concentration.

5.1.3.3 TGA

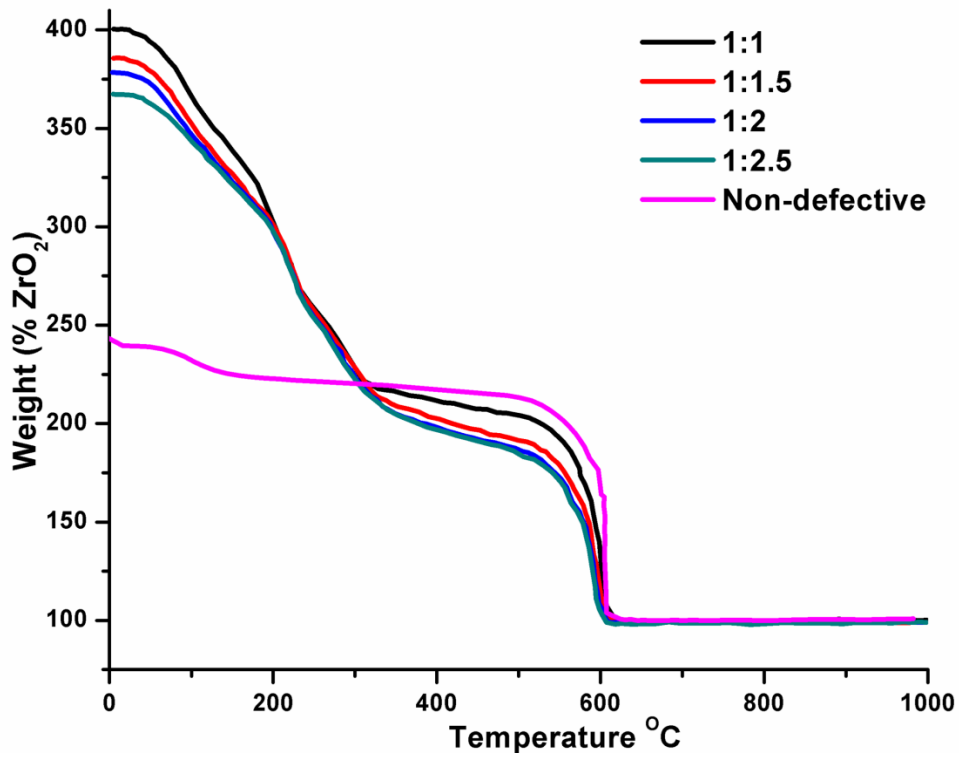

Figure 5.3. TGA curves for non-defective UiO-66(Zr) and defective UiO-66 MOF samples

Figure 5.3 shows that the TGA plateau was lower as the modulator concentration was increased. This makes sense if one interprets this as the retrieval/replacement of linkers resulting in a linker deficient structure. The plateau gradually shifts from the predicted TGA of an ideal UiO-66 MOF. The samples all have a similar decomposition temperature of approximately 793 K and is in accordance to literature [19].

5.1.3.4 N_2 adsorption isotherms

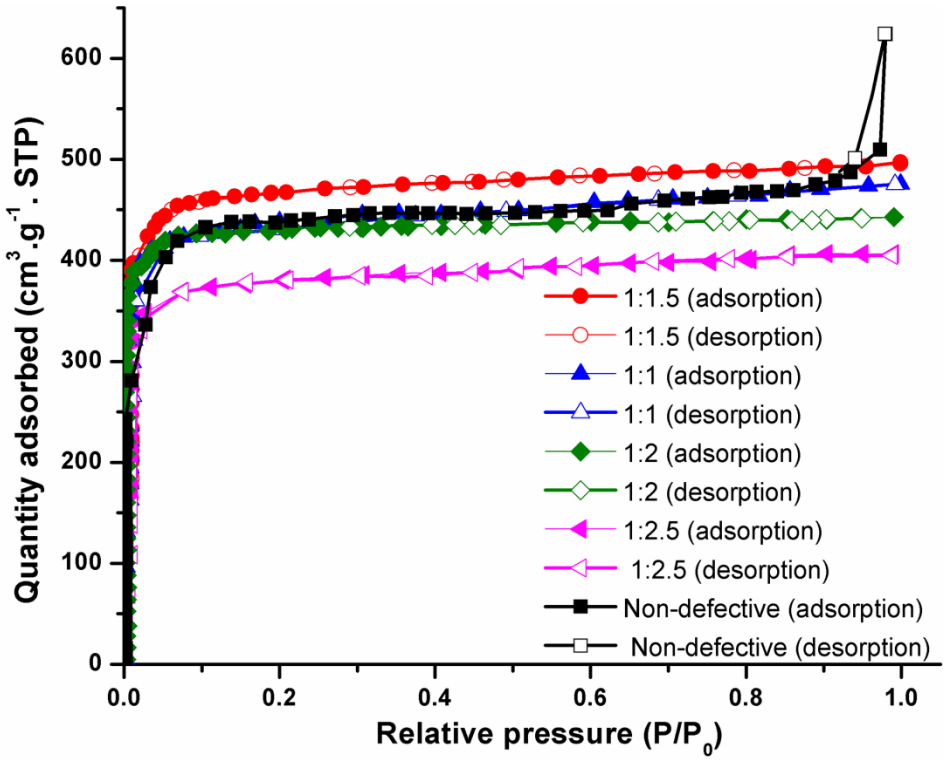

Figure 5.4. N_2 adsorption isotherms for samples synthesised using variable amounts of formic acid (modulator) and non-defective sample.

The N_2 sorption studies at 77 K confirmed the permanent porosity of activated UiO-66 synthesised with a variable amount of formic acid. The BET surface areas obtained from Figure 5.4 are 1612.2, 1218.4, 1095.9 and 904.4 $m^2.g^{-1}$ for 1:1.5, 1:1, 1:2 and 1:25 DMF:FA, not necessarily following a consistent trend. A higher percentage of defects results in an increase and then a decrease in surface area as more modulator is added. The BET surface area of the non-defective sample was 1275 m^2 g^{-1} as reported in Chapter 4. After additional missing linker defects were established, there was no improvement in the surface area for the 1:2 and 1:2.5, which suggests that high porosity detected in UiO-66 samples could be due to missing cluster defects rather than missing linkers. However, further studies targeted at identifying missing cluster defects would be required in order to confirm this assumption.

5.1.3.5 H_2 uptake

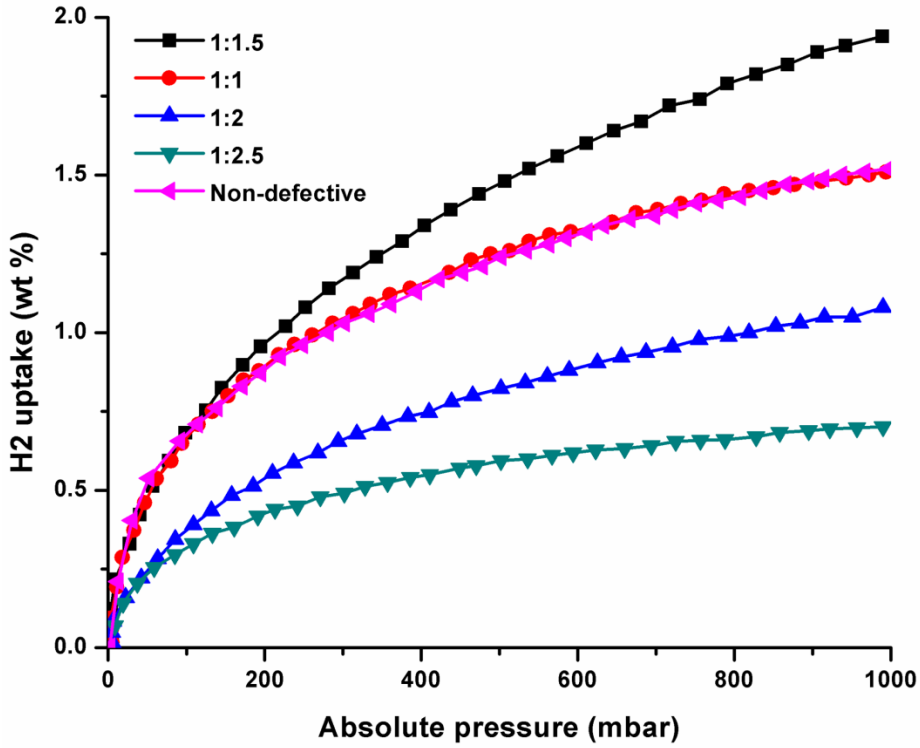

Figure 5.5. H_2 sorption isotherms for non-defective and defective UiO-66 MOFs at 77 K and 1 bar.

From Figure 5.5 it can be seen that the ratio of 1:1.5 FA:DMF performs much better than the non-defective material, with an uptake of 1.94 wt. %. The 1:1 ratio has an uptake that is equal with that of the non-defective sample, uptake of 1.51 wt. %. As the amount of modulator is further increased, we observe a decrease in the uptake as we do for the surface area. Therefore, we see a direct correlation in surface area and H_2 uptake. The 1:2.5 ratio showed the lowest performance, with an uptake of 0.702 wt. %, which is lower than reported in the literature [20].

5.2 Linker variation

5.2.1 Abstract

In this section, we discuss and compare materials which were synthesised using different linker concentrations. All the other reaction parameters were kept constant.

5.2.2 Synthesis

5.2.2.1 Reagents

Zirconium chloride ($ZrCl_4$, Sigma-Aldrich, >99.5%), terephthalic acid (Sigma-Aldrich, 98%), formic acid (HCOOH, Sigma-Aldrich, >95%), acetic acid (≥ 99.7%) and N,N-dimethylformamide (DMF) Sigma-Aldrich, 99.8. All reagents were used as provided.

5.2.2.2 Procedure

0.7 g (3.00 mmol) of zirconium chloride, 45 mL of DMF (42.48 g, 580 mmol) and 0.52 mL (0.55 g, 9.09 mmol) of formic acid were added to a 100 mL round bottom reaction flask. A magnetic stirrer bar and H_2BDC linker (0.05 g, 0.30 mmol) were added to the solution. The solution was heated on a hot plate at 473 K for 5 h during which a visible change from colourless to white was observed. The reaction was further heated for 18 hours, after which the solution was cooled to room temperature. The resultant solution was sonicated for 30 s and allowed to stir for 18 h at 25 °C at 200 rpm. The MOF was isolated from the supernatant by centrifugation and washed 3 times using DMF and the solvent was exchanged with methanol. Samples were placed in a vacuum oven at 80 °C overnight prior to analysis. Different ratios of $ZrCl_4$:H_2BDC were prepared as indicated in Table 5.2.

Table 5.2. Amounts of linker (H_2BDC) used

Sample	Mass of H_2BDC added (g)	Number of moles (mmol)

UiO-66-1:0.1	0.05	0.30
UiO-66-1:0.5	0.25	1.50
UiO-66-1:1	0.46	3.00
UiO-66-1:1.5	0.76	4.50

5.2.2 Results and discussion

5.2.2.1 SEM images

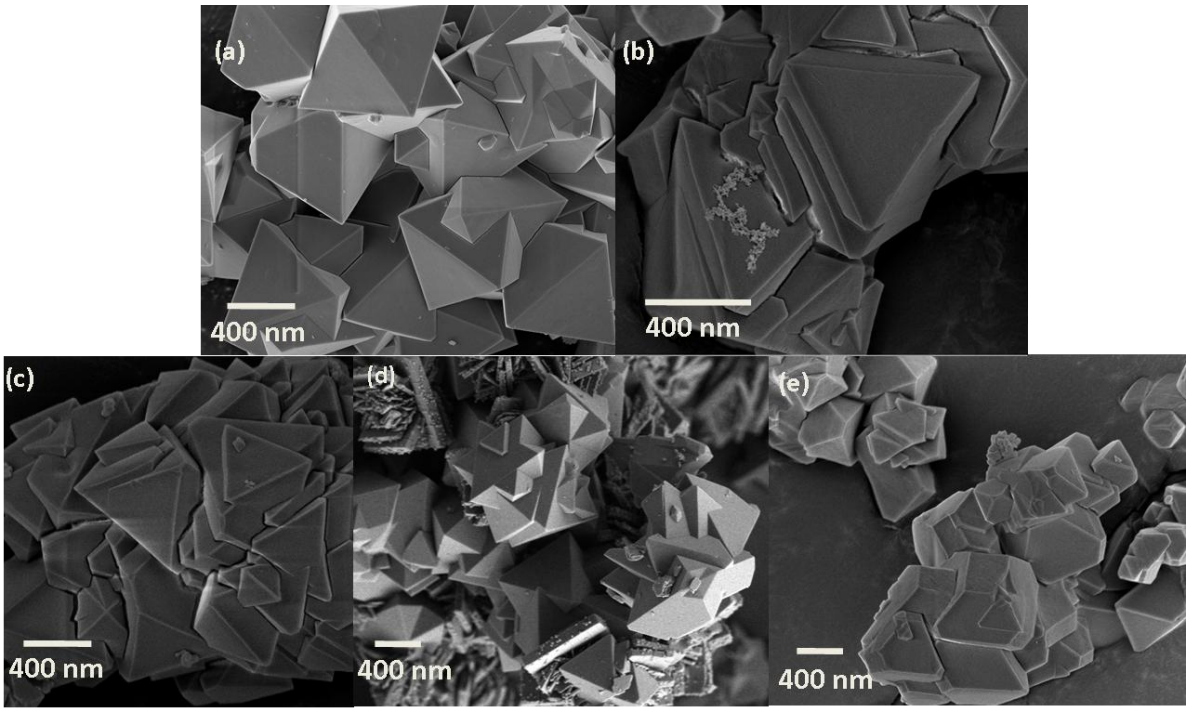

Figure 5.6. SEM images of material prepared with different amounts of linkers. (a) Non-defective, (b) 1:1, (c) 1:1.15, (d) 1:0.5, (e) 1:0.1

The SEM images for all samples are shown in Figure 5.6. The crystals are nano-sized. When the concentration of the linker was decreased, the resulting crystals were not as well-defined as compared to the pristine material but formed heterogeneous agglomerates, although their sizes remain much the same. Under these low linker concentration conditions, the nucleation rate was slower, taking 5 hours to produce precipitates compared to 3 hours for a synthesis

using high linker concentration. This tendency towards crystal growth corresponds to the coordination modulation mechanism, which means that the concentration of the linker affects the growth of UiO-66 during the framework formation.

5.2.2.2 PXRD

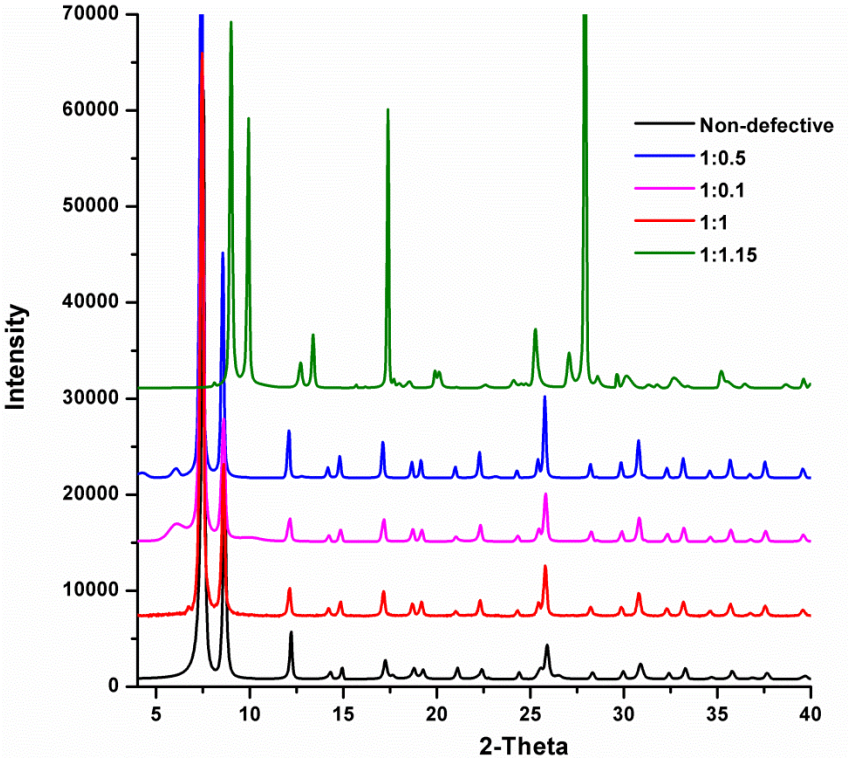

Figure 5.7. PXRD patterns of material synthesised with varying amounts of linker concentrations producing defective material, as well as the PXRD pattern for the non-defective material.

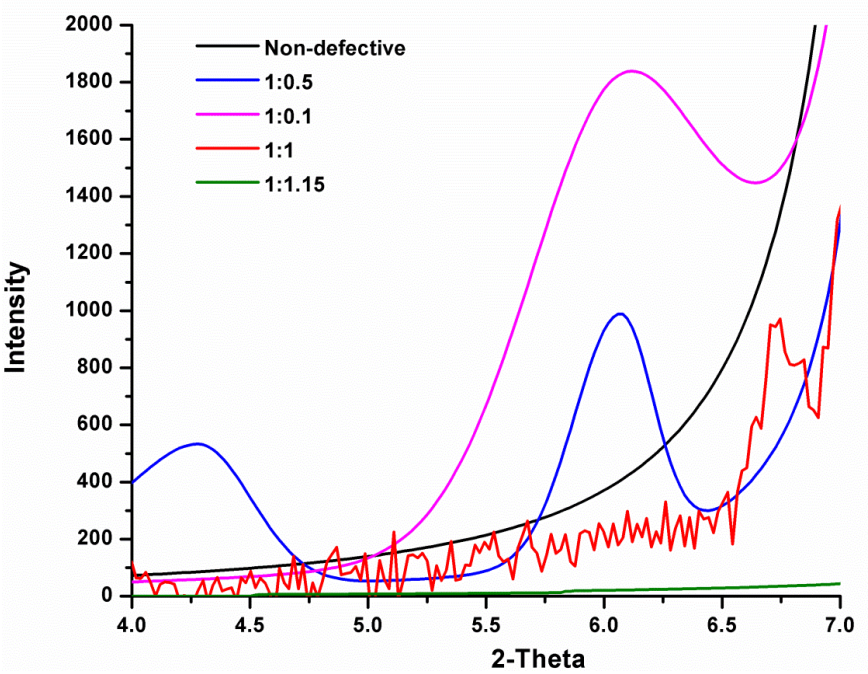

Figure 5.8. Zoomed-in image of the region 4-7° 2-theta revealing symmetry-forbidden peaks.

The PXRD technique was used to analyse the changes of the synthesised UiO-66 as the linker ratio is varied. The X-ray diffraction patterns presented in Figure 5.7 indicate the structure of the UiO-66 obtained. The results show that all the prepared products have the same characteristic peaks as the non-defective UiO-66, suggesting micro-porous MOF structures. The disparity between diffraction peaks provides a good understanding of defects within UiO-66 MOF. For samples synthesised using different amounts of the linker (terephthalic acid), the PXRD range is shown from 3-40 °. Two neighbouring reflections in the region 3-7° shown in Figure 5.8, occurring when nano-size forbidden regions are present in the structure due to the evolution of a large 4-degree peak. These peaks are observed as the number of linkers is reduced. Such nanoregions occur when one-quarter of the SBU cell clusters are absent and result in defect sites in coordinated clusters.

5.2.2.3 TGA

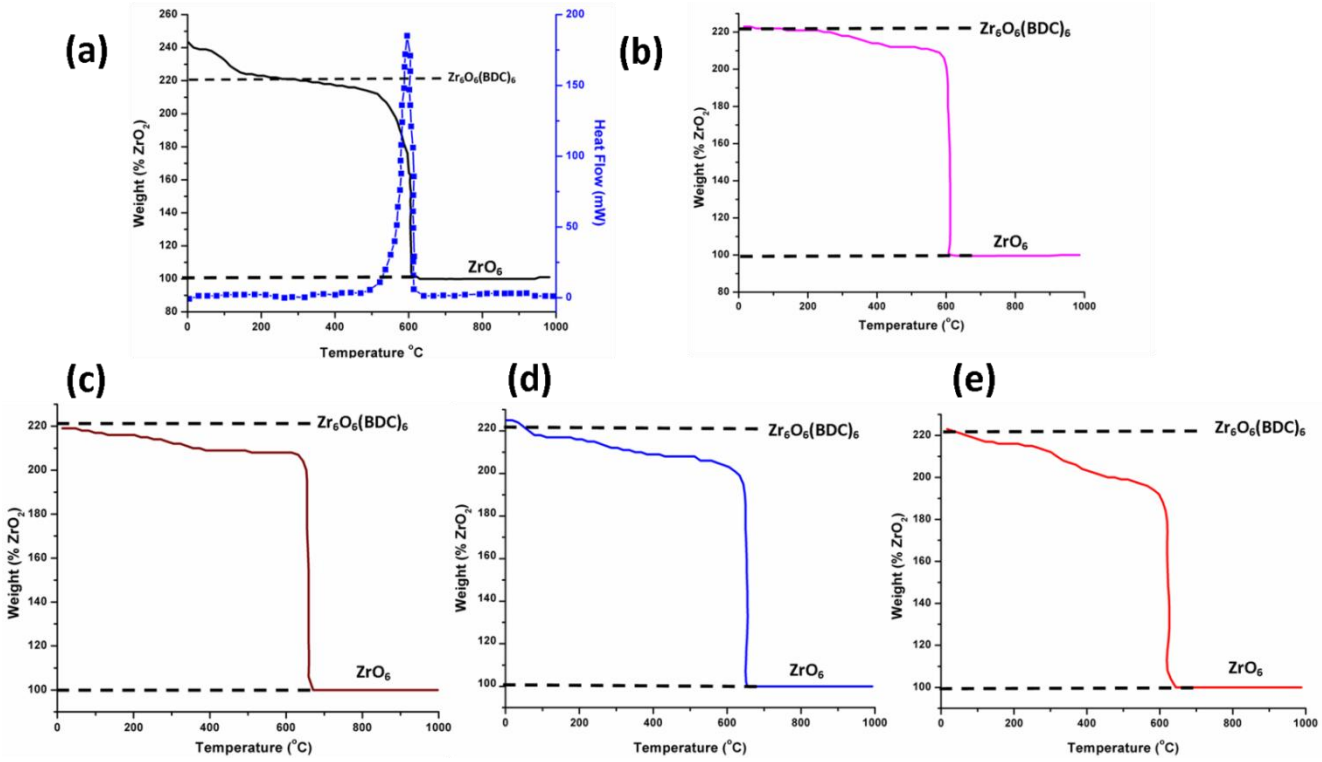

Figure 5.9. TGA curves for non-defective UiO-66 MOF and the defective UiO-66 MOF. (a) non-defective, (b) 1:1.5 (c)1:1, (d)1:0.5, (e) 1:0.1 (ratios representing DMF:FA)

TGA curves of the four as-synthesised UiO-66 samples (synthesised with a reduced amount of linker) are shown in Figure 5.9. All specimens display the weight loss up to 350 °C, and the TGA plateaus are observed in the 350–450 °C range, followed by full framework decomposition at about 600 °C. The first two weight loss steps before 200 °C represent the physical loss of water and trapped solvent molecules, i.e. DMF within the pores. The UiO-66 framework undergoes dehydroxylation at an interval of 200–350 °C. The residual DMF or H_2O coordinated with Zr to compensate for the deficiencies of the linker are removed simultaneously, resulting in the corresponding weight loss step. The plateau for the 'defective' samples occurs at a lower weight (%ZrO_2) than the expected weight of 220.2. This is a clear indication of the presence of defects in these structures.

5.2.2.4 Potentiometric acid–base titration

The potentiometric acid-base titration method has been demonstrated to reliably determine the number of defects. In the ideal (i.e., defect-free) form of UiO-66 each SBU is linked to 12 BDC connectors, giving the $ZrO_4(OH)_4$ cluster one μ3-OH ion. For the titration of defects, two more ions are accessible, either via missing clusters or missing linkers, the Zr-OH_2 and Zr-OH, which mask defective areas. Moreover, in the event of excess modulator, the defect sites may be captured by the single-carboxylated modulator species, which should be titrable if the pH of the solution is significantly lower than the free modulator pKa. Theoretically there are therefore four forms of protons. That proton type can thus be classified and calculated since each proton would have a distinctive pKa value. The pKa values for UiO-66 are 3.52, 6.79 and 8.30 for μ_3-OH, Zr-OH_2 and Zr-OH, respectively [6]. The pKa is estimated to be 4.92 for acetate. The first derivative of the titration curve is intended to represent the different points of equivalence.

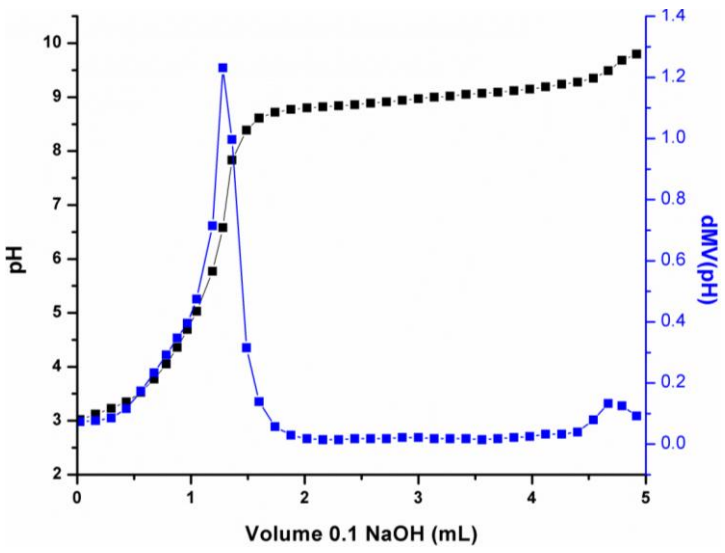

Figure 5.10. Non-defective UiO-66 MOF acid-base titration curve.

For this curve shown in Figure 5.10 we only found one type of titrable ion, the μ_3-OH with a pK_a of 3.29. We can therefore deduce that there are no defects present in this structure.

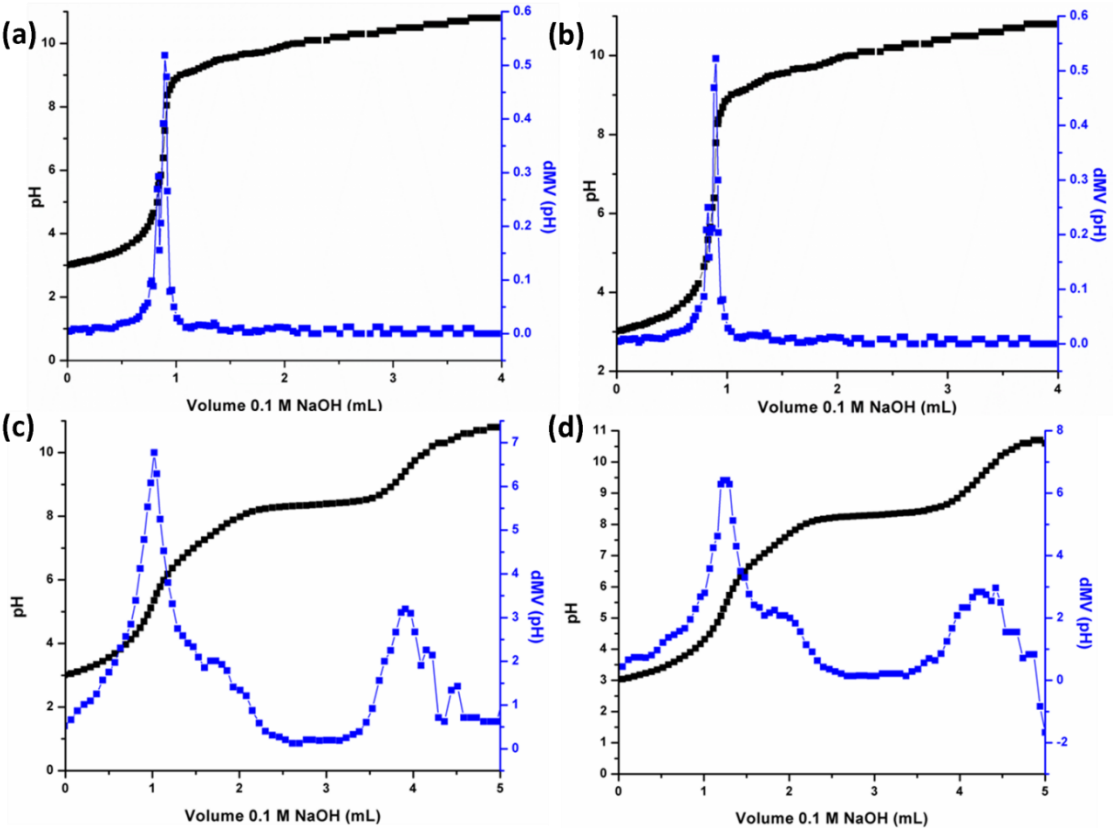

Figure 5.11. Acid-base titration curves obtained for defective UiO-66 MOF samples. (a) 1:1.5 ratio, (b) 1:1 ratio (c) 1:0.5 ratio and (d) 1:0.1 ratio.

We determine the amount of NaOH titrant consumed for each species to determine the number of acetate or –OH/-OH_2 pairs present. With respect to the acetate anions, we take the difference between the second (acetate) and first (μ_3-OH) equivalence points in the quantity of NaOH titrant consumed. Similarly, by taking the difference in NaOH titrant consumed between the third (Zr-OH_2) and second (acetate) equivalence points, the amount of –OH_2 species present can be discovered. From these results, the total number of titrable protons from a pair of –OH/-OH_2 can be calculated by multiplying by three the previously established number of –OH_2 protons (each terminal water is deprotonated once, resulting in an additional hydroxyl terminal group which we believe is equal to the hydroxyl terminal group already existing in the pair). The comparative quantities of titrated protons from pairs of acetates and –OH/-OH_2 are then estimated and allocated respectively to the variables *y* and *z*. These values are then associated

with the molecular formula of UiO-66 incorporating acetate and –OH/-OH_2 pairs and also compensating for missing linkers, $Zr_6O_4(OH)_4(bdc)_{6-x}[(OH_2)(OH)]_{z*2*x}(C_2O_2H_3)_{y*2*x}$, where *x* is the total number of missing linkers in an ideal cluster of $Zr_6O_4(OH)_4(bdc)_6$. The proportion of missing linkers can then be discovered by equating the experimental value of titrated protons with different numbers of missing linkers from the calculated theoretical values [9].

Knowing the quantitative nature of titration, and assuming that each ditopic linker lost represents one aqua and one hydroxo ligand at each of the two nodes, the number of missing linkers in UiO-66 is determined based on the number of titratable M–OH_2 protons and M–OH protons. The needed numbers can be determined from the amount of NaOH titrant consumed between the first equivalence and last equivalence point. Therefore, using this method we calculated the number of missing linkers. The results obtained are tabulated below in table 5.3 using the calculations explained in section 5.2.1.4a.

Table 5.3. Calculated pKa values and their corresponding equivalence points for non- defective and linker deficient samples. The calculated missing linkers are also shown in the final column.

Sample	**EP1**	**-OH pK_a**	**EP2**	**AA pK_a**	**EP3**	**Zr-OH_2 pK_a**	**Missing linkers**
UiO-66-ND	1.28	3.29	-	-	-	-	0
UiO-66-1:1.15	0.839	3.36	0.998	4.40	-	-	0.08
UiO-66-1:1	0.828	3.36	0.979	4.45	-	-	0.084
UiO-66-1:0.5	1.27	3.35	1.93	4.6	-	-	0.36
UiO-66-1:0.1	1.02	3.42	1.67	4.69	2.77	7.34	2.19

5.2.2.5 N_2 adsorption isotherms

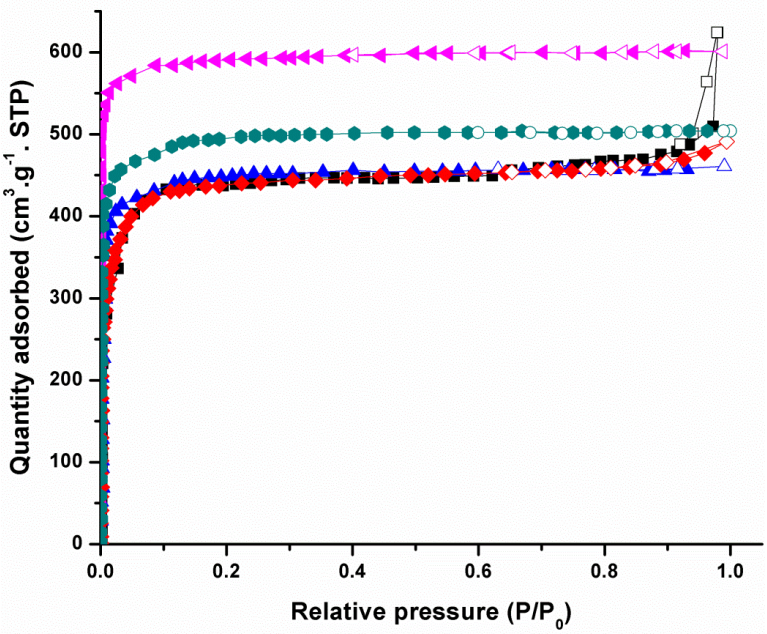

Figure 5.12. BET surface area curve comparing the non-defective (black) and the defective material obtained using different concentrations of linkers. 1:0.1 (pink), 1:0.5 (green), 1:1 (blue) and 1:1.15 (red)

The surface areas of the defective samples UiO-66-1:1 and UiO-66-1:1.15 (1258 $m^2 . g^{-1}$ and 1293 $m^2 . g^{-1}$, respectively) shown in Figure 5.12, are similar to that of the non-defective sample. The most defective samples UiO-66-1:0.5 and UiO-66-1:0.1 exhibited higher surface areas of 1485 $m^2 . g^{-1}$ and 1599 $m^2 . g^{-1}$ respectively. We observe a trend in the surface area increase as the linkers are reduced in number.

5.3 Conclusion

We synthesised defective UiO-66 MOFs using a de-novo method and observed that the defective samples had improved surface areas as compared to the non-defective MOF. The adsorption isotherms are reversible, which means that gases can be adsorbed and desorbed equally as efficiently onto the adsorbent. The quantities of the missing linkers were

successfully allocated by using potentiometric acid-base titrations. From the titrations and calculations of the missing linker, we concluded that the 1:0.1 ratio had the most missing linkers and also exhibited the highest surface area. Potentiometric acid–base titration was found to be an effective experimental technique for quantifying defect sites resulting from missing linkers. TGA and XRD both also proved that the defects were successfully incorporated into the MOF structures.

5.4 References

1. Shearer, G.C., Chavan, S., Ethiraj, J., Vitillo, J.G., Svelle, S., Olsbye, U., Lamberti, C., Bordiga, S. and Lillerud, K.P., Tuned to perfection: ironing out the defects in metal–organic framework UiO-66. *Chem. Mater.*, **2014**, 26(14), 4068-4071.
2. Wu, H., Simmons, J.M., Liu, Y., Brown, C.M., Wang, X.S., Ma, S., Peterson, V.K., Southon, P.D., Kepert, C.J., Zhou, H.C. and Yildirim, T., Metal–organic frameworks with exceptionally high methane uptake: where and how is methane stored. *Chem. Eur. J.* **2010**, 16(17), 5205-5214.
3. Bordiga, S., Lamberti, C., Ricchiardi, G., Regli, L., Bonino, F., Damin, A., Lillerud, K.P., Bjorgen, M. and Zecchina, A., Electronic and vibrational properties of a MOF-5 metal–organic framework: ZnO quantum dot behaviour. *Chem. Commun.*, **2004**, (20), 2300-2301.
4. Jiang, Z., Xiao, T., Kuznetsov, V.Á. and Edwards, P.Á., Turning carbon dioxide into fuel. Philosophical Transactions of the Royal Society A: Mathematical, *Phys. Eng. Sci.*, **2010**, 368(1923), 3343-3364.
5. T-Raissi, A. and Block, D.L., 2004. Hydrogen: automotive fuel of the future. *IEEE Power and Energy Magazine*, 2(6), 40-45.
6. Murray, L.J., Dincă, M. and Long, J.R., Hydrogen storage in metal–organic frameworks. *Chem. Soc. Rev.*, **2009**, *38*(5), 1294-1314.
7. Broom, D.P., Webb, C.J., Fanourgakis, G.S., Froudakis, G.E., Trikalitis, P.N. and Hirscher, M., Concepts for improving hydrogen storage in nanoporous materials. *Int. J. Hydrogen Energy*, **2019**, *44*(15), 7768-7779.

8. Xin, Z., Bai, J., Pan, Y. and Zaworotko, M.J., Synthesis and Enhanced H2 Adsorption Properties of a Mesoporous Nanocrystal of MOF‐5: Controlling Nano‐/Mesostructures of MOFs To Improve Their H2 Heat of Adsorption., *Chem. Eur. J.* **2010**, 16, 13049–13052.
9. Xin, Z., Bai, J., Shen, Y. and Pan, Y., 2010. Hierarchically micro-and mesoporous coordination polymer nanostructures with high adsorption performance. *Cryst. Growth Des.* 10 **2010** 2451–2454.
10. Du, H., Bai, J., Zuo, C., Xin, Z. and Hu, J., 2011. A hierarchical supra-nanostructure of HKUST-1 featuring enhanced H 2 adsorption enthalpy and higher mesoporosity. *CrystEngComm* 13 **2011** 3314–3316.
11. Feng, Y., Jiang, H., Chen, M. and Wang, Y., 2013. Construction of an interpenetrated MOF-5 with high mesoporosity for hydrogen storage at low pressure. *Powder Technol.* 249 **2013** 38–42.
12. Psofogiannakis, G.M. and Froudakis, G.E., 2011. Theoretical explanation of hydrogen spillover in metal− organic frameworks. *J. Phys. Chem. C.* 115 **2011** 4047–4053.
13. Bueken, B., Van Velthoven, N., Willhammar, T., Stassin, T., Stassen, I., Keen, D.A., Baron, G.V., Denayer, J.F., Ameloot, R., Bals, S. and De Vos, D., Gel-based morphological design of zirconium metal–organic frameworks. *Chem. Sci.*, **2017**, *8*(5), 3939-3948.
14. Kim, H., Kim, D., Moon, D., Choi, Y.N., Baek, S.B. and Lah, M.S., Symmetry-guided syntheses of mixed-linker Zr metal–organic frameworks with precise linker locations. *Chem. Sci.* **2019**, 10(22), 5801-5806.
15. Hou, J., Ashling, C.W., Collins, S.M., Krajnc, A., Zhou, C., Longley, L., Johnstone, D.N., Chater, P.A., Li, S., Coulet, M.V. and Llewellyn, P.L., Metal-organic framework crystal-glass composites. *Nat. Commun.*, **2019**, 10(1), 1-10.
16. Wu, H., Chua, Y.S., Krungleviciute, V., Tyagi, M., Chen, P., Yildirim, T. and Zhou, W., Unusual and highly tunable missing-linker defects in zirconium metal–organic framework

UiO-66 and their important effects on gas adsorption. *J. Am. Chem. Soc.* **2013**, 135(28), 10525-10532.

17. De Vos, A., Hendrickx, K., Van Der Voort, P., Van Speybroeck, V. and Lejaeghere, K., Missing linkers: an alternative pathway to UiO-66 electronic structure engineering. *Chem. Mater.* **2017**, *29*(7), 3006-3019.
18. Schaate, A., Roy, P., Godt, A., Lippke, J., Waltz, F., Wiebcke, M. and Behrens, P., 2011. Modulated synthesis of Zr-based metal organic frameworks: from nano to single crystals. *Chem. Eur. J*, **2011**, pp. 6643-6651
19. J. H. Cavka, S. Jakobsen, U. Olsbye, N. Guillou, C. Lamberti, S. Bordiga and K. P. Lillerud. A New Zirconium Inorganic Building Brick Forming metal organic frameworks with exceptional stability. J. Am. Chem. Soc., 2008, 130, 13850–13851.
20. Zhao Q, Yuan W, Liang JM, Li JP. Synthesis and hydrogen storage studies of metal-organic framework UiO-66. *Int. J. Hydrogen Energy*, **2013**, 38: 13104-13109.

CHAPTER 6: POST-SYNTHETIC MODIFICATION

6.1 Post-synthetic modification via acid treatment

6.1.1 Abstract

This chapter presents post-synthetic modification PSM as a chemical classification tool for the modification of MOFs. It has been used widely to tailor porous-frameworks for a wide range of applications based on their physical/chemical properties. PSM has since proven to be a simple yet powerful method to introduce functionalities that cannot be accessed during synthesis. We focus on PSM via acid treatment (Section 6.1) and mechanical treatment (Section 6.2).

6.1.2 Preparation

To determine the applicability of post-synthetic acid modification 5 mg of the synthesised defect-free sample was placed in 2 ml HCl solutions of concentrations 0.05, 0.5 and 1 M at room temperature for 48 hours. The crystals changed from white to yellow within 24 hours. After 48 hours, the resulting off-yellow crystals were separated by filtration, soaked in and washed with DMF to remove any excess HCl.

6.1.3 Results and discussion

6.1.3.1 SEM images

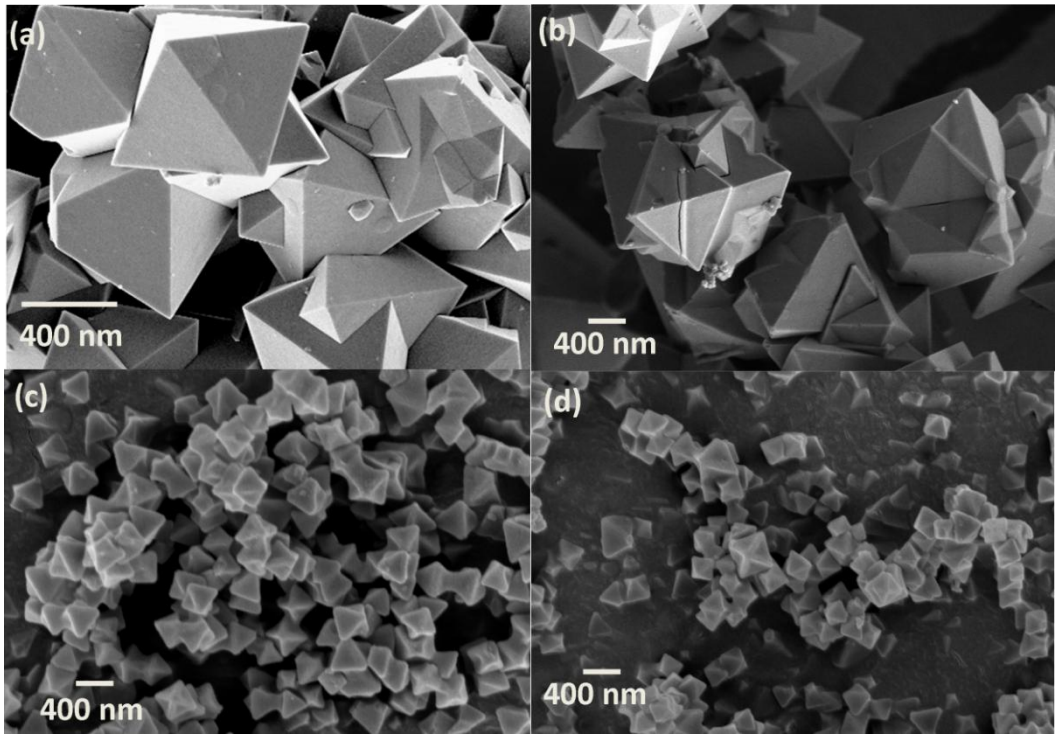

Figure 6.1. SEM images of (a) non-defective UiO-66 MOF and (b) 0.55 M (c) 0.05 M and (d) 1 M acid-treated samples.

SEM indicated that the crystallinity and particle morphology had not been retained after the addition of acid. We also observe from Figure 6.1 a gradual decrease in the size of the inter-grown crystallites from 600 nm to 300 nm. No other significant differences are evident from the images.

6.1.3.2 PXRD patterns

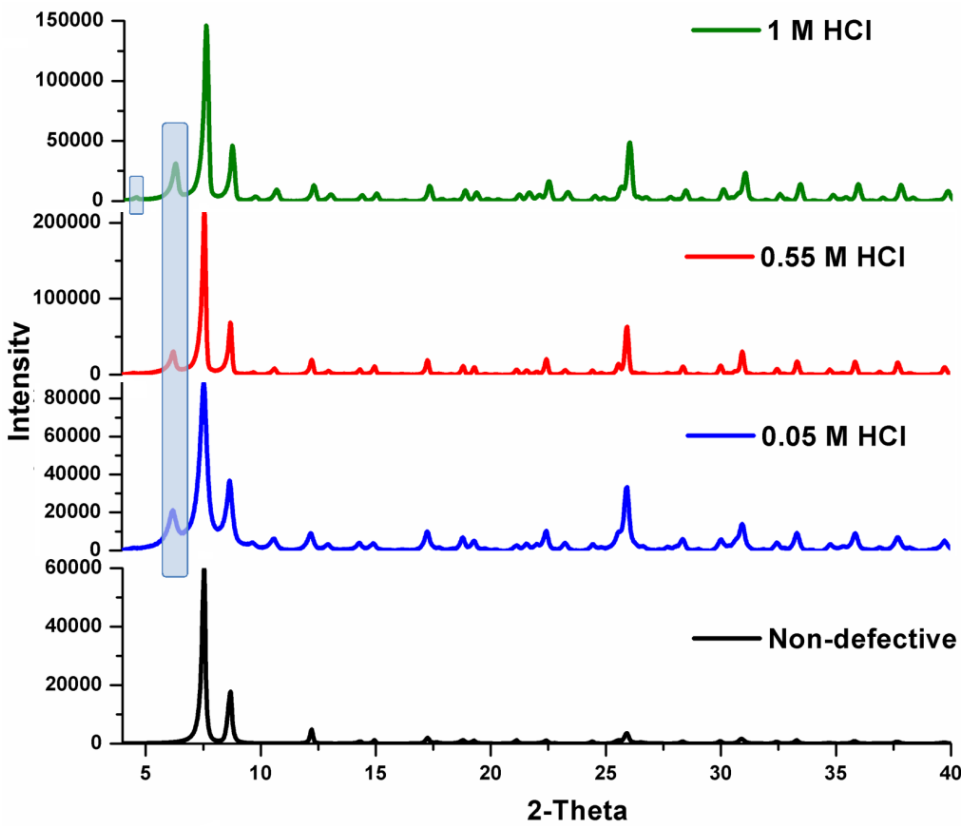

Figure 6.2. PXRD patterns highlight the difference between defective and non-defective UiO-66 MOF samples.

Figure 6.2 shows the X-ray diffraction pattern; the patterns validate the structure of the Zr-based MOF UiO-66. All characteristic peaks are observed with additional peaks which are symmetry-forbidden in the region 3-7° 2θ. These peaks, as mentioned before, are an indication of cluster defects.

6.1.3.3 Pore size distribution

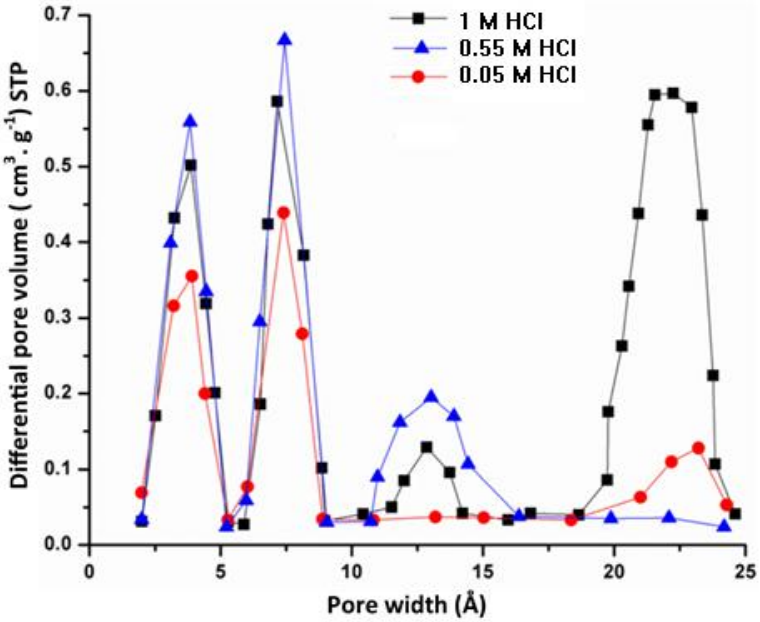

Figure 6.3. Pore size distribution of the different materials post-modified using HCl.

By the introduction of defects, we have increased the pore sizes as shown in Figure 6.3 and the differential pore volume. In most cases an increase in the pore size results in a n unstable MOF. Also, we assume that the acid treatment acts as an activation process, which clears the pores of the framework as we also observed an increase in the surface area [3].

6.1.3.4 TGA

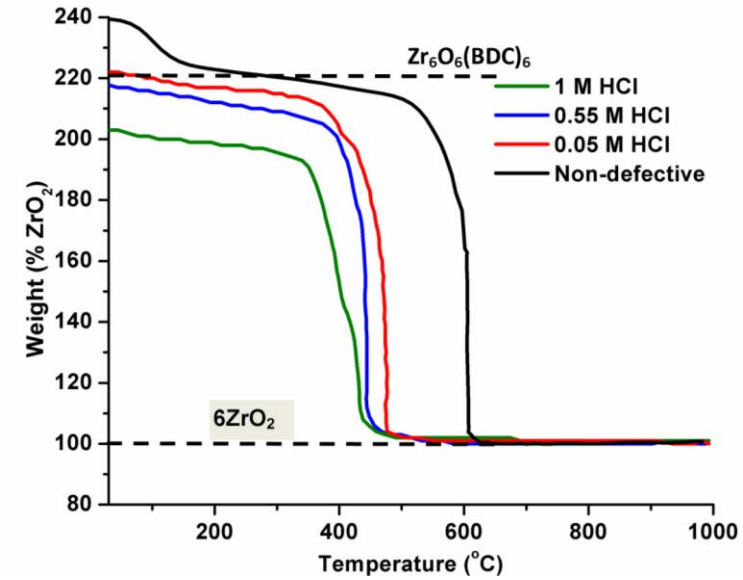

Figure 6.4. TGA thermograms of a non-defective and defective UiO-66 material obtained by treating with acid via PSM.

From the TGA, it is evident that the existence of defects compromised the thermal integrity of the MOF. We notice thermal decomposition at lower temperatures as compared to non-defective material. As illustrated in Figure 6.4, the plateaus for the materials that were post modified using acid are lower than the 220.2% line, as normally observed for a UiO-66 MOF. This is an indication that there are fewer than 12 BDC linkers connected to one Zr_6 cluster, and the molecular weight would thus be lower than that of $Zr_6O_6(bdc)_6$. We can also state that the lower the plateau, more missing linkers/cluster defects are expected in that sample. Therefore the material which was placed in 1 M HCl had more defects.

6.1.3.5 N_2 adsorption isotherms

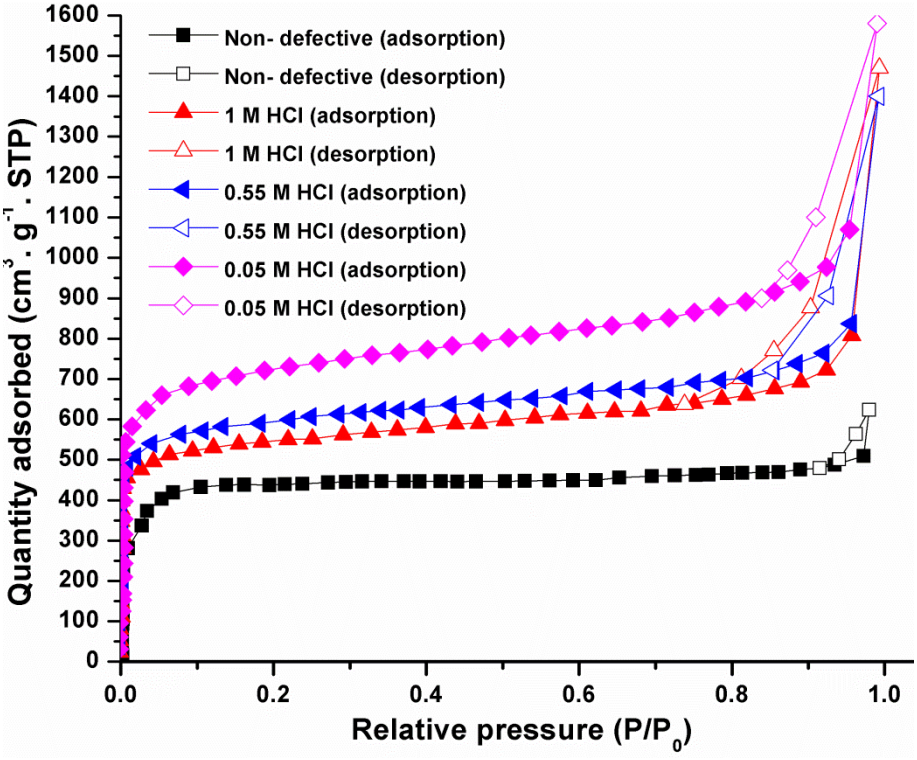

Figure 6.5. BET isotherms of pristine UiO-66 material and defective acid treated samples.

The N_2 adsorption isotherm shown in Figure 6.5 is of type I with a hysteresis loop at a higher P/P_0 ratio (> 0.8), suggesting some mesoporosity and structural microporosity. However, since this is not evident in the SEM images we can assume that the crystals are not uniform in size, and it is possible that there could be some larger particles present in the mixture. However, this cannot be confirmed with the data provided herein. Earlier studies have shown that hysteresis at relative pressure above 0.4 indicates mesoporous defects [1-2].

6.1.3.6 H_2 uptake

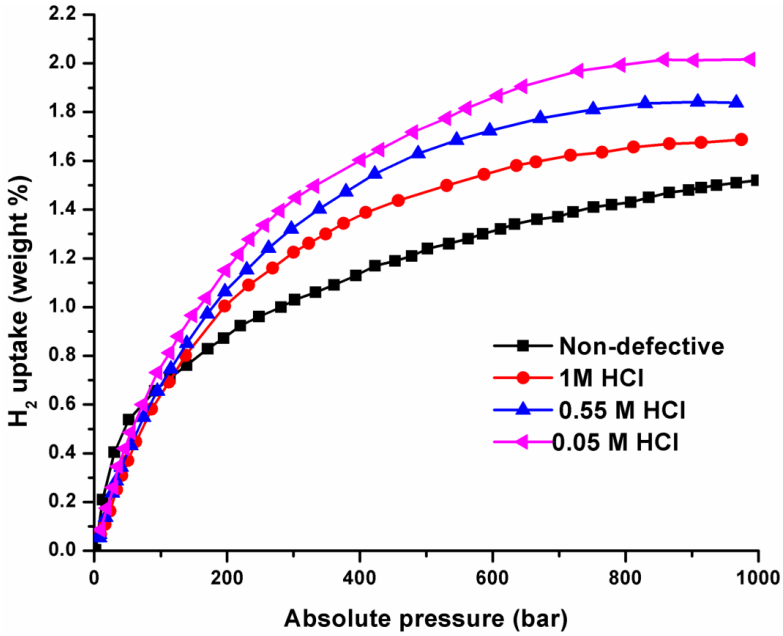

Figure 6.6. H_2 uptake isotherms comparing pristine UiO-66 MOF and defective UiO-66 samples obtained via PSM.

The amount of hydrogen adsorbed by non-defective UiO-66 MOF at low pressures is higher than for the PS-modified samples. However, as the pressure is increased the PS-modified materials steadily adsorb more hydrogen that non-defective material. This shows the importance of high pressure hydrogen adsorption studies in order to reach more accurate conclusions. The increase in uptake depends on the defects introduced; e.g. dangling linkers. Dislocated linkers open new adsorption pockets and increase the uptake of hydrogen [7]. The increase in adsorption indicated in Figure 6.6 is a result of a higher number of different existing adsorption sites and an increased hydrogen adsorption surface area [8].

6.2 Post-synthetic modification via exertion of mechanical force

6.2.1 Abstract

MOFs with high porosity normally exhibit poor mechanical stability. However, UiO-66, a high-porosity Zr-MOF, exhibits unusually high mechanical stability. Studies have shown that the exceptional mechanical stability of UiO-66 is due to its high framework connectivity (i.e. the high degree of coordination between the Zr-O metal centres and the organic linkers) [3]. Herein, we make use of this valuable property for the development of defective UiO-66 MOFs.

6.2.2 Preparation

Milling was performed in two 15 cm3 grinding vials, each containing two 12 mm diameter balls. 5 mg of the defect-free UiO-66 MOF was placed in the grinding vials. The rotation speed of the planetary milling device was optimised to 500 rpm and kept constant for all samples. The only parameter that was adjusted was the time each sample was milled for. The milling times were adjusted to 5, 10, 15 and 20 mins and the resultant products were labelled Mechanical 1, Mechanical 2, Mechanical 3, Mechanical 4, and Mechanical 5, respectively.

6.2.3 Results and discussion

6.2.3.1 SEM images

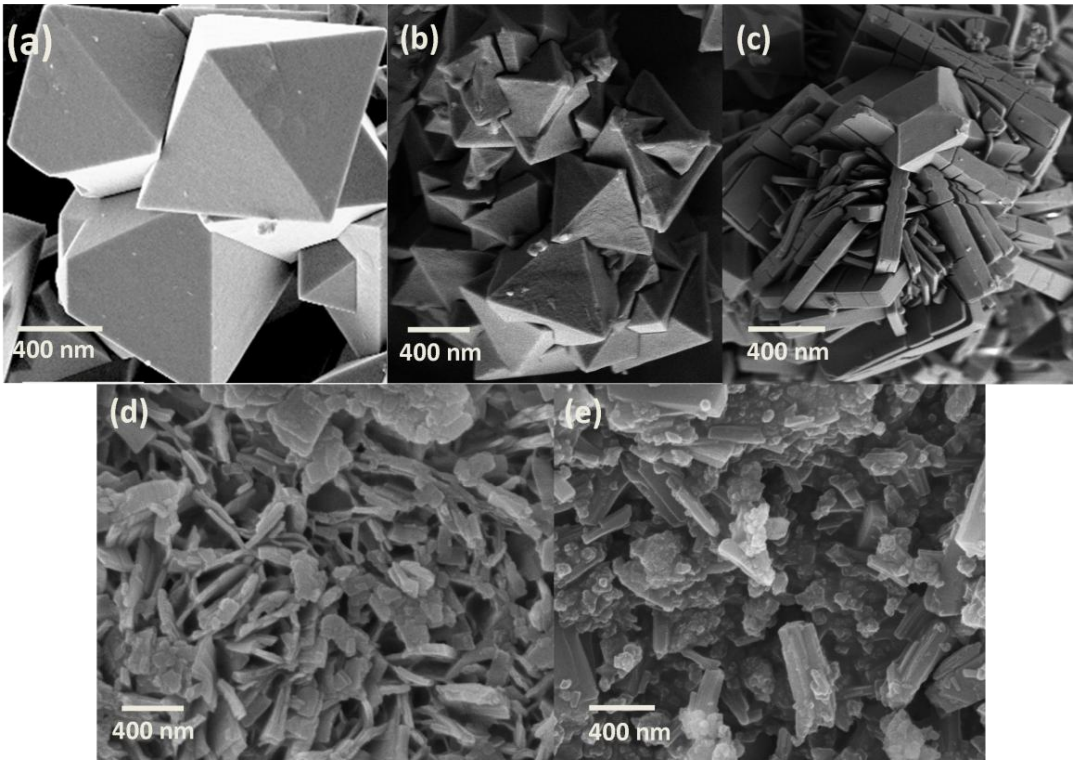

Figure 6.7. SEM images obtained for (a) non-defective UiO-66 sample and (b-e) samples which were mechanically modified for 5, 10, 15 and 20 mins respectively.

From the SEM images shown in Figure 6.7, we observe that the texture of the crystal surface changes considerably and the shape also evolves to yield sheet-like structures. This can be due to impurities or a second phase of nucleation on the crystal surface.

6.2.3.2 FTIR and PXRD

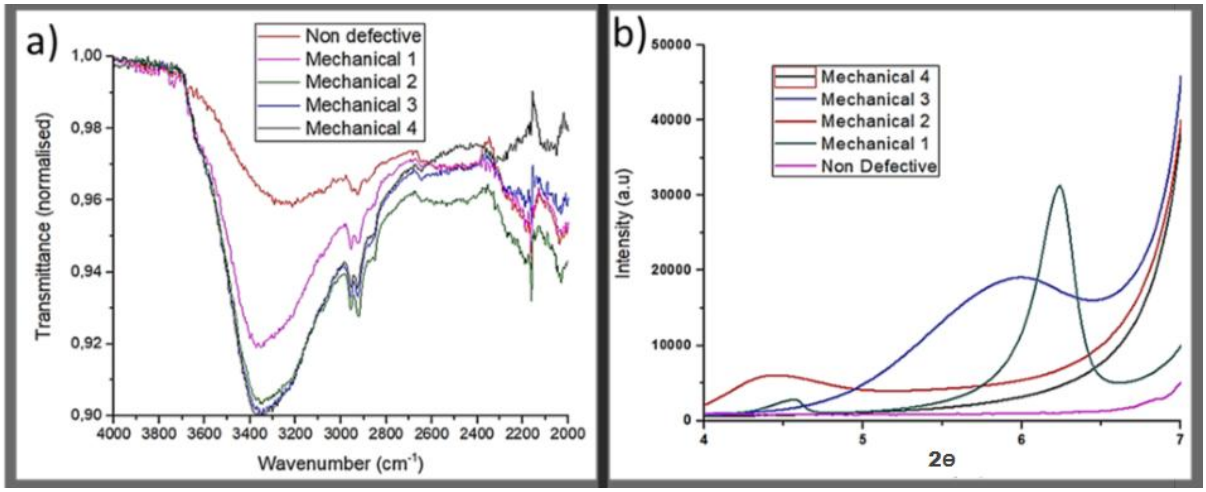

Figure 6.8. (a) FTIR spectra and (b) PXRD diffractograms of non-defective and defective UiO-66 MOF obtained via mechanical PSM..

By using FTIR, we able to acquire efficient information regarding defects present in the structure. Yang et al. [4] suggested that an ideal UiO-66 MOF contains μ_3-OH groups. However defective UiO-66 MOFs gain two additional OH terminal pairs with a proton which has migrated to another position of the node or OH/H_2O terminal pair. Therefore, by analysing FTIR peaks shown in Figure 6.8a, especially those of hydroxyl groups, we can observe additional multiple OH bands in the 3350 cm^{-1} region and in the 2900 cm^{-1} region of the defective UiO-66 MOF spectra. Moreover, the PXRD patterns of both non-defective and defective UiO-66 MOFs do not show any other peaks of impurities or terephthalic acid. It would have been better to provide a detailed analysis of the defect structure but that would only be possible with larger single crystals (5-100 µm). It was difficult to acquire these sizes of crystals and also failure to do Rietveld refinement prevented us from obtaining such results. Therefore, we are able to classify cluster defects using PXRD; they are shown in the region 4-7° 2θ in Figure 6.8b. The peaks in the region shown are due to reo phase which is a form of UiO-66 MOF with missing-cluster defects. The intensity of the peaks also gives an indication

of the concentration of the defects; generally, the higher the peaks, the more defects found in the structure [5].

6.2.3.3 TGA

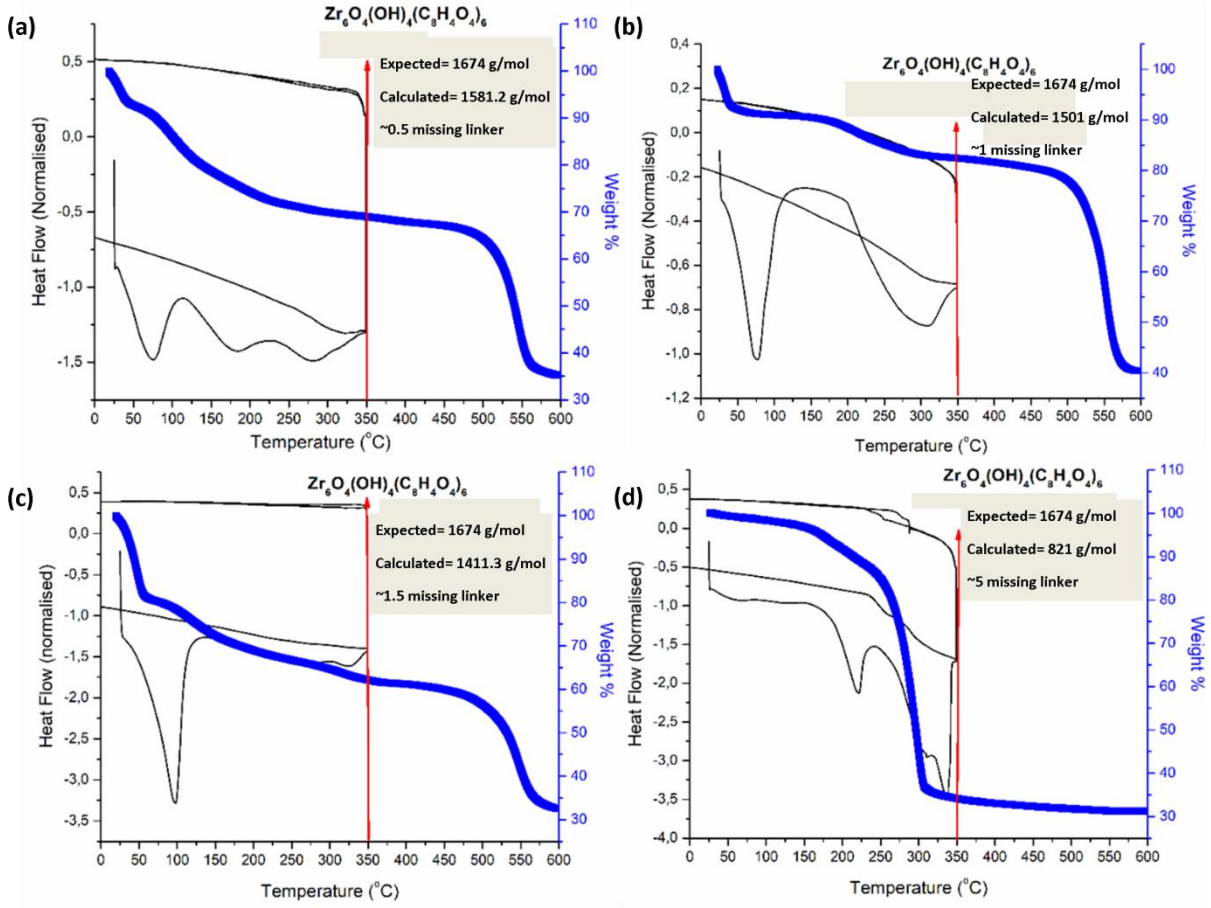

Figure 6.9. TGA thermograms showing the weight % of a) mechanical 1, b) mechanical 2, c) mechanical 3 and d) mechanical 4 defective UiO-66 MOFs, (black) DSC thermograms.

We used TGA to calculate the number of missing linker defects. The UiO-66 TGA analysis in Figure 6.9 shows three distinct steps that lead to various decomposition phases. The loss of solvent molecules and hydrogen-bound water are the first significant weight losses (under 423 K). The dehydroxylation of the $Zr_6O_4(OH)_4$ cluster group to the Zr_6O_6, as well as the loss of the linkers and the water molecules leads to the decomposition of the framework and the formation of ZrO_2. In this case, the final mass loss (623-823 K) is where the highest weight %

is lost and is used to estimate the number of missing linkers. In the dehydroxylation step, we assumed, that the Zr_{12} double cluster does not separate through loss of six Zr_2-OH but instead loses the terephthalic acid and hydrogen bonded water to yield a double dehydroxylated cluster $(Zr_6O_6)_2.(OH)_6$. We have, however, observed peaks in the PXRD suggesting that there are missing clusters. Therefore, the loss of weight could be a result of loss of clusters and not only linkers.

6.2.3.4 N_2 adsorption isotherms

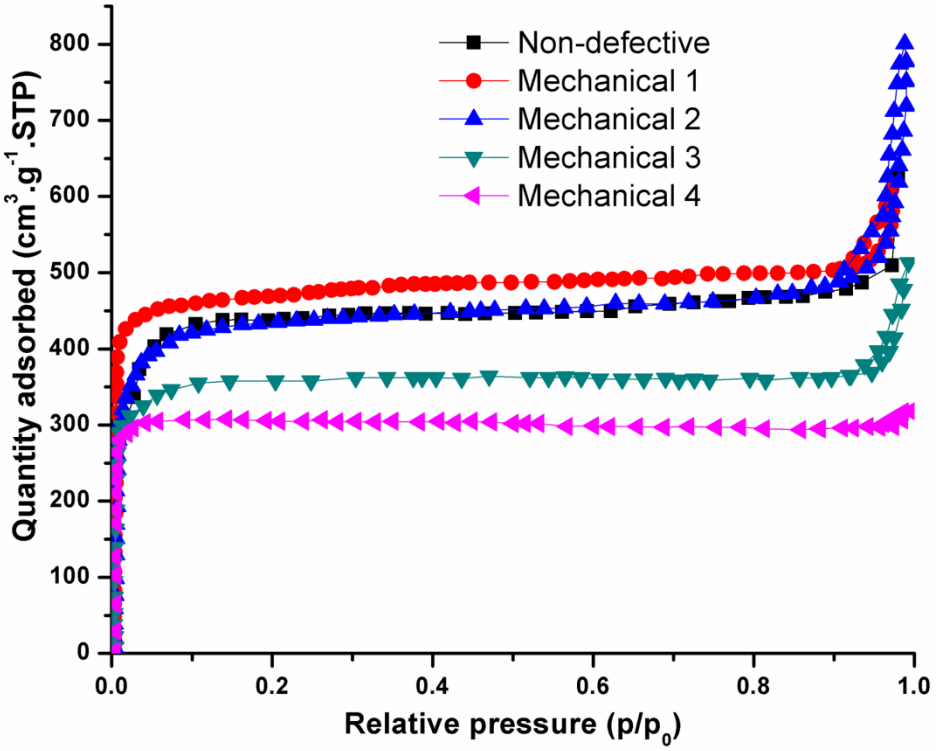

Figure 6.10. BET isotherms of mechanically modified UiO-66 samples and non-defective sample.

Defect formation plays a significant role in pore structural changes and thus has a huge effect on the BET surface area. It is evident that there is a correlation between BET surface area and linker deficiency. Shearer and co-worker [6] proved there is a linear correlation between BET surface area and linkers missing from a structure. This is not always true because another study

proved that a high concentration of defects may compromise the surface areas significantly. From Figure 6.10 we initially observed an increase in BET surface area when mechanical force was exerted for a shorter period. However as we further exposed the material to mechanical force for longer period, we noticed a decrease in the surface area, which could be a result of high concentrations of missing linkers which may have collapsed or destroyed the structure.

6.2.3.5 H_2 adsorption isotherms

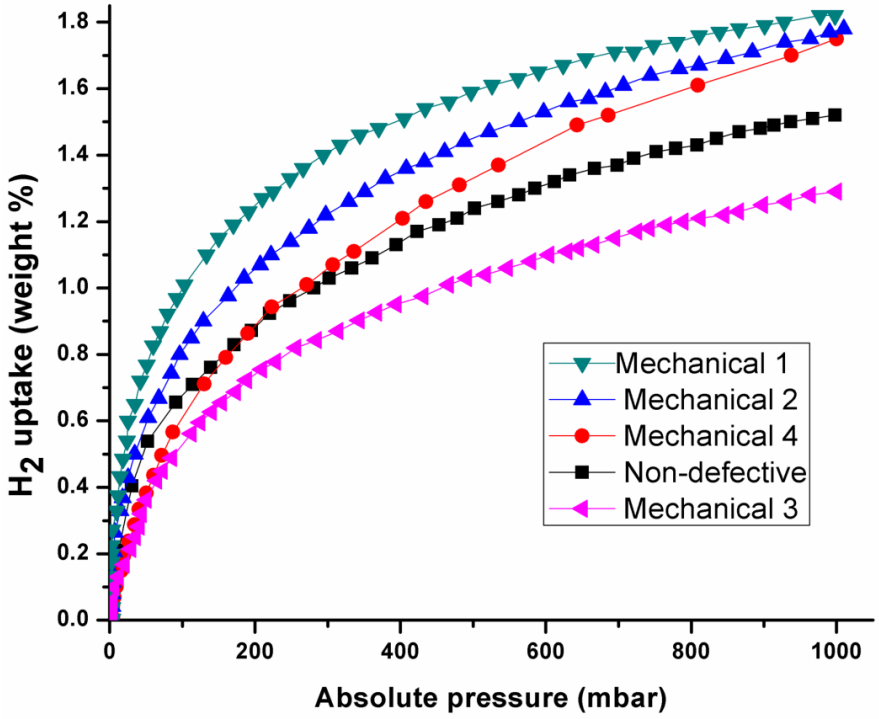

Figure 6.11. H_2 uptake isotherms for non-defective and defective UiO-66 MOFs.

Regulated defects have been shown to have an important positive effect on the MOF surface compared to non-defective material. This discovery was intended to promote the process of hydrogen spill-over, which is one of the most effective ways to increase the storage capacity of hydrogen in environmental conditions [9]. The Zr-MOFs labelled Mechanical 1, Mechanical 2 and Mechanical 3 displayed in Figure 6.11 show a relatively high H_2 uptake in comparison to the H_2 uptake of the defect-free material. Similarly, we observed higher BET surface

mechanically modified material compared to the non-defective content previously mentioned. Mechanical 4 exhibited lower H_2 uptake than all the other samples, implying that the material was unable to retain the hydrogen molecules due to the large pore sizes.

6.3 **Comparison of optimised conditions**

Finally, we compared the optimised conditions in each section and the high pressure H_2 uptake is shown below.

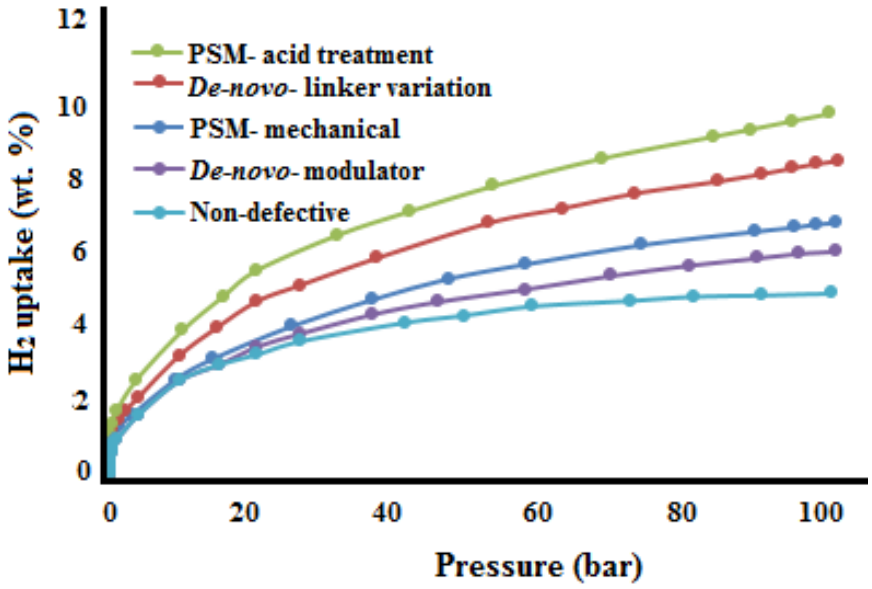

Figure 6.12. High pressure H_2 uptake for optimised conditions for each defect-engineering method

Figure 6.12 show that hydrogen uptake was higher for the acid treated samples obtained via PSM. The material was optimised by using 0.05 M HCl at room temperature for 24 hours. The H_2 uptake reached 9.57 wt. % at 100 bar. This is a good improvement over the H_2 uptake of the non-defective MOF at high pressure, which was 5.1 wt. %. This material also had the highest surface area as compared to all the synthesised and modified materials. The DOE target is 7 wt. % absolute uptake, and both the PSM acid-treated and de-novo MOFs have reached this standard.

6.4 **Conclusion**

Compared to the parent UiO-66, the defective UiO-66 reveals substantial differences in the adsorption capacity, revealing that the pore size is greatly increased due to missing linker / cluster defects. BET surface area studies was also undertaken to analyse the surface area of linker deficient MOFs after exposure to acidic conditions and mechanical pressure. This work shows that the pore size can be modified as a function of the concentration of the defect. Furthermore, it is seen that the systemic modification by the acidic medium in the defective UiO-66 contributes to an expansion in the average pore size without compromising the chemical stability of the acidic species. Despite ongoing scientific interest in defective MOFs, laboratory studies discussing the mechanical stability of defective MOFs are currently not available in the literature [10]. Even after carrying out this study, we believe that more extensive work needs to be done in order to provide adequate knowledge in this area. The findings of this work advance the knowledge of textural properties and chemical stability of defect-engineered MOFs, and we also propose a preparation process for the synthesis of defective but stable MOFs.

6.5 References

1. Vishnyakov, P.I. Ravikovitch, A.V. Neimark, M. Bülow, Q.M. Wang, Nanoporestructure and sorption properties of Cu-BTC metal-organic framework. *Nano Lett*. **2003,** 3 (6), 713–718.
2. G.W. Peterson, G.W. Wagner, A. Balboa, J. Mahle, T. Sewell, C.J. Karwacki, Ammo-nia vapor removal by Cu3(BTC)2and its characterization by MAS NMR, *J. Phys. Chem. C*. **2009,**113 (31) 13906–13917.
3. Wu, H., Yildirim, T. and Zhou, W., Exceptional mechanical stability of highly porous zirconium metal–organic framework UiO-66 and its important implications. *J. Phys. Chem. Lett*. **2013**, 4(6), 925-930.
4. Yang, Q., Wiersum, A.D., Jobic, H., Guillerm, V., Serre, C., Llewellyn, P.L. and Maurin, G., Understanding the thermodynamic and kinetic behavior of the CO2/CH4 gas mixture within the porous zirconium terephthalate UiO-66 (Zr): a joint experimental and modelling approach. *J. Phys. Chem. C*, **2011**, 115(28), 13768-13774.
5. Cliffe, M.J., Wan, W., Zou, X., Chater, P.A., Kleppe, A.K., Tucker, M.G., Wilhelm, H., Funnell, N.P., Coudert, F.X. and Goodwin, A.L., Correlated defect nanoregions in a metal–organic framework. *Nat. Commun*., **2014**, 5, 4176.
6. Shearer, G.C., Chavan, S., Ethiraj, J., Vitillo, J.G., Svelle, S., Olsbye, U., Lamberti, C., Bordiga, S. and Lillerud, K.P., Tuned to perfection: ironing out the defects in metal–organic framework UiO-66. *Chem. Mater.*, **2014**, 26(14), 4068-4071.
7. Szilágyi, P.Á., Serra-Crespo, P., Gascon, J., Geerlings, H. and Dam, B., The impact of Post-synthetic linker Functionalization of MOFs on Methane storage: The role of Defects. *Frontiers Energy Res.* **2016**, *4*, 9.
8. Hanzawa, Y. and Kaneko, K.,. Gas Adsorption. In Carbon Alloys. *Elsevier Science* **2003,** 319-334.

9. Ren, J., Langmi, H.W., Musyoka, N.M., Mathe, M., Kang, X. and Liao, S., Tuning defects to facilitate hydrogen storage in core-shell MIL-101 (Cr) @ UiO-66 (Zr) nanocrystals. *Mater. Today: Proc.* **2015**, *2*(7), 3964-3972.
10. Øien, S., Wragg, D., Reinsch, H., Svelle, S., Bordiga, S., Lamberti, C. and Lillerud, K.P., Detailed structure analysis of atomic positions and defects in zirconium metal–organic frameworks. *Cryst. Growth Des.* **2014**, *14*(11), 5370-5372.

CHAPTER 7: CONCLUSION AND RECOMMENDATIONS

The objective of this thesis was to synthesise and characterise UiO-66 MOF material, engineer them by introducing defects and optimise the conditions to achieve high hydrogen uptake. All of the above have been reported and achieved satisfactorily.

Four different methods for introducing defects were explored, namely modulator variation and linker variation (which fell under *de novo* engineering), followed by acid treatment and mechanical methods (which fell under PSM). The materials were characterised using various techniques, namely SEM, PXRD, TGA, FTIR, Raman, N_2 adsorption/desorption, and then their sorption performances were tested for H_2 at low and high pressures. The different MOFs analysed herein have provided an in-depth insight on the subtleties of the properties of UiO-66 MOF and their behaviour under various conditions.

The non-defective material was synthesised successfully, and its characterisation provided enough evidence to prove that there are no, or insignificant defects detected in the material. The Raman spectra and PXRD patterns matched the data for a pristine simulated UiO-66 MOF. The TGA plateaus at 220.2 (% ZrO_2), which is expected for a MOF with no missing linkers/clusters. Furthermore, using potentiometric acid-base titration, we were able to prove that there was one titrable μ_3-OH, which is contained in the SBU of a UiO-66 MOF. No additional titratable OH were found using this method for the non-defective material. The surface area for the non-defective material was found to be 1275 $m^2.g^{-1}$ and the material had a hydrogen uptake of 1.51 wt. % at 1 bar and 77 K, which is standard for UiO-66 MOFs.

Our first attempt at introducing defects involved using formic acid as a modulator, formic acid, and varying the concentration of this modulator to find the optimum concentration that produced enough defects to offer the highest hydrogen uptake. Though this approach of using a modulator and studying the associated defects has been investigated before, our approach of

optimisation in order to reach high surface areas and hydrogen uptake has not been explored. We observed no change in the structure though the dimensions did change. However, there was no proportionality in the increase of the modulator concentration in relation to the dimensions. No phase changes were observed by PXRD except for the occurrence of broad symmetry-forbidden peaks for the defective material. With regard to the N_2 adsorption, only the 1:1.5 DMF:modulator ratio showed an increase in the accessible surface area, with the 1:1 ratio showing similar results to the non-defective material. The lack of hysteresis in the defective material is an indication of the easily accessible pores. The increase in surface area thus resulted in a high H_2 uptake for the 1:1.5 ratio.

For the linker ratio variation material, potentiometric acid-base titrations studies were conducted in order to quantify the defects in these materials. Again, we observed symmetry-forbidden peaks for the defective material and the intensity of the peaks correlated with the concentrations of the defects. This technique has proven to be efficient in quantifying defects.

The highest surface area and hydrogen uptake observed in all the materials synthesised in this study was by the post-modified material that was acid treated with 0.05 M HCl. All materials obtained from post modification were microporous. The results followed the same pattern as those of defective material produced where the defects were created during the synthesis. Finally, from the results presented herein, linker ratio variation and acid treatment via PSM proved to be the most efficient way of introducing defects, which resulted in the highest surface areas and hydrogen uptake.

Work that may follow from this work could be the use of different MOFs and introducing novel linkers which may be easily manipulated and controlled. Howe et. al [1] have suggested the use of mixed metals or incorporating Ni or Co as metal centres to enhance the chemical stability during defect engineering. As we did notice that when we reached a certain level of

modification, the material instability of the structure when the defects are introduced. The introduction of sulphate groups can also be an interesting study as the sulphate groups would impart strong Brønsted acidity and the results can be comparable with those reported herein for HCl treatment. This can be achieved by reacting the MOF with aqueous sulphuric acid to generate its sulphated analogue. Sulphuric acid chemically attacks the surface structure of the defective ZrMOF resulting in the sulphation of the Zr moieties and the sulphonation of the organic functional groups, in addition to the deposit of residual sulphate ions on the surface. Long-term stability is another important factor that needs to be considered before applying adsorbents in practical processes. Therefore, long-term water exposure experiments on MOFs should also be conducted in the future, especially if this is to be used in conventional vehicles or similar applications, and particularly for the acid-treated materials. Though we were able to study the kinetics of the defect-free material, it would be interesting to also conduct a study of the kinetic changes in defective materials as this would provide an explanation of why and how we observe an increase in hydrogen adsorption. To advance the modulator variation studies, one could investigate the relationship between the pKa of different acid modulators and hydrogen adsorption. One strategy for further exploring this mechanism would be to synthesise defective UiO-66 variants using trifluoroacetic acid (pKa = 0.23), difluoroacetic acid (pKa = 1.24), fluoroacetic acid (pKa = 2.6), and acetic acid (pKa = 4.76) as the acid modulators.

7.1 References

1. Howe, J. D.; Morelock, C. R.; Jiao, Y.; Chapman, K. W.; Walton, K. S.; Sholl, D. S., *J. Phys. Chem. C* **2017**, 121 (1), 627-635.
2. Shearer, G. C.; Chavan, S.; Bordiga, S.; Svelle, S.; Olsbye, U.; Lillerud, K. P., *Chem. Mater.* **2016**, 28 (11), 3749-3761.